Chapter 4. Identifying ferroelectric domain structure using angle-resolved piezoresponse force microscopy

AR-PFM was used in conjunction with VPFM and EBSD to provide a systematic interpretation of domain patterns in polycrystalline, near-morphotropic PZT. This study develops methods for resolving complex domain patterns where multiple phases may be present. AR-PFM was carried out with a 30° rotation interval, and the resulting data were analysed to identify the orientation of the underlying axis of piezoelectricity. The additional information provided by AR-PFM was studied, comparing its capabilities to those of 3D PFM, consisting of one VPFM image and two orthogonal LPFM images. It is shown that, in certain conditions, using AR-PFM can identify the phases present at the sub-grain scale. This was confirmed using VPFM and EBSD data. Additionally, the details of the process to generate AR-PFM maps including image registration to correct for the spatial distortion caused by scanner creep and the non-linearity in SPM are also introduced. The research presented in this chapter was published as follows:

Kim KL, Huber JE. Identifying ferroelectric phase and domain structure using angle-resolved piezoresponse force microscopy. Appl Phys Lett 2014;104:122901–1–4.

Kim KL, Huber JE. Mapping of ferroelectric domain structure using angle-resolved piezoresponse force microscopy. Rev Sci Instrum 2015;86:013705–1–11.

4.1 Introduction and literature review

Characterization techniques [36,37] such as electron microscopy and SPM have been used to study domain structure in ferroelectrics and hence how domain structure governs the material properties [9,10]. In particular, PFM is widely used to resolve ferroelectric domains at high resolution [99,120]. Several advanced PFM techniques have been developed including local polarization switching [116], piezoresponse force spectroscopy [122,123], and quantitative analysis of PFM signal using the carefully calibrated instruments [109,110]. In chapters 2 and 3, it was shown that PFM can provide detailed information about domain patterns, and by combining with EBSD data, could provide an understanding of domain evolution caused by electrical or mechanical loading. However, there was uncertainty over the domain pattern in some cases.

PFM can also provide 3D surface displacement data induced by the local converse piezoelectric effect, by combining VPFM and LPFM [79,80]. LPFM enables us to partially overcome a limitation of VPFM by distinguishing between adjacent domains with similar out-of-plane piezoelectric response, but different in-plane response. Figure 4.1 shows a typical example of 3D PFM [79]. A PZT capacitor that was negatively poled from the top electrode appears in uniform contrast in VPFM phase image in figure 4.1(a). However, two orthogonal LPFM images in figures 4.1(b)–(c) reveal that the poled capacitor is still in a multiple-domain state. These three PFM images enable reconstructing a 3D map of polarization in figure 4.1(d) when the possible polarization directions are known as shown in figure 4.1(e). LPFM exploits the torsional behaviour of the cantilever to detect in-plane oscillations of the sample surface due to piezoresponse. Thus, the LPFM signal is affected by the sample orientation with respect to the cantilever. Based on this principle, recent works [124–126] have analysed the variation of the LPFM signal with sample rotation. The results showed that the LPFM phase signal changes sign

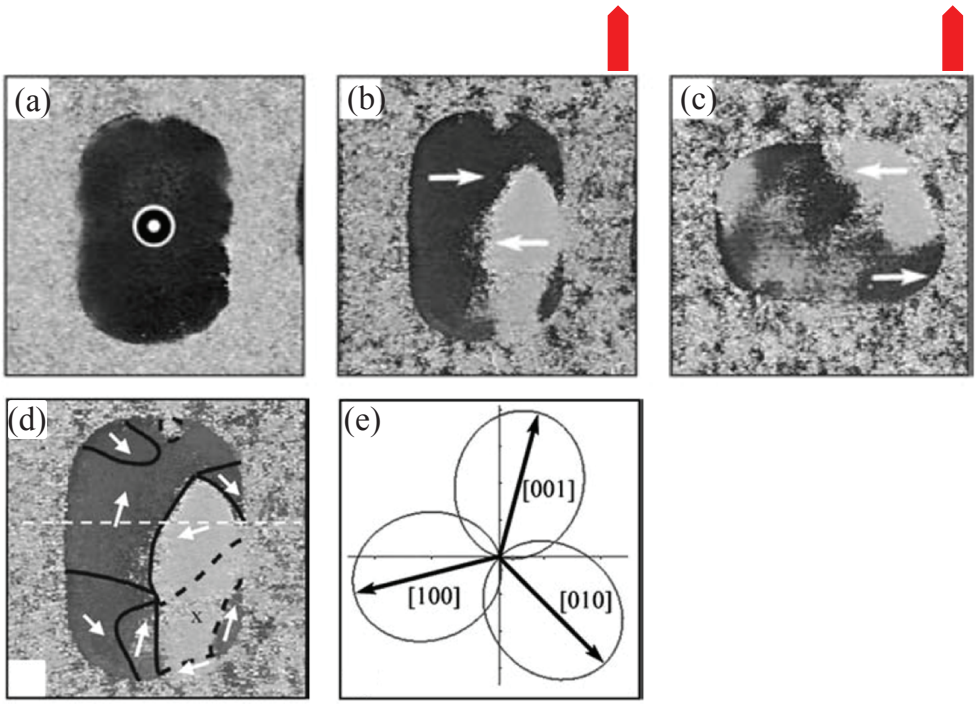

Figure 4.1: (a) VPFM phase image and (b),(c) LPFM phase images of a ferroelectric capacitor . Note that (c) was taken after a 90° counter-clockwise rotation of the sample from (b). An out-of-plane arrow in (a) indicates the vertical component of polarization direction deduced from the VPFM phase signal. Arrows in (b),(c) show the lateral components of polarization direction with respect to the cantilever orientation, shown above each image, deduced from the LFPM phase signal. (d) The reconstructed map of polarizations based on VPFM and LPFM images in (a)–(c) and the possible polarization vectors in tetragonal PZT in (e) (modified from [79]).

twice during a 360° rotation; the angle at which the sign change occurs corresponds to the orientation of the surface displacements.

This idea was extended for mapping domains by using the angle of phase reversal to obtain extra data about domain structure [127–129]. In AR-PFM, stepping the sample rotation through a range of angles enables the microscope to expose domain patterns that would not be clear from the VPFM component alone. This ability of AR-PFM has been exploited to study charged domain boundaries [127,128], and domain evolution under electrical loading [129]. The image introduced in figure 4.2(a) shows a map of domain configuration generated using AR-PFM method by Park *et al.* [128]. In this image, the orientation of surface displacement was identified using LPFM signals. And based on the surface displacement vectors, charged domain boundaries were studied. The boundaries

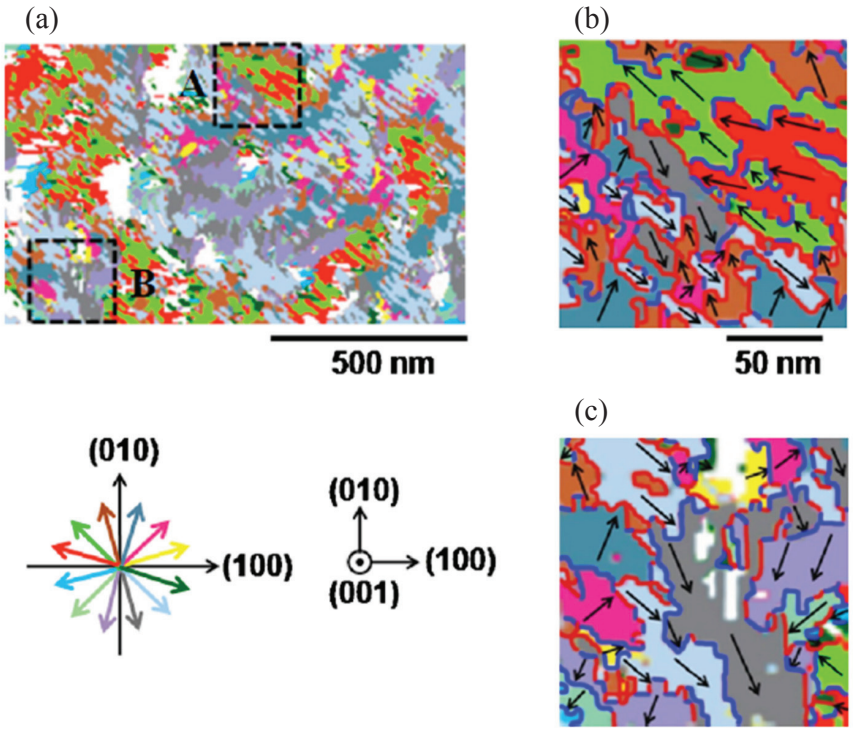

Figure 4.2: (a) A map of domain configuration in $BiFeO_3$ thin film produced by AR-PFM. (b) and (c) are the enlarged views of 'A' and 'B' in (a), respectively (modified from [128]).

between each domain are marked by blue and red lines indicating neutral and charged domain boundaries, respectively. Figures 4.2(b)–(c) show the enlarged views of the regions 'A' and 'B' in figure 4.2(a), respectively. However, the AR-PFM method does produce some complications such as effects of scanner distortion and the need for care in interpreting polarization directions from surface displacements. There has been relatively little work aimed at systematically understanding AR-PFM.

In this chapter, the process for mapping domain structure using AR-PFM is introduced, and attention is given to sources of error that arise during the process. In addition, for a systematic interpretation of results, crystal orientation data is obtained using EBSD, so that crystallographic planes can be identified. Using knowledge of the specific habit planes and arrangements of non-180° domain walls [21] then enables the interpretation of domain patterns and polarization directions.

A consequence of the use of multiple methods in the present work is that it becomes possible to compare the direction of lateral surface displacement, measured by AR-PFM, to the in-plane polarization direction, deduced using EBSD data. The surface displacement direction and polarization direction are commonly taken to be identical [126,130], but in the present work the discrepancy between these two directions is illustrated. Also, in conjunction with EBSD data, AR-PFM enables discrimination between material in the rhombohedral phase and material in the tetragonal phase at the sub-grain scale. These points are illustrated with observations of domain patterns in near-morphotropic PZT.

4.2 The AR-PFM method

PFM works by exciting the local converse piezoelectric response of a surface using an oscillating voltage applied to the scanning probe cantilever tip. Since this induces oscillating mechanical displacements in the surface, the contacting tip also oscillates at the driving frequency; the amplitude and phase of these oscillations provide the PFM signal. The cantilever motion is monitored through the reflection of laser light from the cantilever onto a photodetector. In VPFM the vertical (out-of-plane) oscillations due to cantilever bending are measured, while LPFM data is derived from the torsional oscillations of the cantilever. Consequently, LPFM data relates to in-plane surface displacements that are perpendicular to the cantilever.

A schematic of the AR-PFM method is shown in figure 4.3(a). In AR-PFM, a series of LPFM scans is conducted at the same location on the sample surface. After each LPFM scan, the sample is rotated about a vertical axis through a constant rotation interval, while the orientation of the cantilever remains fixed. The underlying polarization directions in the sample rotate with the sample, and accordingly the surface displacement

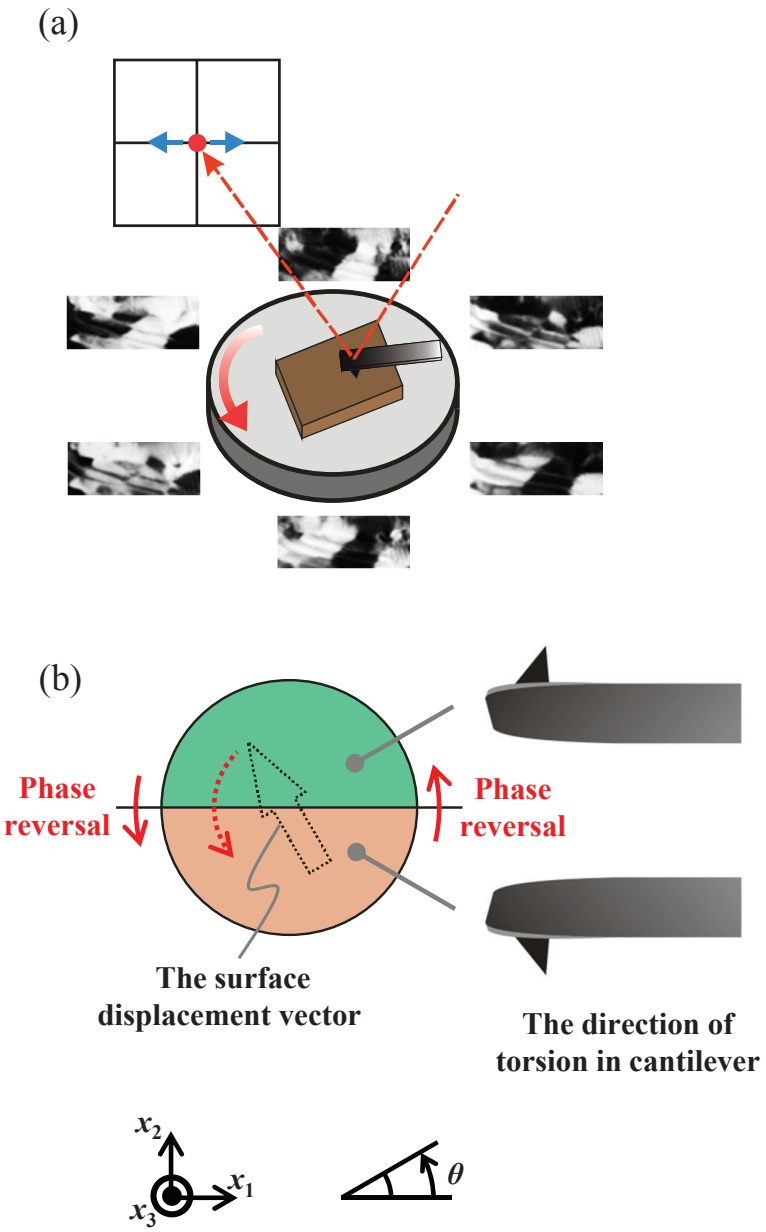

Figure 4.3: (a) A schematic of the AR-PFM method. (b) The relationship between the direction of torsion in the cantilever and the surface displacement vector during 360° sample rotation.

vectors also rotate. It is normally assumed that the relative orientation of the sample and cantilever does not affect the distribution of electric field within the sample, so that the rotation of the sample surface displacement matches exactly the rotation of the sample itself. This assumption is reasonable provided the scanning probe tip produces an axisymmetric voltage distribution at the sample surface. Then, the VPFM data is invariant to sample rotation but distinct LPFM data are generated at each rotation angle. To

illustrate this, six LPFM images taken with a 60° rotation interval are shown in figure 4.3(a). Of course, rotation of the sample also rotates the measured data in instrument co-ordinates. For this reason, the images in figure 4.3(a) have been rotated back into sample coordinates to facilitate comparison of features in the images. It is immediately evident that rotating the sample changes the LPFM contrast. Details of the experimental method that produced figure 4.3(a) will be discussed later in this chapter.

Figure 4.3(b) shows the relationship between the direction of torsion in cantilever and the surface displacement vector during 360° sample rotation. In the instrument coordinate system shown in figure 4.3(b), the cantilever is aligned with x_1, and the torsion of the cantilever is driven by the surface displacement component u_2 along $\pm x_2$. Thus the LPFM signal amplitude will be greatest when the sample is aligned such that the surface displacements are along $\pm x_2$ and the signal amplitude will fall to zero when the surface displacements are along $\pm x_1$. More generally, material rotation through angle θ transforms the surface displacement vector $\mathbf{u} = \begin{bmatrix} u_1 & u_2 & u_3 \end{bmatrix}^{\mathrm{T}}$ into

$$\mathbf{u}' = \begin{bmatrix} \cos\theta & -\sin\theta & 0 \\ \sin\theta & \cos\theta & 0 \\ 0 & 0 & 1 \end{bmatrix} \mathbf{u}. \tag{4.1}$$

Hence

$$u_2' = u_1 \sin\theta + u_2 \cos\theta, \tag{4.2}$$

and $u_2' = 0$ when

$$\tan\theta = -u_2 / u_1. \tag{4.3}$$

Note also that $u_1'(\theta + \pi) = -u_1'(\theta)$, $u_2'(\theta + \pi) = -u_2'(\theta)$, and $u_3'(\theta + \pi) = u_3'(\theta)$. Thus the lateral components of surface displacement vector u_1', u_2' are expected to change sign during a 180° sample rotation while the vertical component of surface displacement

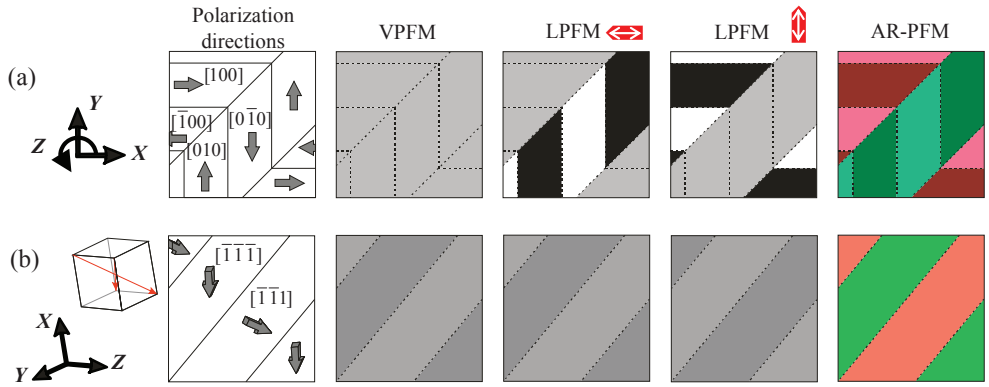

Figure 4.4: (a) An example of the domain structure visualized through 3D PFM. (b) The domain structure that cannot be clearly visualized through 3D PFM. The domain patterns in both (a) and (b) can be exposed by AR-PFM maps through distinct colouring according to surface displacement orientation.

vector u_3' remains unchanged. This is confirmed experimentally in section 4.4. The piezoresponse signal is expected to be either in-phase or 180° out-of-phase with the input voltage signal. By colouring each point in the scan according to the rotation angle at which phase-reversal occurs, an AR-PFM map is generated that shows the direction of surface displacements associated with the converse piezoelectric response of each point on the sample surface.

The advantages of the AR-PFM method in identifying ferroelectric domains are illustrated in figure 4.4 which shows a comparison between 3D PFM and AR-PFM using two hypothetical domain patterns. For ease of understanding, the comparison is made under the assumption that the direction of lateral surface displacement matches the in-plane component of the local polarization. We shall return to the distinction between these effects in section 4.5.

First consider the pattern of polarization directions shown in figure 4.4(a). Here all polarization vectors are in-plane, having no vertical component. This type of domain pattern can arise in tetragonal ferroelectric crystals with the crystallographic axes (*X, Y*, *Z*) as shown in figure 4.4(a). In this case, VPFM cannot discriminate the domains. By contrast, the domain pattern can be exposed through LPFM images from orthogonal scan

directions. But a single LPFM scan does not necessarily distinguish the four domain types present, and is unlikely to show strong contrast between these domains. Meanwhile, the four in-plane polarization directions are separated by 90°, and hence easily distinguished by AR-PFM, provided the rotation interval between scans is less than 90°.

In the second example, figure 4.4(b), the domain pattern consists of polarization vectors $[\bar{1}\bar{1}\bar{1}]$ and $[\bar{1}\bar{1}1]$ in the rhombohedral crystal system, with (*X*, *Y*, *Z*) axes as shown. The crystal orientation was generated using three Euler angles (175.4°, 49.2°, 290.2°) that illustrate a case where two polarization directions are both into-plane (that is, both have negative x_3 components in instrument co-ordinates) and both belong to the fourth quadrant of sample rotation. In this case, neither VPFM nor LPFM can clearly expose the domain pattern through the phase signal, and only weak contrast would appear in amplitude images. Once again, AR-PFM can clearly expose the domain pattern by identifying the orientation of surface displacements. In this case, since the surface displacement directions are close together, a much smaller AR-PFM rotation increment is needed for good discrimination. In fact, this scenario is rather common in randomly oriented crystals because the random orientation makes it likely that some pair of domains will produce similar surface displacements through their converse piezoelectric effects. The situation is also likely to arise in multi-phase materials where there may be many domain orientations [126].

How many rotation steps are needed to provide an AR-PFM map? Since $u_2'(\theta+\pi) = -u_2'(\theta)$ there is no need to obtain LPFM signals from more than two quadrants of sample rotation. Now suppose a ferroelectric crystal has *n* stable polarization orientations, giving rise to $n/2$ distinct surface displacement directions that may be observed in any 180° range of sample rotation. Then rotation increments $\Delta\theta > 2\pi/n$ cannot discriminate the *n* orientations of surface displacement. If the underlying crystal

orientation is known in instrument co-ordinates, such that the expected surface displacements are known, then setting $\Delta\theta$ less than the angle between the two closest in-plane surface displacement directions guarantees being able to discriminate the set of domains using AR-PFM. However, if the crystal orientation is not known in advance, then the angle between the two closest surface displacement directions may be arbitrarily small. Then a compromise is needed between angular resolution and the practical difficulty of taking large numbers of PFM scans. As $\Delta\theta$ is reduced, finer discrimination in surface displacement direction is achieved. However, the requirement for a greater number of LPFM scans increases the risk of tip degradation, which adversely impacts the quality of PFM data – this is discussed further in section 4.4.3. In the present work, experiments are conducted on randomly oriented polycrystalline PZT, which has 6 distinct polarization directions in the tetragonal phase and 8 in the rhombohedral phase. Thus $\Delta\theta < 2\pi/8$ was needed, and a 30° interval of sample rotation was used as a practical compromise between accuracy, acquisition speed and maintaining signal quality.

4.3 Application of AR-PFM to a polycrystalline ferroelectric

To illustrate the AR-PFM method, scans were carried out on samples of bulk polycrystalline PZT (PZT-855, APC International). This material was chosen because it presents significant challenges for AR-PFM measurement: the randomly oriented grains mean that we do not know in advance what polarization directions will be present. Furthermore, PZT-855 has a composition close to the morphotropic phase boundary separating the tetragonal and rhombohedral phases [15,16]. As noted in chapter 1, both the tetragonal and rhombohedral phases can be present in this material at room temperature. Accordingly, the material can be polarizable in any <100> or <111> direction. The mechanical and electrical compatibility conditions in equations (1.1) and

(1.2) provide a set of possible domain wall orientations in each phase as shown in figure 1.4. However, non-180° domain walls can be formed in {110} planes in both phases. Therefore, finding a matching plane for domain walls does not discriminate between tetragonal and rhombohedral phases unless the matching plane is one of {100}. One advantage gained by using PZT-855 is that the piezoelectric response is among the strongest of any known material, so that PFM signals are readily obtained.

The magnitude of spontaneous strain is $(c-a)/a = 1.38\%$ along <100> in the tetragonal phase, and $8\beta/3 = 0.0155\,(\text{rad})$ in the rhombohedral phase where c is the lattice parameter along the polarization direction, a is the lattice parameter orthogonal to the polarization direction in tetragonal, and β is the rhombohedral shear angle [17]. The significance of these magnitudes is that the spontaneous strains are slightly too small to be reliably discriminated by our EBSD measurements [131]. Thus, EBSD was used to only obtain the pseudo-cubic axis orientations of the crystal lattice in figure 4.5.

The samples tested were bulk PZT plates approximately 2 mm thick. The imaging surface was polished to a mirror finish using a 40 nm colloidal silica suspension. The back surface was electroded using conductive paint and adhered to a sample mount. The material was in an unpoled condition.

A Veeco Dimension 3100 nanoscope with a built-in lock-in amplifier was used to acquire VPFM data, and Signal Access Module III (Veeco) with SR830 lock-in amplifier (Stanford Research Systems) were installed for LPFM signal acquisition. The resulting LPFM data are pure phase signals, while the VPFM data contains mixed amplitude and phase signals. During the VPFM and LPFM scans, topography data were collected simultaneously with PFM data. For signal optimization in each scan mode, distinct scanning probes were chosen for acquiring VPFM and LPFM data. For VPFM, Bruker SCM-PIC probes were used with a 5 V amplitude of tip voltage at 180–200 kHz near

contact resonance frequency. Meanwhile, in LPFM, Nanosensors PPP-NCSTPt probes were used with a 5 V amplitude of tip voltage at 6.8–7.8 kHz. The range of frequencies indicated is due to the use of optimised frequencies for each region of the sample surface, but a constant frequency was used throughout AR-PFM in any one region.

One issue arising in AR-PFM is the need to rotate the sample while accurately maintaining the sample position within the instrument. Our instrument has a rotation stage, but was unable to place the rotation centre under the scanner with sufficient accuracy to avoid the need for realignment between scans. Therefore the region of interest was re-located after each LPFM scan using instrument co-ordinates and topography features.

EBSD measurements were carried out in an Evo LS ESEM, operated at 10 Pa pressure and 10–15 kV. The Kikuchi patterns were analysed using Orientation Imaging Microscopy data analysis software. Euler angles identifying the orientation of the common pseudo-cubic axes (point group m3m) were obtained. The intersection of key crystallographic planes with the sample surface was then computed using Matlab.

Figures 4.5(a)–(d) show preliminary observation of the region of interest, using the EBSD inverse pole figure, EBSD image quality map, AFM topography map and VPFM image, respectively. The EBSD image quality map shows up grain boundaries (dark contrast) due to the inability of the EBSD to identify a unique crystallographic orientation at these points. The grain boundaries identified by EBSD were used to check that the region of interest was correctly located across the two instruments. Figure 4.5(e) is an enlarged view of the rectangle marked in figure 4.5(d).

Note that two distinct lamellar patterns A and B can be observed within a single grain in figures 4.5(d)–(e). The crystallographic planes of these non-180° lamellations were identified using EBSD data, and will be discussed in section 4.5. The region in

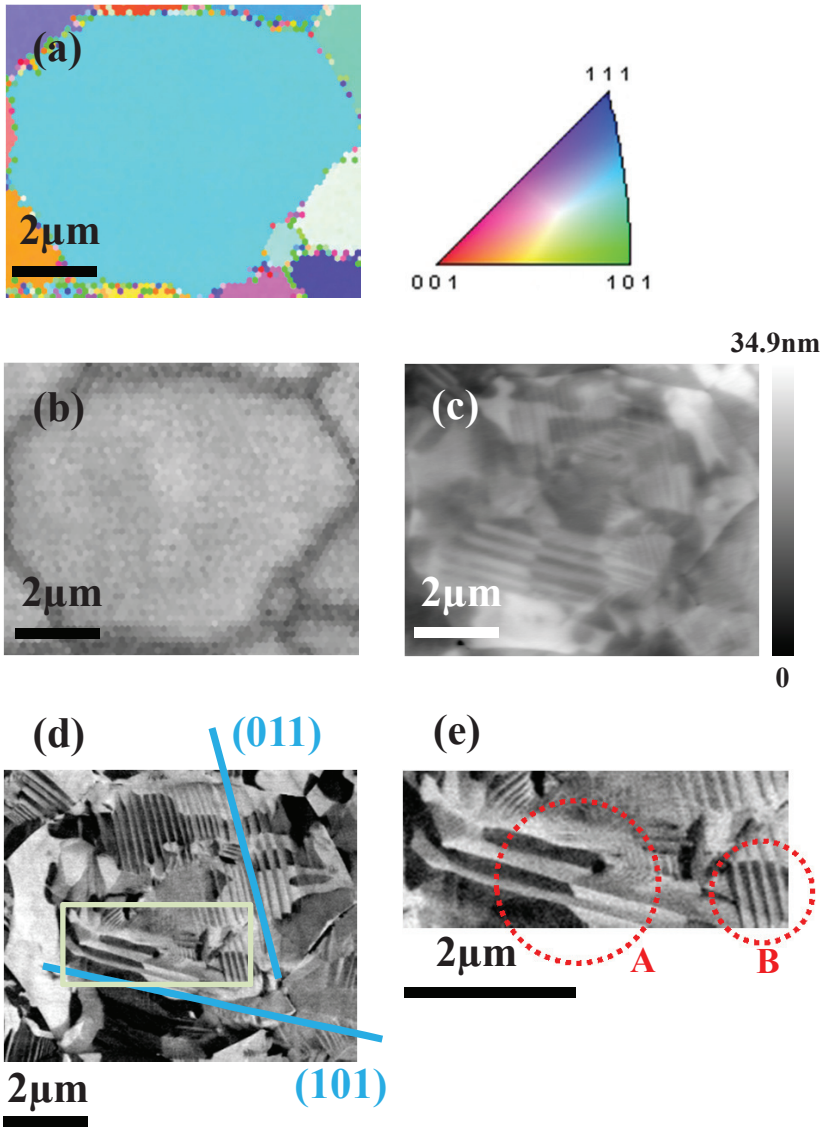

Figure 4.5: Identifying crystallographic planes of lamellar patterns using AFM, PFM, and EBSD data. The identical region is shown through (a) EBSD inverse pole figure, (b) EBSD image quality map, (c) AFM topography, (d) VPFM image; a rectangle marks the region enlarged in (e).

figure 4.5(e) was then studied using AR-PFM. Rotation increments of 30° were used and a full 360° cycle consisting of twelve LPFM phase images was recorded to check the reversal of contrast with each 180° rotation.

4.4 Processing of LPFM data to produce AR-PFM images

4.4.1 Image registration

The objective of AR-PFM is to provide angular orientation information about the direction of the surface displacements caused by the converse piezoelectric effect. In equation (4.3), the rotation angle $\theta = \theta_0$ such that $u_2'(\theta_0) = 0$ corresponds to phase reversal in the LPFM phase data and is correlated with the orientation of the underlying crystal orientation. Mapping θ_0 over the region of interest provides information about the underlying crystal orientation that is not present in VPFM or orthogonal LPFM images. The use of equation (4.3) to identify θ_0 at each pixel in the AR-PFM image requires pixelwise comparison of a set of LPFM images. To study the variation of LPFM signal in each pixel during sample rotation, the set of LPFM images first need to be aligned in the same coordinate system. This requires a rotation of each image into a common reference frame. However, to achieve accurate alignment of SPM images taken from different sample orientations, image registration is also essential to correct for scanner artefacts such as non-linearity and creep [132]. A variety of techniques exist for the correction of scanner artefacts in SPM, mainly based on comparison of multiple measurements from the same region [133]. Here, we emphasize that the objective is not the absolute correction of spatial distortion in the SPM data, but rather removal of differences in distortion which arise due to the sample rotation. The main sources of distortion considered were scanner non-linearity, drift and creep.

First, the open-loop scanner was calibrated using standard calibration grids to minimise the effects of intrinsic non-linearity in the piezoelectric *x*–*y* drive. This calibration enables the microscope to give accurate *x*–*y* position control close to the zero-offset central position. Thus the main sources of distortion in images centred on the zero-

offset position are likely to be thermal drift and creep, rather than intrinsic non-linearity. The first LPFM image in the series was taken with *x*–*y* zero-offset and the corresponding topography image was used as the basis for image registration. The subsequent LPFM images, captured after successive sample rotations, required scanner offsets in the range 0–10 μm for re-centring. Since scanner non-linearity can be significantly influenced by these scanner offsets image registration was used to enable pixel-wise correlation. Also, creep generally occurs in the open loop configuration whenever a spatial offset is used during scanning [69]. Finally, angular errors of order ±0.2° in the sample rotation were expected since manual alignment against a scale was used.

To correct for these errors, image registration was carried out using Matlab. Since the AFM topography signal is expected to be consistent for all sample orientations, the topography data was used for image registration. A second order polynomial correction function was generated for each LPFM scan other than the 0° scan by locating and marking features in the topography images. This corresponds to the control point selection method of image registration in Matlab's Image Processing Toolbox. An alternative method, automatic registration, has the advantage that it does not require manual input of control points, but proved unable to correct for the multiple sources of distortion present in the LPFM data.

To illustrate the image registration process, figure 4.6 shows the process applied to the topography image taken from 270° sample orientation. Image 1 in figure 4.6(a) shows the raw topography image at $\theta = 270°$. The image was first rotated clockwise by 270° (image 2). Next, a set of about 50 control points in the base image were manually identified and located in image 2, see figure 4.6(b). This set of points was used to define a least square error best fit transformation of second order polynomial type. The transformation is applied to image 2, generating the final image 3, with improved

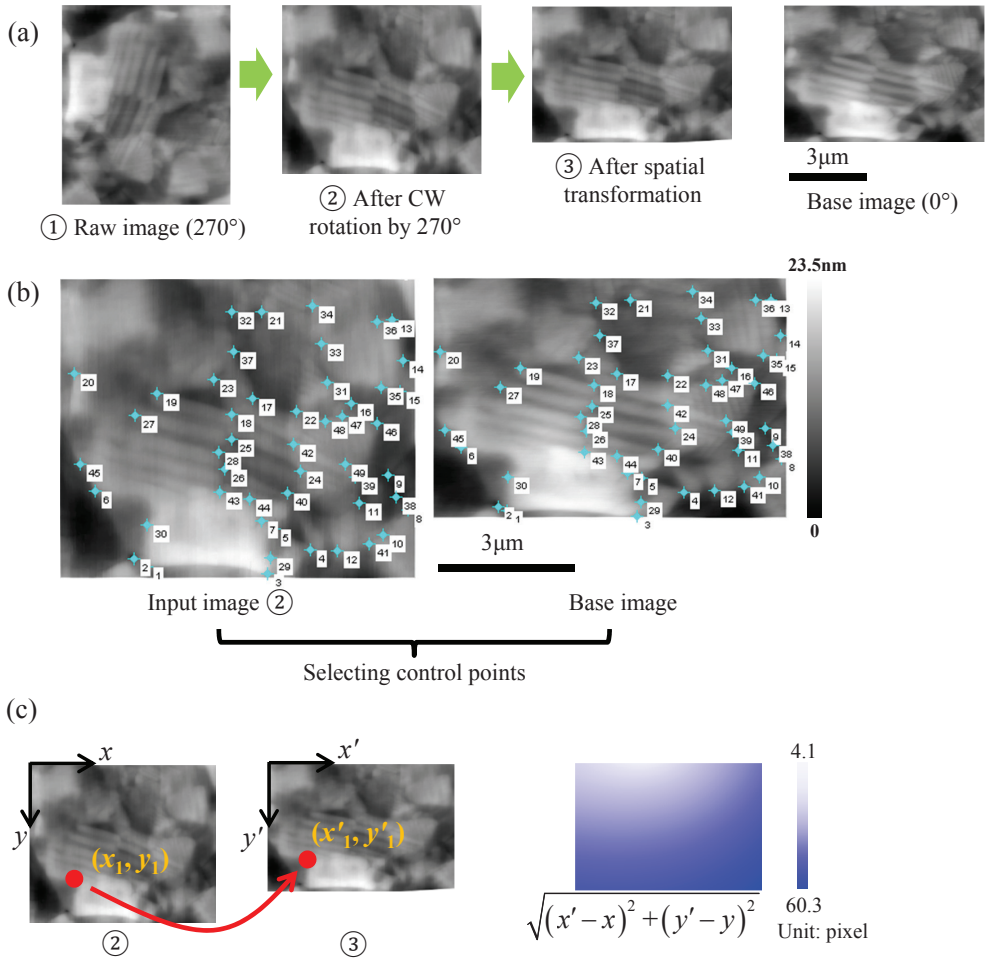

Figure 4.6: Image registration process for the raw AFM topography image taken from 270° sample orientation. (a) represents image registration process through (b) selecting control points to create the transformation matrix, and (c) shows pixel displacement during spatial transformation for the every pixel in image 3.

similarity to the base image. The same transformation was then applied to the LPFM image. Over all 11 LPFM images except for the base image, the mean pixel displacement was in the range 7.7–30.1 pixel, with the 270° image shown being the worst case. Figure 4.6(c) shows details of the spatial transformation in this worst case.

It was found that this image registration process gave sufficient agreement among the images to produce AR-PFM maps. Typically each pixel has a single phase reversal in any 180° sample rotation interval, suggesting that the pixel data is drawn from the same domain on the sample surface. Note, however, that a deficiency in the process is the use of the topography images; since the sample was polished flat, topographic features were

relatively indistinct. This can be seen in figure 4.6(b), where domain patterns show through the topography due to the slight variations in the polishing process caused by the crystallographic orientation. Much sharper images are obtained from the VPFM signal, which is also expected to be independent of sample orientation. Recently developed scanning probe microscopes are able to generate multiple signals at the same time, and hence VPFM, LPFM as well as topography images can be obtained simultaneously. Hence VPFM images with fine domain patterns could be used advantageously for selecting control points, where available.

4.4.2 LPFM phase images

The resulting LPFM phase images are shown in figure 4.7 with the orientation of the cantilever and the fast scan direction indicated above each image. It is evident from figure 4.7 that each pair of images taken with 180° difference in sample orientation have opposite LPFM phase signals. The lamellar patterns A and B from figure 4.5(e) are also indicated in figure 4.7; these patterns were most clearly exposed in the LPFM data at distinct sample orientations. Considering the LPFM images in the range $0° \le \theta < 180°$, lamellar pattern A is clearly exposed at $\theta = 120°$ while the contrast between these lamellae is almost indistinguishable in 0°, 30°, and 60° orientations. Meanwhile, lamellar pattern B is visible at 0° and 150°, but is indistinct at other orientations. There is no single orientation clearly exposing lamellar patterns A and B at the same time. This illustrates the point that a single LPFM scan cannot reliably expose the domain patterns present in a randomly oriented sample. In fact, even a pair of LPFM images taken from this region at orthogonal angles may not clearly expose both lamellations, see LPFM images at $\theta = 30°$ and $\theta = 120°$. This suggests the use of AR-PFM with angle increments less than 90° to reliably expose domain patterns.

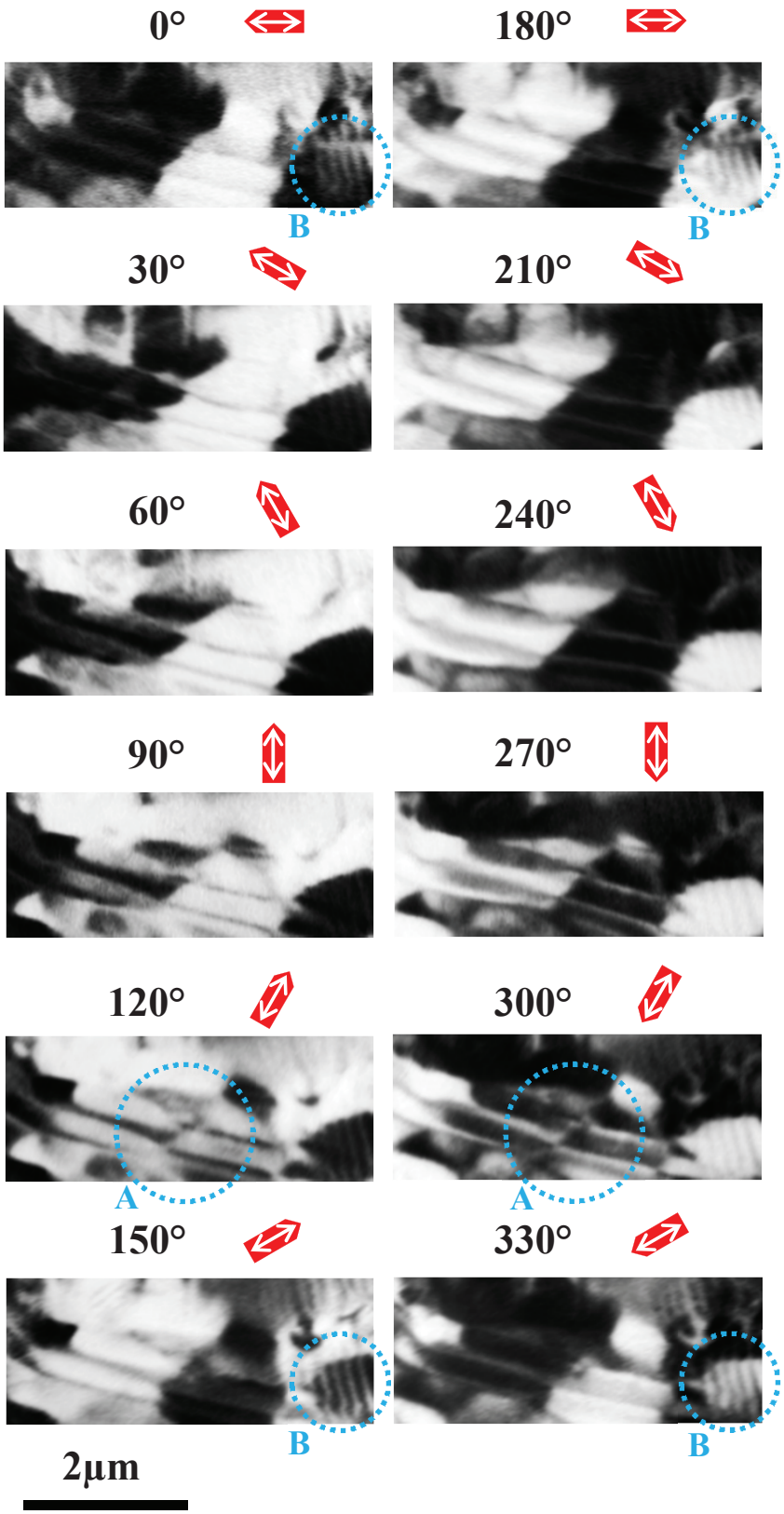

Figure 4.7: Twelve LPFM images collected during a 360° sample rotation.

4.4.3 AR-PFM maps

An AR-PFM map was created using the spatially transformed LPFM data set of figure 4.7. To generate the map, we seek for each pixel, the angle at which phase reversal occurs during sample rotation. This corresponds to the angle at which the lateral surface displacements excited by the converse piezoelectric effect are aligned with the cantilever. Phase reversal of the LPFM signal occurs twice during a 360° sample rotation. Hence, labelling the LPFM phase signal as $f(\theta)$, there are two angles at which $f(\theta) = 0$. Define θ_{N} as the angle at which $f(\theta) = 0$ with $df/d\theta < 0$.

The AR-PFM maps made use of twelve colour codes in figure 4.8(b) corresponding to twelve rotation segments. The orientation of each angular segment corresponds to the spatial axis of the measured surface displacements in the images. Accordingly, each segment aligns with the axis of motion of the cantilever tip relative to the sample.

Two distinct methods were used to estimate the angle θ_{N} for each pixel. The first method uses the first Fourier coefficient of $f(\theta)$, F_1 , given by $\theta_0 = \arctan\left(\mathrm{Im}(F_1)/\mathrm{Re}(F_1)\right)$ where $F_n = (1/2\pi)\int_{-\pi}^{\pi} f(\theta)\mathrm{e}^{-in\theta}d\theta$. Since we expect $f(\theta+\pi) = -f(\theta)$, and have samples at intervals $\Delta\theta$, F_1 was approximated using

$$F_1 = \frac{\Delta\theta}{\pi}\sum_{k=0}^{5} f(k\Delta\theta)\mathrm{e}^{-ik\Delta\theta}. \qquad (4.4)$$

The resulting AR-PFM map of the region of interest is shown in figure 4.8(a). An alternative method for identifying θ_{N} is to search for a pair of successive rotation angles between which $f(\theta)$ changes sign from positive to negative. Once again, expecting that

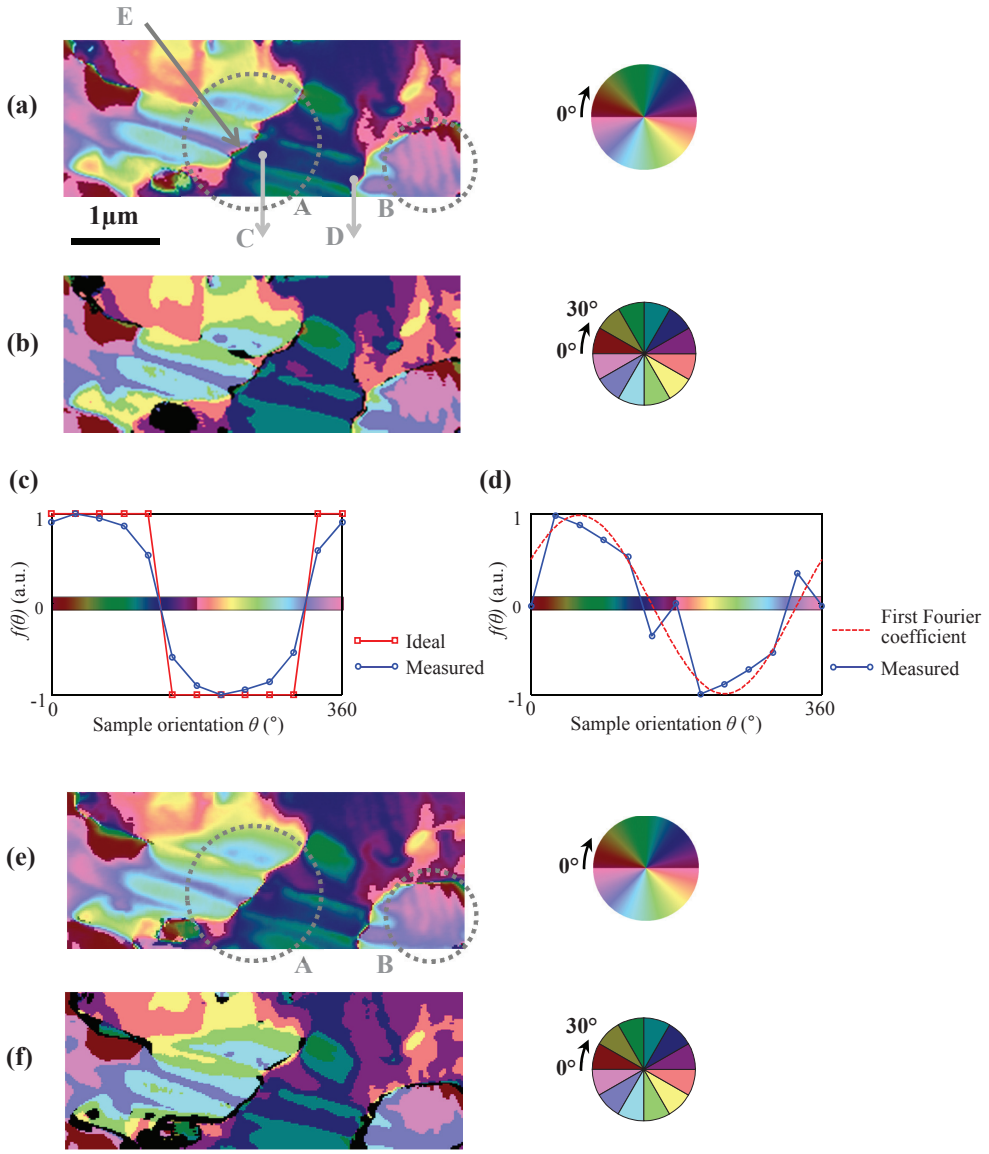

Figure 4.8: AR-PFM maps using (a),(e) the first Fourier coefficient, in full spectrum, and (b),(f) only rotation segment in which phase reversal occurs in LPFM signal. (a) and (b) were mapped using data from $0° \le \theta < 180°$ and (e) and (f) were mapped using data from $180° \le \theta < 360°$. (c) and (d) illustrate examples of signal variations corresponding to the two pixels C and D in (a), respectively.

$f(\theta+\pi) = -f(\theta)$ the process can be carried out using only those images with $0° \le \theta < 180°$. This gives rise to discrete θ_N values in 30° increments, see figure 4.8(b). In this case, black colouring was used to indicate the presence of more than one phase reversal within $0° \le \theta < 180°$. This could occur due to errors in image registration, and affected 4.5% of the pixels, mostly close to the junctions of domains. This second method

is advantageous in sharply defining domain boundaries when the surface displacement vector rotates through an angle greater than 30° between domains.

Figures 4.8(c) and (d) illustrate the normalized LPFM signal variations $f(\theta)$ from two pixels in figure 4.8(a) marked C and D, respectively. In figure 4.8(c) the signal is typical in that phase reversal occurs twice during 360° rotation. The ideal phase signal consists only of ±1 values as shown, making a sharp transition at the phase reversal angle. However, the measured data show a more gradual transition, which can be attributed to the presence of a system-inherent background signal [134]. Figure 4.8(d) relates to a pixel on the border between two domains, and shows an example where $f(\theta)$ has more than two zeros. This results in black pixel colouring in figure 4.8(b). However, the first Fourier coefficient can still be estimated through equation (4.4), demonstrating an advantage of the method used to generate figure 4.8(a).

Figures 4.8(e) and (f) correspond exactly to figures 4.8(a) and (b) except that the data range used was $180° \le \theta < 360°$. These AR-PFM images illustrate the accuracy of the assumption that $f(\theta + \pi) = -f(\theta)$: the r.m.s. angular error between pixels in figure 4.8(a) and figure 4.8(e) is 27.3°. The errors arise due to three main reasons: Firstly, misalignment of image features after image registration would cause errors near domain walls. Secondly, since the scan direction on the sample surface is reversed by a 180° rotation, asymmetric topography features can produce artefacts that would change upon 180° rotation. Finally, tip wear over the course of several scans causes a change in tip radius [132], and hence can affect the nature of the electrical contact driving the piezoelectric response of the surface.

The AR-PFM map reveals the lamellar patterns in region A that were identified by VPFM in figure 4.5(e). This pattern can now be clearly seen as two sets of non-180° lamellae, separated by a 180° domain wall (marked E in figure 4.8(a)). The 180° wall at E

separates domain pairs with $\theta_N \sim 135°$ and $\theta_N \sim 315°$, and domain pairs with $\theta_N \sim 105°$ and $\theta_N \sim 285°$. Similarly, the finer domain bands from region B of figure 4.5(e) appear as non-180° lamellae. In region B the lamellations are sufficiently fine (spacing about 80 nm) that they are not clearly resolved in figure 4.8(b), although the Fourier coefficient method of figure 4.8(a) resolves them. Overall this suggests that the spatial resolution achieved with AR-PFM is poor relative to typical SPM measurements, and this can be attributed to the difficulty of maintaining image registration across a wide range of sample rotation angles. The benefits of the method therefore lie in the quantitative orientation data obtained. Next consider two aspects of the orientation data revealed by AR-PFM. First the relationship between surface displacements and the underlying polarization direction will be considered. Then the ability to discriminate between the rhombohedral and tetragonal phases of PZT will be explored.

4.5 Correlating lateral surface displacement and polarization direction

Making use of the EBSD data, we are now in a position to compare the surface displacement directions from the AR-PFM measurements with the polarization directions in the underlying crystal. To do this, the EBSD data is first used to find the Euler angles of pseudo-cubic axes corresponding to the crystallographic orientation of the sample region of interest. Then, by comparing the intersections of the {110} and {100} planes with the sample surface, the set of possible orientations for non-180° domain walls is identified. For example, region A, figure 4.9(a) contains several domain walls that are closely aligned only with the (101) plane: we infer that these are non-180° domain walls with a (101) habit plane. Hence the domain wall normal **n** is known. Next, from the

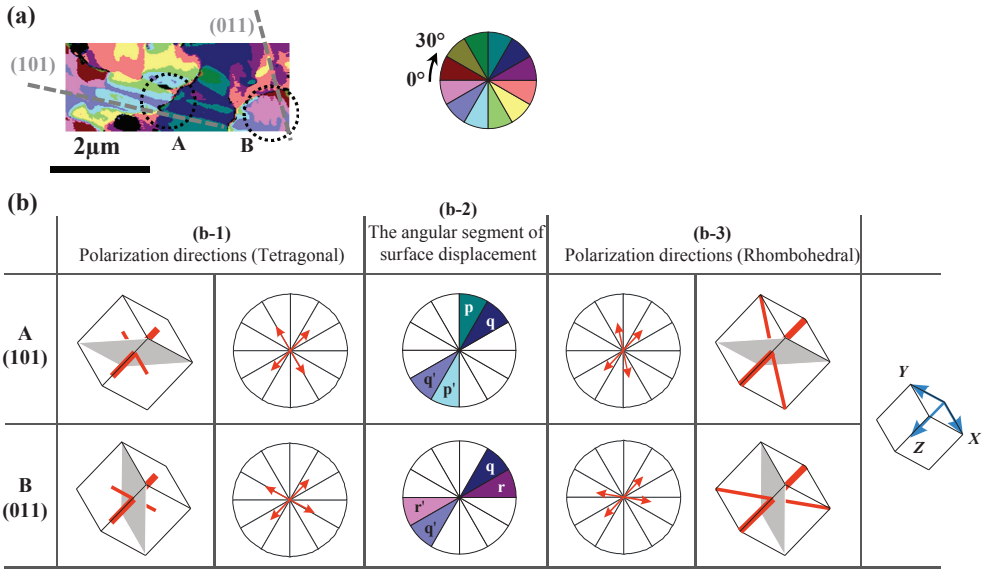

Figure 4.9: (a) shows AR-PFM plot and a colour pie. (b) represents a discrepancy between axis of the lateral surface displacement and in-plane polarization direction using AR-PFM and EBSD data.

theory of compatibility (equations (1.1) and (1.2)) and knowing that the possible polarization directions are limited to <100> for the tetragonal phase or <111> for the rhombohedral phase, we can infer the possible domain pairs separated by the (101) plane. Figure 4.9(b) shows the orientation of the crystallographic axes, possible polarization directions in the tetragonal and rhombohedral phases, and their projections into the plane of the sample surface. Meanwhile, the 30° rotation segments of surface displacements are identified using AR-PFM and shown in (b-2), figure 4.9(b). A similar analysis is carried out for region B of figure 4.9(a), which shows non-180° domain walls with a (011) habit plane. In both cases there is a clear discrepancy between the projection of the polarization directions into the sample surface plane and the measured direction of lateral surface displacements. This is significant because the PFM response is often taken to indicate the underlying polarization direction [126,130]. However, a discrepancy between the directions is expected from consideration of the tensorial nature of the piezoelectric effect [135], and is indeed observed in our measurements. Similar observations were made by Jungk *et al.* [125].

4.6 Identification of rhombohedral/tetragonal phase

In alloys such as polycrystalline near morphotropic PZT, the presence of randomly oriented grains, multiple phases, and many distinct domain types adds great complexity. Individual analytical techniques, such as X-ray diffraction, give only part of the story, and typically, the use of multiple techniques is needed to characterise grain, phase, and domain structure. In this section, it is demonstrated that AR-PFM can allow identification of the phases and domain structures present at the sub-grain scale in PZT, using another region in the same material.

4.6.1 Application of AR-PFM to another region in the PZT

Figures 4.10(a)–(c) show the AFM topography, VPFM, and EBSD image quality data, respectively, for another region of interest. Triple junctions appear as dark spots in figure 4.10(a) and can be identified as the intersections of grain boundaries in figure 4.10(c). Figure 4.11 shows an enlarged VPFM image corresponding to the region within the rectangle marked in figure 4.10(b). This region comes from within a single grain, except for two small regions in the upper corners marked GB, and has a uniform crystal orientation. Straight and curvy lines are non-180° and 180° domain walls, respectively, as noted in chapter 1. Non-180° domain structures seen in figure 4.11, include the broadly spaced lamellar pattern H and the herringbone pattern I–J. A wavy 180° domain wall, M, can be also observed at the centre of the lamellar pattern H. Although the VPFM image shows contrast between the lamellae of non-180° domain structures, the data do not provide sufficient information to identify the 3D axis of the piezoelectric response. For example, in figure 4.11, regions H and I both contain domains in light contrast but these cannot be confirmed as having similar polar axis. Similarly, the

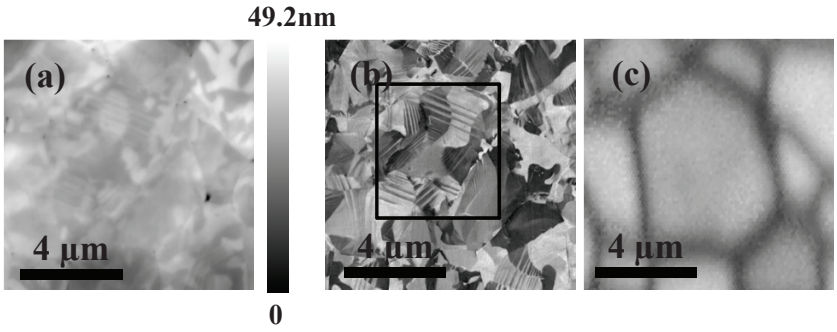

Figure 4.10: The region of interest, shown through (a) AFM topography, (b) VPFM; a rectangle marks the region enlarged in figure 4.11, (c) EBSD image quality map.

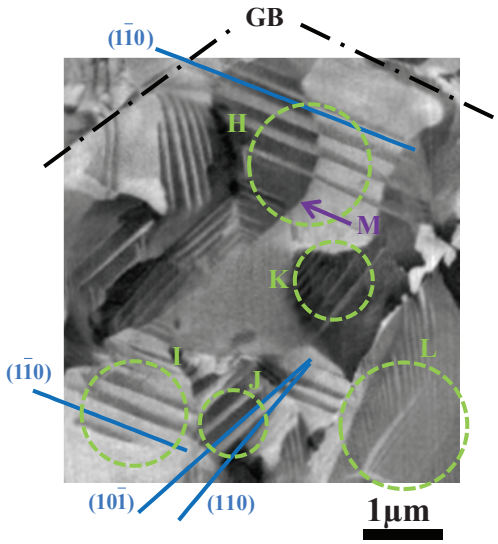

Figure 4.11: Lamellar and herringbone domain patterns and identification of crystallographic planes in VPFM image using EBSD.

laminations at J and K have matching orientation of domain walls, but the polar axes of the individual domains cannot be identified from VPFM alone. Note also that the region L in figure 4.11 shows almost uniform contrast. In fact a distinct banded structure will appear when this region is studied using AR-PFM. Crystallographic planes shown in figure 4.11 were identified by EBSD and will be discussed later.

Figures 4.12(a)–(f) show six LPFM phase images corresponding to the same region as that shown in figure 4.11. Each image was taken after rotating the sample through a multiple of 30°. Since phase reversal in the LPFM signal always occurs once during a 180° sample rotation [128], the six images are sufficient to capture the full range

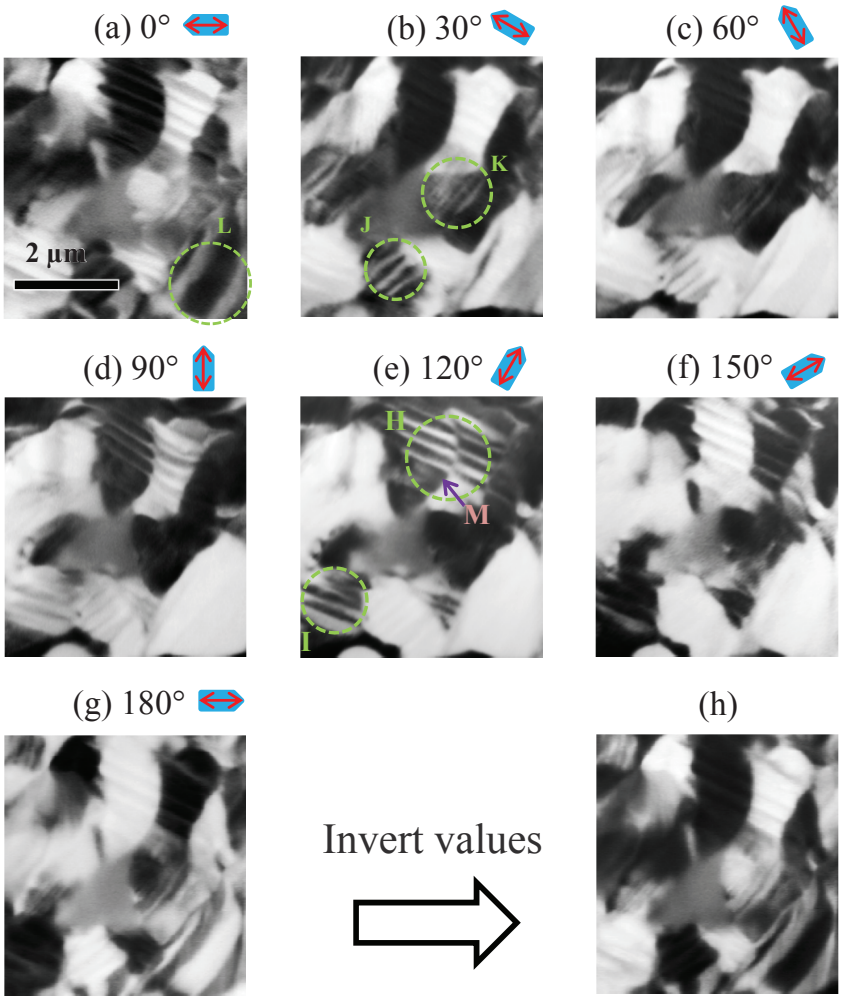

Figure 4.12: LPFM phase images acquired after sample rotations. The scales in (b)–(h) are the same as in (a). The cantilever orientation and fast scan direction are shown above each image.

of signal variation. Figure 4.12(g) shows the LPFM image after 180° sample rotation. As figure 4.12(h) illustrates, the LPFM image inverted from figure 4.12(g) is almost the same with figure 4.12(a). The five LPFM images taken at 30°–150° sample orientations were registered based on the LPFM image from 0° *via* the same method introduced in figure 4.6.

In figure 4.12(e) it can be seen that, at a sample rotation of 120°, the lamellar structure H becomes distinct in the LPFM image. However, there is no single LPFM phase image making clear both parts of the herringbone pattern I–J of figure 4.11: The lamellae at I are most distinct in figure 4.12(e) while those at J appear in figure 4.12(b).

Meanwhile, region L, which showed only weak contrast in VPFM appears as distinct stripes in figure 4.12(a). Of interest, figure 4.12(c) and figure 4.12(f) show LPFM images taken with a 90° relative sample rotation, but neither image shows this striped pattern in region L. Since this pattern did not appear in VPFM either, we can infer that there are three orthogonal directions in which the piezoresponse signal did not identify the domain structure. Hence, the 3D PFM technique, which is sometimes used to identify polarization direction, may not have shown the domain structure revealed by AR-PFM in this region. Figure 4.13(a) shows a map of angle θ_N over the LPFM image plane according to the colour code shown. Figure 4.13(c) shows essentially the same data as figure 4.13(a) except that angle θ_N was found by considering the phase of the first Fourier coefficient of $f(\theta)$ in equation (4.4). It can be confirmed that the map in figure 4.13(a) is advantageous in visualizing domain walls while figure 4.13(c) provides more subtle detail of signal variation. Thus, these two methods can be complementary to each other. The AR-PFM map can also be produced using smoothed data. One method is to use the sum of the signals in the corresponding pixel and the surrounding pixels within the distance of two pixels as shown in figure 4.13(e). This method could prevent wrong θ_N values that occur due to slight misalignment between images. Figures 4.13(a) and (c) were produced based on only the central pixel while figures 4.13(b) and (d) were generated using the sum of the data in the central pixel and the surrounding pixels. Some regions including N in figures 4.13(b) show noticeable difference between these two methods. Except for such minor difference, the resulting images from this method show almost the same result with figures 4.13(a) and (c), and appear not to significantly change the image quality. A drawback of this method is that this deteriorates the resolution of AR-PFM map.

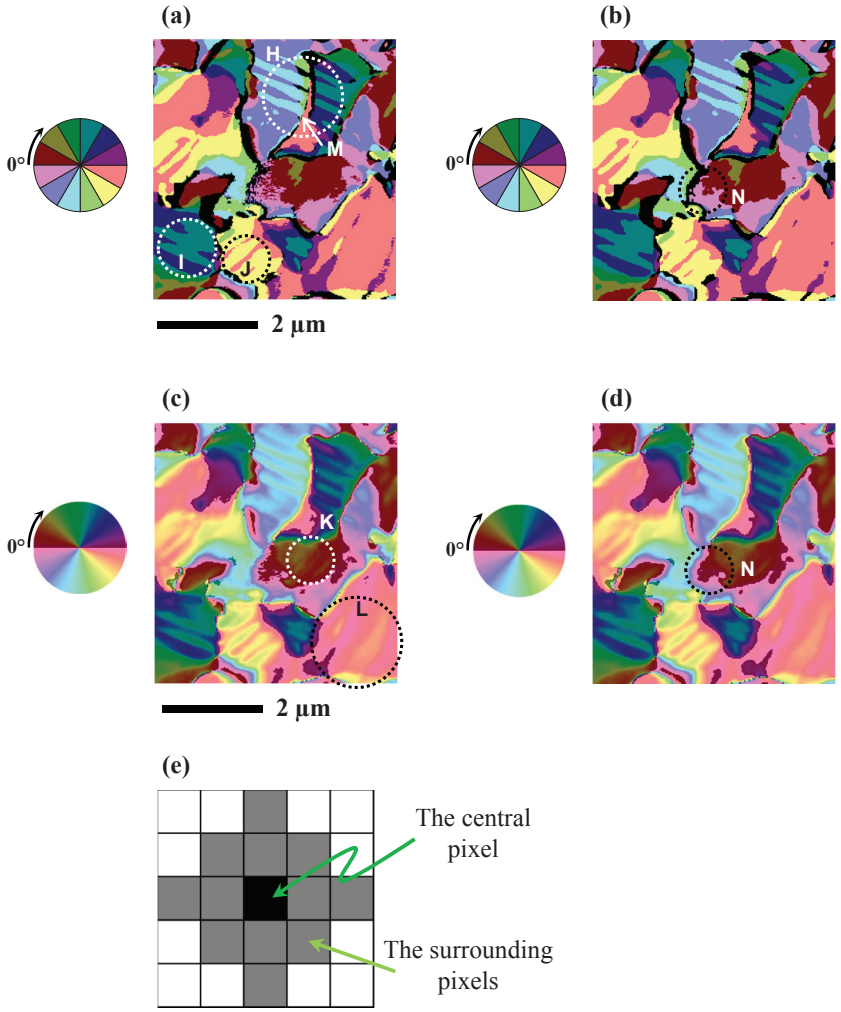

Figure 4.13: AR-PFM maps using (a)–(b) rotation angle at which phase reversal occurs and (c)–(d) the first Fourier coefficient, F_1, in full spectrum. Black pixels in (a)–(b) represent regions in which phase reversal occurs more than one time. While (a), (c) were produced by only considering the central pixel in (e), the sum of the signals including the surrounding pixels was considered to generate (b), (d).

The maps in figure 4.13 condense information from the AR-PFM data set. This helps to make clear features such as the presence of multiple domain bands at L, which was not visible in the LPFM images from most rotation angles. These maps also enable us to discriminate between regions that appear similar in VPFM data but in fact have differently oriented piezoelectric response. For example, in figure 4.13(a), the region marked H consists of two laminations separated by a 180° domain wall, marked M. We can infer that M is a 180° wall because it appears curved. However, figure 4.13(a)

explicitly identifies a jump in orientation of 180° as boundary M is crossed. Laminations to the right of M have θ_N values in angle bins 90°–120° and 120°–150°. On the left of boundary M the corresponding θ_N values are in angle bins 270°–300° and 300°–330°. It also becomes evident that the lamination at I is matched in orientation with the lamination to the right of boundary M in region H, which was not shown by the VPFM signal. Similarly, regions J and K consist of laminations with matching orientation (see figure 4.11). The AR-PFM data in figure 4.13, however, identify that these regions contain distinct domain types, with relative rotation of 180° – that is, the domains in J are antiparallel to those in K.

4.6.2 Phase identification

A further use of the AR-PFM maps is to assist in discriminating between the tetragonal and rhombohedral phases in PZT. For example, noting that the data in figure 4.13 are taken from within a single grain, consider the laminations in region I and J. Each of these consists of two distinct colours in the AR-PFM map, with no common orientation or antiparallel orientations. Hence regions I and J show four distinct axes of piezoelectricity. Since this is not possible in the tetragonal phase (with only three distinct axes) the region must be rhombohedral.

To confirm this interpretation, the Euler angles 175.4°, 49.2°, 290.2° measured by EBSD were used to identify the crystallographic planes corresponding to the domain walls in each lamination (see figure 4.11 for detail). In lamination I, the domain walls lie in $(1\bar{1}0)$ planes, while in lamination J, the domain walls may be $(10\bar{1})$ or (110) planes, to within the instrument tolerance. All of these planes can form domain walls in either the tetragonal or the rhombohedral phases. However, in the tetragonal phase, the polarization variants that can meet compatibly across these domain walls must contain pairs of

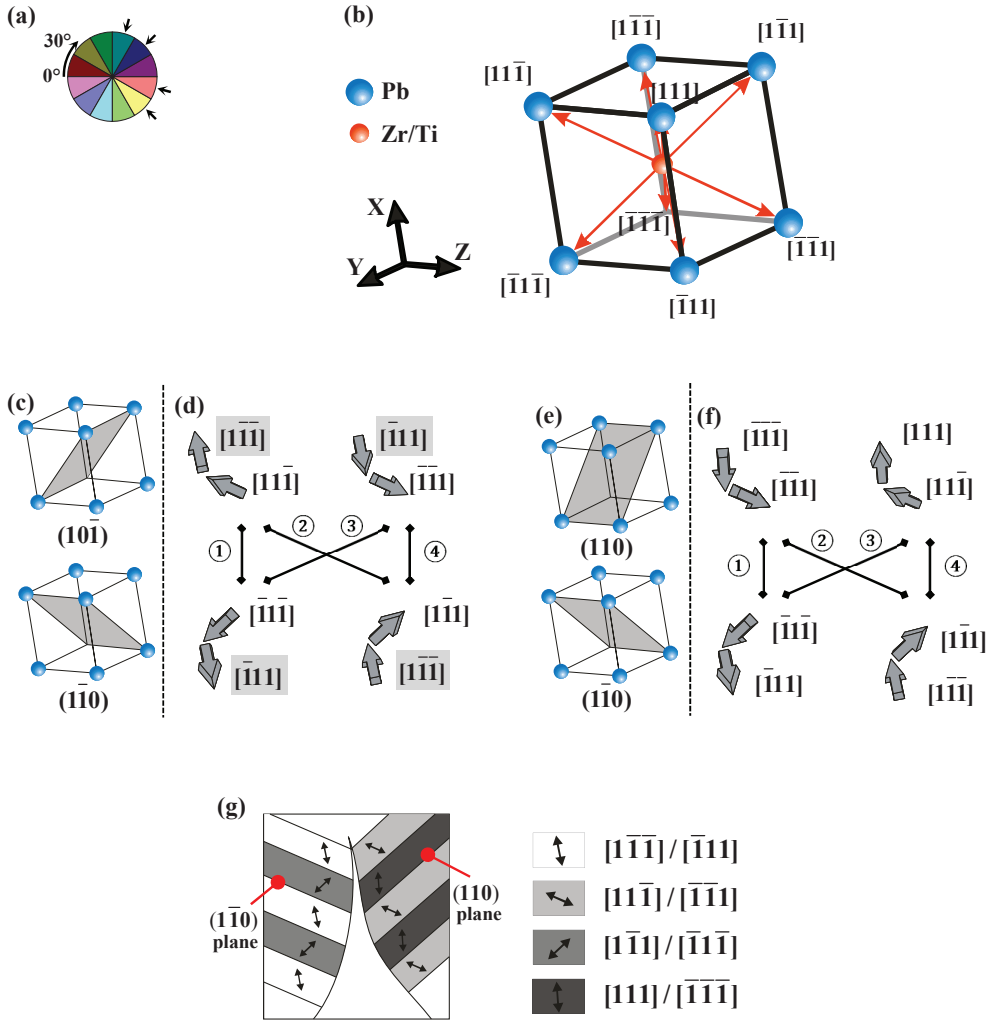

Figure 4.14: (a) The four orientations corresponding to the herringbone pattern I–J in figures 4.13. (b) Crystal coordinate system from EBSD, showing the eight <111> polarization directions of the rhombohedral phase. (c) A 3D view of the possible domain wall orientations of the herringbone domain pattern. (d) Possible polarization directions for each plane in (c). (e) Another 3D view of possible domain wall orientations of the herringbone domain pattern. (f) Possible polarization directions for each plane in (e). (g) Interpretation of polarization variants in region I–J in figure 4.13.

polarization directions that are either parallel or antiparallel. Thus region I–J cannot be tetragonal. Furthermore, in the rhombohedral phase, the combination of a domain wall in the $(1\,\bar{1}0)$ plane, and a domain wall in the $(10\,\bar{1})$ plane also guarantees the presence of polarization variants that are parallel or antiparallel as figures 4.14(c)–(d) show. The only remaining possibility is that the region is rhombohedral with $(1\,\bar{1}0)$ domain walls in lamination I and (110) domain walls in J. Figures 4.14(e)–(f) show that any pair among

the four possible combinations of polarization directions guarantees four distinct polarization axes in the herringbone pattern I–J. This interpretation of the domain structure is illustrated in figure 4.14(g). This shows that the angle resolved data can provide clear discrimination between the tetragonal and rhombohedral phases, provided that a sufficiently rich pattern of laminations is present.

4.7 Conclusion

The present chapter described a method for obtaining and analysing AR-PFM data. The method was applied to the identification of ferroelectric domain structure in near-morphotropic PZT. The use of image registration to correct for distortion caused by piezo-scanner artefacts was demonstrated. Ferroelectric domain patterns were mapped by using the angle of phase reversal in the LPFM signal during sample rotation. The resulting AR-PFM maps enable clear identification of ferroelectric domain patterns by colouring domains according to the orientation of the surface displacements due to the converse piezoelectric effect. In addition, using AR-PFM and EBSD data in conjunction, the method was able to show discrepancy between the direction of lateral surface displacement and the in-plane component of the polarization direction. The AR-PFM method also provided data that enabled discrimination between the tetragonal and rhombohedral phase. This technique can be applied to a wide range of piezoelectric materials including thin films [126,130], biological systems [136–139], and also is applicable to microscopies based on locally induced strain measurement, such as electrochemical strain microscopy (ESM) [140,141].

After recognizing the opportunity provided by LPFM for studying domain structures, the instruments for LPFM were installed during this doctoral research. Thus, the AR-PFM method was not applied to study the evolution process of ferroelectric

domains. But, it is believed that AR-PFM can be a very powerful technique for studying the evolution of ferroelectric domain patterns. So this is a suggested area for further work.

Chapter 5. Monte Carlo simulation of ferroelectric domain evolution

A Monte Carlo simulation method is developed that can generate domain structures typical of ferroelectrics and model their evolution. After studying how energy terms influence the domain patterns that form, this modelling method was tested in various ways. First, compatible domain patterns similar to those that are typically observed from PFM images were generated, starting from randomly assigned polarizations in a lattice. Second, the stability of compatible and incompatible domain patterns was tested in the absence of loading. Third, for the compatible and partly incompatible domain patterns, electric field and mechanical stress were applied to induce domain evolution. The simulation results showed that polarization switching happened *via* domain wall motion, and polarization switching was restricted by the pre-existing domain patterns. This chapter illustrates that the pattern evolution of ferroelectric domains can be reproduced by a Monte Carlo simulation method, and presents initial steps towards an electro-mechanical coupled Monte Carlo model.

5.1 Introduction

In chapters 2 and 3, the evolution processes of ferroelectric domains were observed using PFM and their mechanisms were discussed. From the experimental works, it was confirmed that domain switching occurs *via* pattern evolution, and the evolution processes are constrained by the pre-existing domain structure. In this chapter, a model

based on Monte Carlo methods is developed to reproduce typical features in the evolution processes of ferroelectric domains. The concept of Monte Carlo simulation was introduced in chapter 1 where it was noted that the method has several advantages: these include ease of set-up, since there was already good existing algorithms, and ability to escape from local energy minimum states.

The early works on ferroelectric domains using Monte Carlo methods were based on an Ising or Q-state Potts model that simulates phase transitions *via* lattice statistics [142,143]. For example, the total energy of the system is expressed using a Hamiltonian consisting of a Potts part that describes interacting polarization states [144] and a static electric energy part [142]. Domain nucleation and growth were reproduced from this model. However, the energies of a grain boundary and a domain boundary were treated equally, which is an unrealistic assumption. In contrast to the Potts model, a lattice-based Monte Carlo method was developed by Potter *et al.* [145] to study ferroelectric domain evolution under applied electric field. In this model, four in-plane polarization directions were randomly assigned to 20 × 20 lattice points at the initial configuration. The total free energy was developed based on electrostatic terms including dipole-dipole interactions, local polarization gradients, and the effect of applied electric field. The resulting domain configurations showed typical domain structures that can be found in tetragonal ferroelectrics. However, no elastic strain energy was considered in this model. Xue *et al.* [146] developed this model by including elastic strain energy and electrostrictive energy. Their model is based on a phenomenological description of the free energy often used in the phase field method [88,92], but the simulation was carried out by the Metropolis algorithm [94] instead of using the TDGL equation. Xue *et al*. [146] did not allow for external electro-mechanical loading in their model.

In the present work, the Metropolis algorithm will also be used. The sequence of the Metropolis algorithm is as follows [94,147]:

1. An initial configuration (A) is set up and its total energy (E_A) is calculated.
2. A second configuration (B) is generated using input from a pseudo-random number generator, resulting in the new total energy (E_B).
3. A transition probability (P) is calculated as follows:

$$P = \begin{cases} \exp\left(\dfrac{-\Delta E}{k_B T}\right) & \text{for } \Delta E > 0 \\ 1 & \text{for } \Delta E \le 0 \end{cases} \tag{5.1}$$

where $\Delta E = E_B - E_A$, k_B is the Boltzmann constant, and T is absolute temperature. This algorithm allows the configuration to transit from the initial configuration A to the second configuration B if $\Delta E \le 0$. Conversely, if $\Delta E > 0$, the probability of the transition (P) is compared with a random number R between 0 and 1. The transition to the second configuration B is allowed only if $P > R$. The details of the algorithm are discussed in section 5.4.

In the present work, the evolution of domain patterns is studied based on a total energy formulation similar to that used by Xue *et al*. [146], except that additional energy terms for an externally applied electric field and a mechanical stress are also considered. The evolution of domain patterns is studied using this model, and the similarity and discrepancy between the simulation result and the experimental observation are discussed.

5.2 Model description

Developing a model for PZT material would make a direct comparison between the model and experiment possible. However, in PZT the phase can be tetragonal or

rhombohedral, depending on subtle ways on temperature, stress, electric field, and the compositional ratio between Zr^{4+} and Ti^{4+} ions. The complex nature in this material is a major modelling challenge. Therefore, in this work, as a starting point, a 2D model of the tetragonal phase, transformed from a high temperature cubic phase is used as a reference system. Thus, when computing the total free energy, the cubic phase serves as the ground state. The model is somewhat similar to $BaTiO_3$ in the tetragonal phase which is less complex than near-morphotropic PZT. Modelling based on Monte Carlo method has been developed for $BaTiO_3$ by the early work [146] , which provides a good guideline for selecting parameters. Thus, there is a limit to directly compare simulation results to the domain evolution processes of the PZT observed from chapter 2 and 3. This chapter focuses on reproducing typical domain evolution processes in ferroelectrics such as the domain broadening process using the parameters used in barium titanate in tetragonal phase rather than reproducing the domain evolution processes observed from the PZT using PFM.

The 2D model consisting of a set of points in a square array is shown in figure 5.1. Each point is allowed a state consisting of a polarization vector and a displacement vector (corresponding to the central cation displacement in a tetragonal perovskite). In this model, only four in-plane polarization vectors and displacement vectors are allowed. Thus, two distinct $m \times m$ arrays $\boldsymbol{P}$ and $\boldsymbol{u}$ consisting of four values 0, $\pi/2$, π, $3\pi/2$ are generated for the computation. The array $\boldsymbol{P}$ represents polarization vectors and $\boldsymbol{u}$ represents displacement vectors. Because each two displacement vectors correspond to the identical strain state, each lattice point can have one of eight possible combinations of a polarization vector and a strain state, see figure 5.1.

In a lattice-based simulation, one lattice point could represent one unit cell in the actual material. Then, noting that the lattice parameter is ~4.0 Å but domains are typically

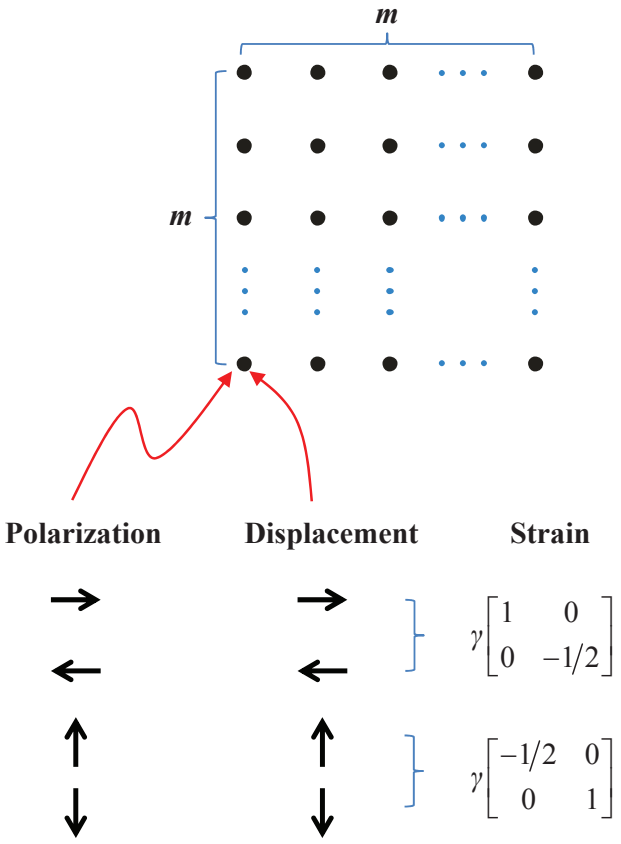

Figure 5.1: A crystalline lattice consisting of m^2 points. Each lattice point has a polarization vector and a displacement vector. Pairs of displacement vectors correspond to the same strain state. Note that γ is material property.

>100 nm in width, to reproduce a realistic simulation, a large number of lattice points are required. Alternatively, one lattice point could be taken to represent a finite volume consisting of many unit cells. The finite volume then represents a group of unit cells switching together. Thus, one lattice point represents a pseudo grain. This has the advantage that a smaller set of lattice points is used, giving a faster simulation. But a disadvantage is that it becomes less clear as to exactly what physical quantities are represented by the state at a lattice point. Energies, local interactions and kinetics will depend on the size (and shape) of the finite volume. Here, a finite volume approach is used, and to avoid the consequent difficulty of specifying physical parameters, all the simulations were performed in dimensionless units. A unit of length defined by two

closest lattice points is one lattice unit [145]. All the parameters used in the energy terms are in dimensionless units, and scaling factors are employed to balance the magnitude between each energy. The result is that the model is ambiguous concerning true physical length scales, time scales and field magnitudes. But it will be demonstrated that it can produce behaviour similar to observations of real materials. Note that this simulation work was carried out using Fortran programming language.

5.3 Phenomenological approach

The total free energy of the material can be represented as

$$F_{\text{tot}} = f_{\text{e}} + f_{\text{es}} + f_{\text{dip}} + f_{\text{g}} + f_{\text{E}} + f_{\text{S}}, \tag{5.2}$$

where f_{e} is the elastic strain energy, f_{es} is the electrostrictive energy, f_{dip} is the free energy of dipole-dipole interaction, f_{g} is the local gradient energy, f_{E} is the free energy due to externally applied electric field, and f_{S} is the free energy due to the externally applied stress. In this section, each energy term in equation (5.2) is introduced.

5.3.1 Elastic strain energy

The phase transition from cubic to tetragonal involves a structural transformation including a change in lattice parameter as well as the generation of spontaneous electrical polarization. The resulting elastic strain energy can then be represented as [148]

$$f_{\text{e}} = \frac{1}{2} C_{ijkl} e_{ij} e_{kl}, \tag{5.3}$$

where C_{ijkl} is the elastic tensor, and e_{ij} is the elastic strain tensor. The elastic strain is given by $e_{ij} = e_{ij}^{\text{tot}} - e_{ij}^{0}$ where e_{ij}^{0} is the spontaneous strain state and e_{ij}^{tot} is the total strain, given by $e_{ij}^{\text{tot}} = \left(\partial u_i / \partial x_j + \partial u_j / \partial x_i\right) / 2$. Using matrix notation with Voigt abbreviation ($e_1 = e_{11}$, $e_2 = e_{22}$, $e_3 = e_{33}$, $e_4 = 2e_{23}$, $e_5 = 2e_{13}$, $e_6 = 2e_{12}$), equation (5.3) can be represented in three dimensions as

$$\begin{aligned} f_{\text{e}} &= \frac{1}{2} C_{\alpha\beta} e_\alpha e_\beta \\ &= \frac{1}{2} C_{11}(e_1^2 + e_2^2 + e_3^2) + C_{12}(e_2 e_3 + e_1 e_3 + e_1 e_2) + \frac{1}{2} C_{44}(e_4^2 + e_5^2 + e_6^2). \end{aligned} \tag{5.4}$$

where $C_{11} = C_{1111}$, $C_{12} = C_{1122}$, and $C_{44} = C_{1212}$. Refer to appendix A.3 for the matrix of elastic tensor in the cubic phase. In two dimensions, equation (5.4) reduces to

$$f_{\text{e}} = \frac{1}{2} C_{11}(e_1^2 + e_2^2) + C_{12}(e_1 e_2) + \frac{1}{2} C_{44}(e_6^2). \tag{5.5}$$

The spontaneous strain states in tetragonal can be represented in two dimensions as

$$\begin{aligned} \boldsymbol{\varepsilon}_{\mathbf{a}} &= \gamma \begin{pmatrix} 1 & 0 \\ 0 & -\frac{1}{2} \end{pmatrix}, \\ \boldsymbol{\varepsilon}_{\mathbf{b}} &= \gamma \begin{pmatrix} -\frac{1}{2} & 0 \\ 0 & 1 \end{pmatrix}, \end{aligned} \tag{5.6}$$

where γ is a material property. The relationship between displacement vectors and strain states is shown in figure 5.1. In the present work the simplifying assumption is made that the total strain at each lattice point is identical to one of the spontaneous strain states. Under this assumption, switching state between ε_{a} and ε_{b} produced no change in energy

f_e, so the elastic strain energy contribution does not affect the model. However, this term would become significant if phase changes or varying stresses were included in the model.

5.3.2 Electrostrictive energy

The elastic strain energy is coupled with polarization *via* the electrostrictive energy term. This energy can be represented as [148]

$$f_{es} = -q_{ijkl} e_{ij} P_k P_l . \tag{5.7}$$

Using Voigt notation, this becomes

$$\begin{aligned} f_{es} &= -q_{11}(e_1 P_1^2 + e_2 P_2^2 + e_3 P_3^2) \\ &-q_{12}[e_1(P_2^2 + P_3^2) + e_2(P_1^2 + P_3^2) + e_3(P_1^2 + P_2^2)] - q_{44}(e_6 P_1 P_2 + e_5 P_1 P_3 + e_4 P_2 P_3), \end{aligned} \tag{5.8}$$

where P_1, P_2, P_3 are the components of polarization $\boldsymbol{P}_i$ and q_{ijkl} is electrostriction tensor. Note that in Voigt notation $q_{11} = q_{1111}$, $q_{12} = q_{1122}$, and $q_{44} = 2q_{1212}$. Refer to appendix A.3 for the matrix form of the electrostriction tensor. Equation (5.8) can reduce in two dimensions to

$$f_{es} = -q_{11}(e_1 P_1^2 + e_2 P_2^2) - q_{12}(e_1 P_2^2 + e_2 P_1^2) - q_{44}(e_6 P_1 P_2). \tag{5.9}$$

As explained in section 5.3.1, strain values e_1, e_2, and e_6 are obtained from an element *i* in the $\boldsymbol{u}$ array. P_1 and P_2 can be also directly obtained from an element *i* in the $\boldsymbol{P}$ array *via* $P_1 = \cos(\boldsymbol{P}_i)$ and $P_2 = \sin(\boldsymbol{P}_i)$. When $q_{11} > 0$ and $q_{12} < 0$, a coupling between $\boldsymbol{P}_i = 0, \pi$ and $\boldsymbol{u}_i = 0, \pi$, or a coupling between $\boldsymbol{P}_i = \pi/2, 3\pi/2$ and $\boldsymbol{u}_i = \pi/2, 3\pi/2$ will be energetically favourable. Thus the electrostrictive energy favours strain states that 'align' with the polarization state.

5.3.3 Dipole-dipole interaction energy

The potential energy for two interacting dipoles with polarization vectors $\mathbf{P}_i$ and $\mathbf{P}_j$ at lattice positions i and j is [145]:

$$f_{\text{dip}} = \sum_{i,j} K\left(\frac{\mathbf{P}_i \cdot \mathbf{P}_j}{r^3} - \frac{3(\mathbf{P}_i \cdot \mathbf{r})(\mathbf{P}_j \cdot \mathbf{r})}{r^5}\right). \tag{5.10}$$

Here K is a scaling factor, $\mathbf{r}$ is the vector in lattice coordinates that connects the two lattice points i and j, so r is the distance in lattice unit between the two lattice points. Note that because all the energies are represented in dimensionless units in this simulation, K is present to scale the quantity of f_{dip}. This energy exists between every polarization pair in a crystalline lattice. Therefore, we must sum f_{dip} over a range of r large enough, in principle, to cover the entire lattice. However, this is difficult to implement in simulations due to a large computation time. In fact, the f_{dip} contributions become almost negligible as r increases [145]. Therefore, a truncation distance of a few lattice unit is commonly used. Here a truncation distance of 6 lattice unit was applied when computing f_{dip}. Note that the dipole-dipole interaction tends to favour dipoles adopting opposite directions if they are in close proximity. It therefore favours the formation of 180° domain walls.

5.3.4 Local polarization gradient energy

The potential energy for dipole-dipole interaction tends to generate antiparallel alignment of polarization vectors (This is discussed further in section 5.5.2). Therefore, to generate ferroelectric domains, another energy term is introduced, penalizing sharp gradients in polarization. The local polarization gradient energy term provides this penalty for

differently oriented polarizations in neighbouring lattice points. Local gradient energy can be represented as [148]

$$f_{\mathrm{g}} = \frac{1}{2} G_{ijkl} P_{i,j} P_{k,l}, \tag{5.11}$$

where G_{ijkl} is a fourth order symmetric tensor, and $P_{i,j} = \partial P_i / \partial x_j$. Using Voigt notation, this becomes

$$\begin{aligned} f_{\mathrm{g}} &= \frac{G_{11}}{2}(P_{1,1}^2 + P_{2,2}^2 + P_{3,3}^2) + G_{12}(P_{1,1}P_{2,2} + P_{2,2}P_{3,3} + P_{1,1}P_{3,3}) \\ &+ \frac{G_{44}}{2}\left[(P_{1,2} + P_{2,1})^2 + (P_{2,3} + P_{3,2})^2 + (P_{3,1} + P_{1,3})^2\right], \end{aligned} \tag{5.12}$$

where G_{11}, G_{12}, G_{44} are the elements in the local gradient matrix, see appendix A.3. The local gradient coefficients can be measured using an inelastic neutron scattering method [148]. Equation (5.12) is reduced to two dimensions as

$$f_{\mathrm{g}} = \frac{G_{11}}{2}(P_{1,1}^2 + P_{2,2}^2) + G_{12}(P_{1,1}P_{2,2}) + \frac{G_{44}}{2}(P_{1,2} + P_{2,1})^2. \tag{5.13}$$

An alternative expression for f_{g} which allows the contribution of $\mathrm{P_{1,2}P_{2,1}}$ to be varied is [146]

$$f_{\mathrm{g}} = \frac{G_{11}}{2}(P_{1,1}^2 + P_{2,2}^2) + \frac{G'_{12}}{2}(P_{1,1}P_{2,2}) + \frac{G'_{44}}{2}(P_{1,2} + P_{2,1})^2 + \frac{G''_{44}}{2}(P_{1,2} - P_{2,1})^2, \tag{5.14}$$

as discussed in the reference [148]. To avoid fitting four distinct parameters in equation (5.14), a simpler form was assumed as follows:

$$f_{\mathrm{g}} = J\left[(P_{1,1}^2 + P_{2,2}^2) + (P_{1,1}P_{2,2}) + (P_{1,2} + P_{2,1})^2 + (P_{1,2} - P_{2,1})^2\right]. \tag{5.15}$$

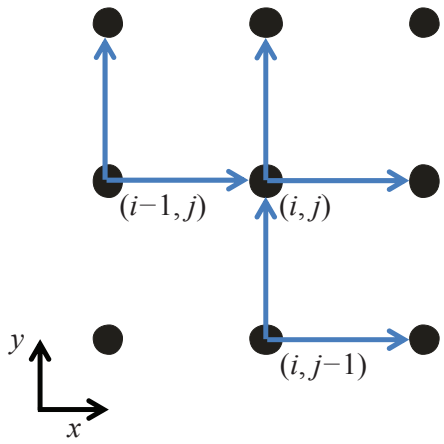

Figure 5.2: Polarization switching in a lattice point (i, j) affects f_g in $(i-1, j)$ and $(i, j-1)$ as well as (i, j) when local gradients toward only the $+x$ and $+y$ directions are considered.

This recognizes that the gradient terms are of similar magnitude but allows their contribution to be scaled relative to other energy terms using parameter J. Equation (5.14) is used in the simulation of domain evolution in section 5.6 and 5.7. When computing, local gradients toward only $+x$ and $+y$ directions were considered, see figure 5.2. Therefore, flipping a polarization direction at a lattice point (i, j) would affect f_g for lattice points $(i-1, j)$ and $(i, j-1)$ as well as the central lattice point (i, j). Thus, when computing changes in f_g, the sum of f_g changes for these three lattice points is taken.

5.3.5 Influence of applied electric field

The potential energy due to polarization in an externally applied electric field is represented as [145]

$$f_E = -\alpha(\mathbf{P}_i \cdot \mathbf{E}_i), \tag{5.16}$$

where α is a scaling factor related to the material volume represented by the lattice point, $\mathbf{P}_i$ is the polarization vector at lattice site *i*, and $\mathbf{E}_i$ is applied electric field. Note that α can be used to balance the contribution of f_{E} with respect to the total energy. In general, $D_i = P_i + \kappa_{ij} E_j$, where D_i is the electric displacement field, P_i is the induced polarization by an electric field E_j , and κ_{ij} is the vacuum permittivity. To a first approximation, E_i in equation (5.16) can be treated as $E_i = E_i^{\mathrm{ave}} + E_i^{\mathrm{vary}}$. In the experiments, E_i^{ave} was imposed. Because polarization changes so as to minimize energy, the fluctuations E_i^{vary} are expected to be smaller in magnitude than E_i^{ave}, so to a first approximation E_i^{vary} can be neglected in small regions of microstructure. Although this is a crude approximation, the results will show that even with $E_i^{\mathrm{vary}} = 0$ the model can reproduce some realistic behaviour of domains. A consequence of assuming uniform E_j but allowing P_i to vary from point to point is that the simulations do not necessarily satisfy electrical equilibrium (or Gauss's law) $D_{i,i} = q$, where q is the free charge density. Incompatible polarization arrangements, such as polarization vectors meeting 'head to head' would generate strong electric fields in practice. The present model neglects this effect and instead only enforces polarization compatibility through the gradient and dipole-dipole terms. This point is revisited in the discussion section 5.7.4.

5.3.6 Influence of applied stress

The potential energy of strain due to an externally applied stress is represented as

$$f_{\mathrm{S}} = -\beta(\boldsymbol{\varepsilon}_i \cdot \boldsymbol{\sigma}_i), \tag{5.17}$$

where β is a scaling factor, $\boldsymbol{\varepsilon}_i$ is the strain tensor associated with lattice point i, and $\boldsymbol{\sigma}_i$ is applied stress tensor. In the present work, only normal stress components were applied, in two dimensions, giving $f_{\mathrm{S}} = -\beta(\varepsilon_{11}\sigma_{11} + \varepsilon_{22}\sigma_{22})$ which tends to favour strain 'aligned' with the applied stress. Once again, the model neglects mechanical equilibrium, $\sigma_{ij,j} + b_i = 0$ where b_i is the body force per unit volume. Effectively it is assumed that the stress can be broken into an average and varying part $\sigma = \sigma^{\mathrm{ave}} + \sigma^{\mathrm{vary}}$ and that the formation of compatible domains will tend to make σ^{vary} negligible in small regions of microstructure. Again, this will be revisted in the discussion section 5.7.4.

5.4 Procedure of simulations

The flow chart of the simulation procedure is introduced in figure 5.3. The procedure of the simulation may be stated as follows. First of all, two distinct $m \times m$ arrays $\boldsymbol{P}$ and $\boldsymbol{u}$ representing polarization vectors and displacement vectors, respectively, are generated. These two arrays consist of only four values 0, $\pi/2$, π, and $3\pi/2$. The relaxation speed of local strain is assumed much faster than that of local polarization, so nine times more chances are given to flipping a displacement vector than flipping a polarization vector [146]. Thus, the simulation starts with comparing ΔF_{tot} before and after flipping a displacement vector in a randomly selected lattice point to a random direction among 0, $\pi/2$, π, and $3\pi/2$ except for the current direction. The probability of accepting the new $\boldsymbol{u}$ is determined depending on whether $\Delta F_{\mathrm{tot}} < 0$ or not. If $\Delta F_{\mathrm{tot}} < 0$, the probability of accepting the new $\boldsymbol{u}$ is 1. However, if $\Delta F_{\mathrm{tot}} > 0$, the probability is $\exp(-\Delta F_{\mathrm{tot}} / k_{\mathrm{B}}T)$. Flipping a displacement vector in a random lattice point is carried out nine times and then flipping a polarization vector is carried out. The simulation procedure for flipping $\boldsymbol{P}$ is the

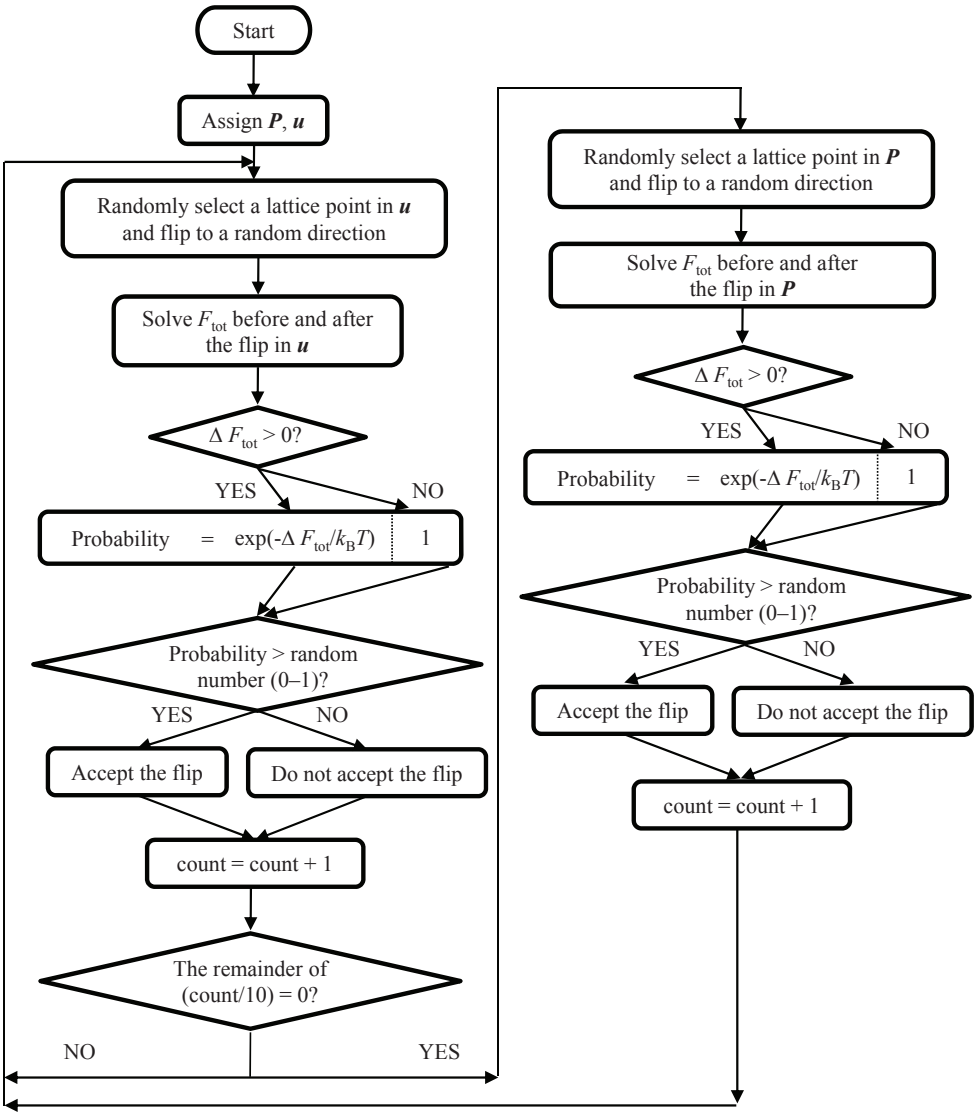

Figure 5.3: The flow chart of the iteration process based on Metropolis algorithm.

same with that for flipping ***u***. Each trial event of a displacement vector or a polarization vector flip adds 1 to the event count. One Monte Carlo step (MCS) indicates a count of m^2 trials. Finally, all the simulations in this chapter were conducted for a 2D lattice with the periodic boundary conditions such that the left and right edges are effectively joined, and the same for the upper and lower edges of the simulation region.

5.5 Effect of energy terms on domain configuration

In this section, the effect of dipole-dipole interaction energy (f_{dip}), local gradient energy (f_{g}), and the potential energy by an externally applied electric field (f_{E}) on domain configuration are studied. f_{dip} , f_{g} and f_{E} are the main energy terms that directly influence on the patterns of electrical polarization. Elastic strain energy (f_{e}) and the potential energy of an externally applied stress (f_{S}) affect the domain pattern through electrostrictive energy (f_{es}). The energy terms f_{dip} , f_{g} , and f_{E} were sequentially introduced into the model and scaling terms were calibrated to give representative ferroelectric behaviour. Firstly, only f_{dip} was incorporated into the total energy. A series of the scaling factor values, *K*, were tested to find which produced minimum energy configuration for f_{dip} . Next, only f_{dip} and f_{g} were incorporated into the total energy and the influence of the scaling factor *J* on domain configuration was studied. Then, the electrical potential energy f_{E} was added and hysteresis loops were produced from two distinct *J* values.

5.5.1 Simulation method

Initial simulations were conducted on a 20×20 square array of points. The simulation temperature, $k_{\text{B}}T$, was determined based on the previous work [145] that shows a "lock-up" phenomenon occurs when the temperature is too low. For this reason, the equivalent temperature was set to $k_{\text{B}}T = 1.5$ in all the simulations in this section. Initial polarization directions in the array were randomly assigned, and the Metropolis algorithm was applied to allow the simulation to evolve through MCS. Note that since f_{e} , f_{S} and f_{es} were not

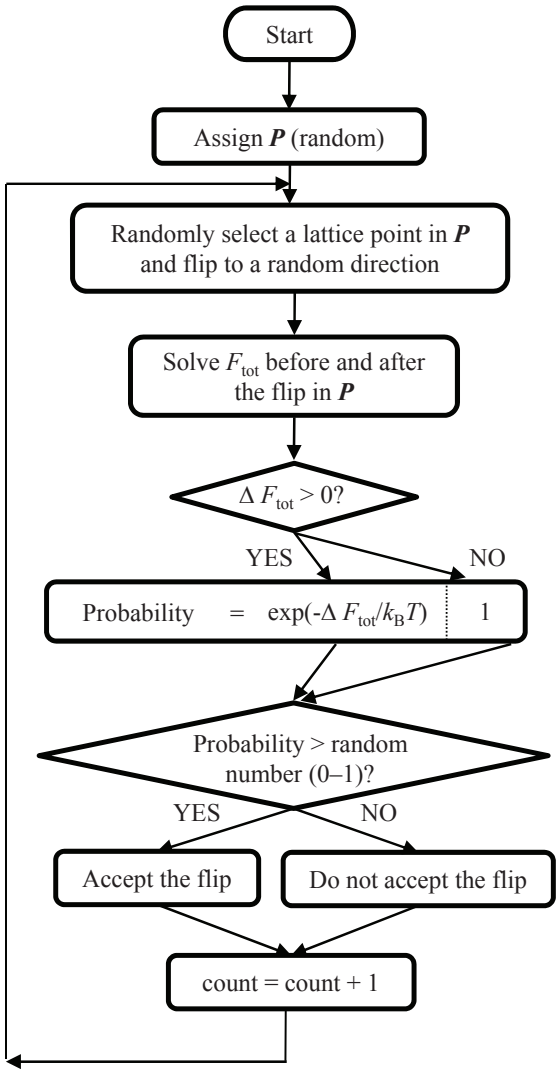

Figure 5.4: The flow chart of the iteration process that is modified from figure 5.3 for the studies in section 5.5.

incorporated into the total energy, the modified algorithm from figure 5.3 was used in this section, see figure 5.4.

5.5.2 Effect of the scaling factors on domain configurations

First of all, the effect of the scaling factor K in equation (5.10) on the total dipole-dipole potential energy and domain configuration was studied in a model with dipole-dipole interaction energy only. Figure 5.5 shows the total dipole-dipole potential energy versus MCS, and the final domain configurations at 500 MCS for $K = 1.0$, 2.0, 3.0, and 4.0. When $K = 1$, the total dipole-dipole potential energy significantly fluctuates as MCS increases, with no clear tendency of increase or decrease. Also, no clear domain configuration forms. When $K = 2$, alternating $+y$ and $-y$ polarizations and $+x$ and $-x$ polarizations can be seen in most areas. This is the typical head-to-tail arrangement of polarization, providing the minimum dipole-dipole interaction energy. And the total dipole-dipole potential energy decreased with reduced fluctuation. As K increases to 3 and 4, the graphs show less fluctuation than that when $K = 2$.

Figure 5.6 shows the average of the total dipole-dipole potential energy during the period defined by 400 MCS – 500 MCS with K in the range 0.5 – 4.0. In each case, the potential energy was averaged over two distinct simulations. The potential energy decreases as K value increases from 0.5 to 2.0. However, the potential energy does not decrease any further after 2.0. A rather small increase can be seen when $K = 2.5 – 4.0$. Therefore, $K = 2.0$ can be set as the optimized scaling factor for dipole-dipole interaction energy. Note that K may need to be adjusted when all the energies are incorporated into the total energy so as to produce realistic domain patterns. For the moment a good working value of K has been established.

As can be seen from figure 5.5, dipole-dipole interaction energy does not favour groups of neighbouring lattice points having the same polarization direction. Thus, the local gradient energy is required to allow extended domains to form in two dimensions. Taking only local gradient energy into account, the total energy was calculated during

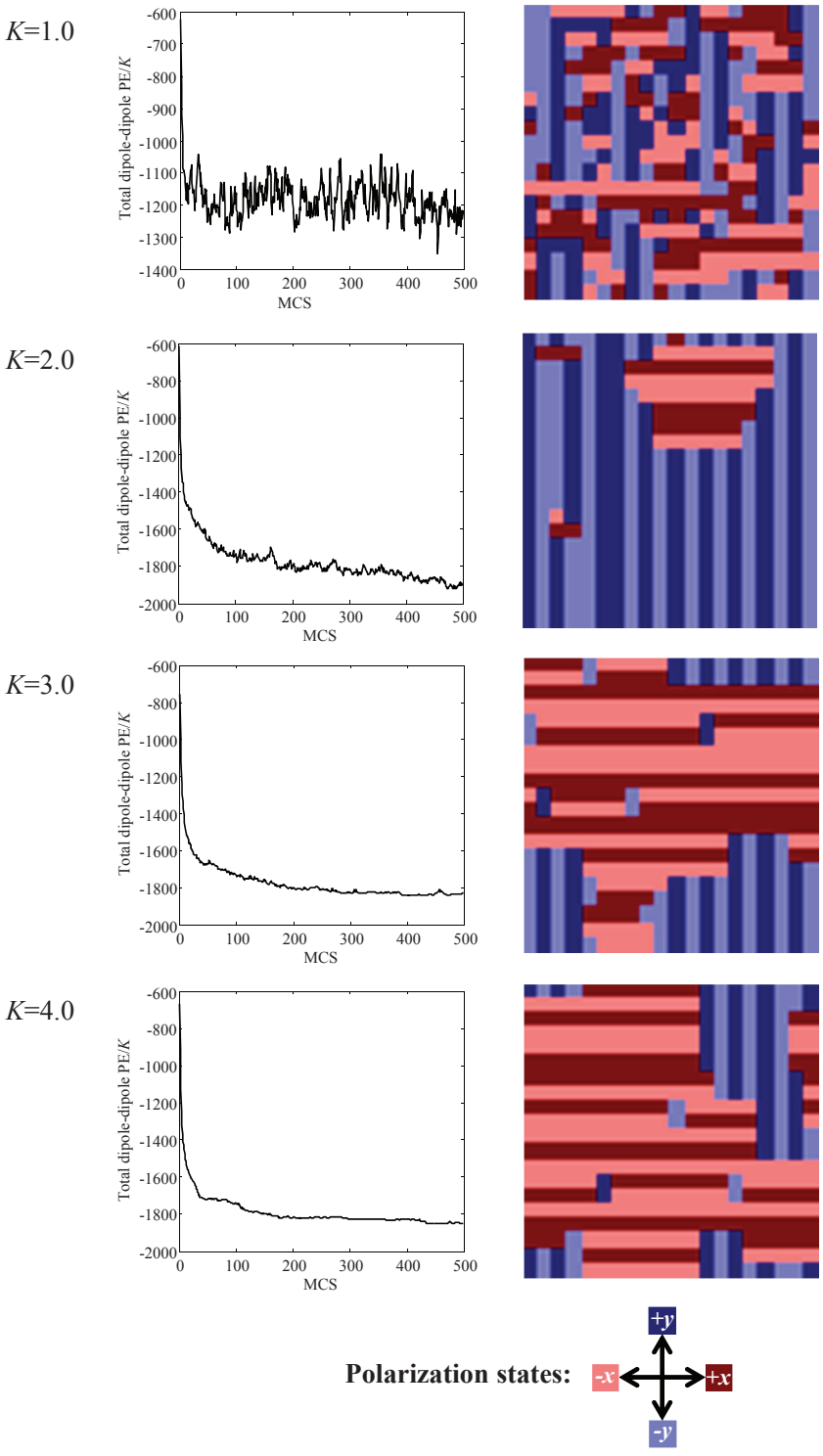

Figure 5.5: The effect of the scaling factor K on the total dipole-dipole potential energy and domain configuration. Four graphs of total dipole-dipole potential energy/K versus MCS for K = 1.0, 2.0, 3.0, and 4.0 are shown on the left while domain configurations at 500 MCS are shown on the right.

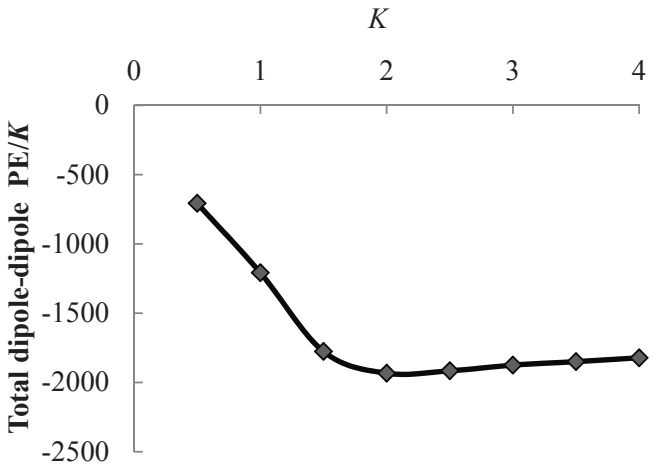

Figure 5.6: The relationship between the scaling factor K and the total dipole-dipole potential energy/K during 400 – 500 MCS. The minimum dipole-dipole potential energy/K occurred when K = 2.0.

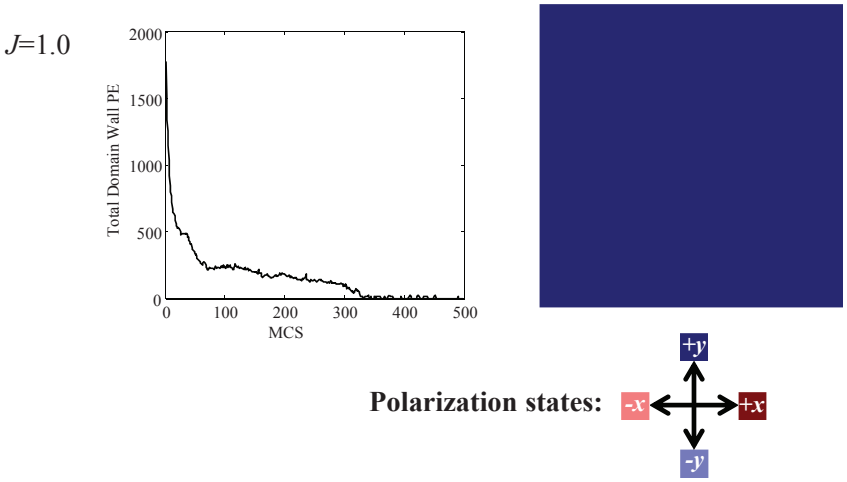

Figure 5.7: The effect of local gradient energy on domain configuration. The graph on the left represents total domain wall potential energy versus MCS while the image on the right shows the domain configuration when MCS = 500.

500 MCS. As figure 5.7 shows, the total domain wall energy reaches 0 after about 300 MCS. The domain configuration corresponding to this state is a single domain where all the polarizations are aligned to one direction. Thus, it can be confirmed that local gradient energy, acting alone, forces the local polarizations to be aligned in the same direction, as expected.

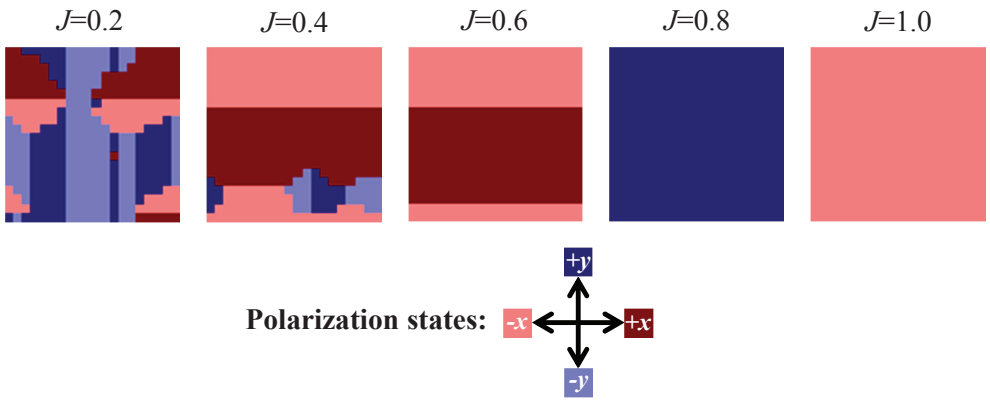

Figure 5.8: The effect of the parameter J on domain patterns when only dipole-dipole interaction energy and local gradient energy were considered.

Next, simulation was carried out to study how dipole-dipole interaction energy and local gradient energy simultaneously affect a domain configuration. In the total energy only dipole-dipole interaction energy and local gradient energy were included. While using $K = 2.0$, the scaling factor J was varied in the range 0.2 to 1.0. Figure 5.8 shows the five domain configurations at 500 MCS when $J = 0.2$, 0.4, 0.6, 0.8, and 1.0. First of all, a noticeable difference in domain configuration can be seen when $J = 0.2$ and $J = 1.0$. When $J = 0.2$, 180° and 90° domain walls form, producing domains in many regions. As J increases, more agglomerated domains can be observed, and the number of domain walls is reduced. When $J = 0.8$, and 1.0, the whole area became a single domain. Evidently when J is large, the local gradient energy dominates the total free energy.

Multiple simulation runs were used to check the results, and the results in figure 5.8 were found to be typical. This suggests that a J value in the region 0.2 – 0.4 may be realistic, however, it is also necessary to calibrate the model behaviour such that applied electric fields produce realistic effects. Hence, the electric potential energy was next introduced into the model.

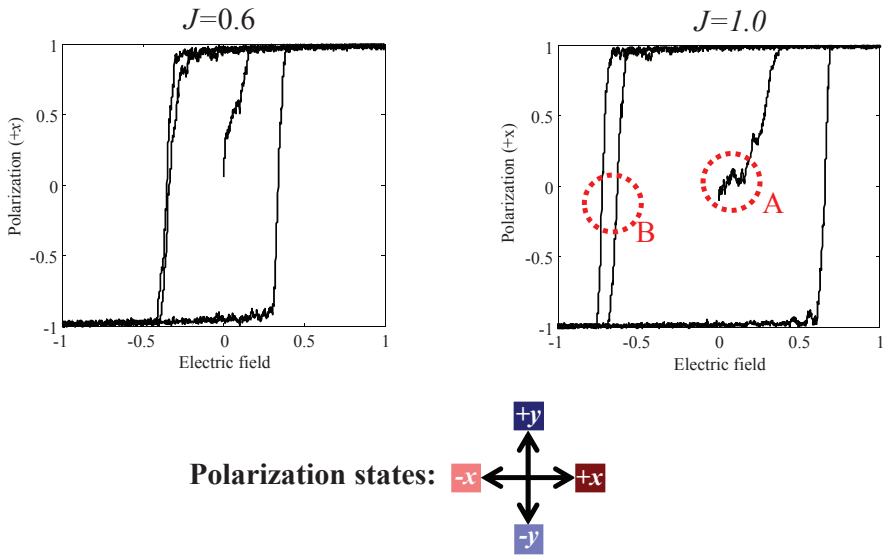

Figure 5.9: The effect of local gradient energy on the hysteresis loop. Two graphs of polarization versus electric field were generated applying $J = 0.6$ and 1.0. 'A' and 'B' in the graph indicate a fluctuating increase of polarization by applied electric field, and dissimilar coercive fields, respectively, both of which are not typically observed from real ferroelectric materials.

A cyclic electric field was applied to a 20×20 array with randomly oriented polarizations. In F_{tot}, only three energy terms f_{dip}, f_g, and f_E were incorporated to test whether this current model can generate a hysteresis loop. In this simulation, $K = 2.0$, and $\alpha = 6.0$. Note that α was decided from a number of tests to generate a hysteresis loop. The simulation was carried out for $J = 0.6$ and $J = 1.0$ to study the effect of domain wall energy on a hysteresis loop. An electric field (efield) was applied according to the following equation; $\text{efield} = \sin(2\pi \times \text{MCS}/(\ln/2))$ where ln is the total counts of trails. Electrical loading was continued for two cycles, and began with $+x$ direction.

Figure 5.9 shows two graphs of hysteresis loops of polarization versus electric field, simulated with two different values of J. Both show hysteresis behaviour of the net polarization due to applied electric field. These graphs also show a coercive field and remnant polarization that are the main features of ferroelectrics. However, unusual

features can be also found from these graphs. For example, curve 'A' can be observed in figure 5.9 where polarization briefly reduces with increasing electric field. This is not typically observed in ferroelectrics. Also, different coercive fields can be seen at 'B'. Normally the coercive field has a single, stable value. These problems may occur partly because the size of the simulation was not large enough to produce a smooth initial curve and a constant coercive field. When the size of the lattice is only 20×20, the net polarization can be significantly affected by the random perturbation of a few lattice points. Another interesting point from figure 5.9 is that the coercive field is significantly affected by the scaling factor *J*. It is well known that coercive field is affected by domain configuration [27]. For polarization switching, the electric field energy must overcome the local gradient energy allowing new domains to form. Thus, as the gradient energy increases, the coercive field also increases.

From the simulations in this section, the effect of energy terms on domain configurations was studied, and scaling factors for the dipole-dipole, gradient and electric potential energies were found. Note that the scaling factors used in this section may need adjustment when all the energies are incorporated into the total energy. The parameters and the scaling factors used will be introduced in section 5.6.

5.6 Domain pattern formed without loading

5.6.1 Simulation method

In this section, f_{dip}, f_{g}, f_{e}, and f_{es} were included in the total energy to study how a polarization array $\boldsymbol{P}$ and a displacement array $\boldsymbol{u}$ generate domain patterns through electrostrictive energy. Thus, the algorithm introduced in figure 5.3 was used. Randomly assigned polarizations and strain states were given in every lattice point as the initial

states, so a high temperature at the early MCS is required to provide enough thermal energy to flip polarizations to approach a low-energy domain configuration. Therefore, $k_{\mathrm{B}}T$ was gradually decreased in each MCS from 1.0 to 0.01. The parameters used in the previous work of Xue *et al*. [146] were applied in equations (5.5), (5.9), (5.10) and (5.14). See table 5.1 for these parameters. The actual quantity of elastic coefficient C_{11}^{*} in $\mathrm{BaTiO_3}$ is about $275\times10^{9}\ \mathrm{N\cdot m^{-2}}$ [92]. However, in the existing literatures [28,92], effective coefficients are often used to represent dimensionless variables. The effective coefficient C_{11} is calculated via $C_{11}=C_{11}^{*}\Big/\left[\left|\alpha_1^{*}\right|\left(P_0^{*}\right)^2\right]$, where α_1^{*} is a coefficient in the Landau free energy with the units $\mathrm{C^{-2}\cdot m^2\cdot N}$ and P_0^{*} is the magnitude of the spontaneous polarization at room temperature with the unit $\mathrm{C\cdot m^{-2}}$. See the reference [92] for further details. The parameters in table 5.1 represent the effective coefficients. Simulation was then carried out using a 70 × 70 lattice size.

Table 5.1: Normalized values of parameters used in the simulation [146].

G_{11}	G'_{12}	G'_{44}	G''_{44}	C_{11}	C_{12}	C_{44}	q_{11}	q_{12}	q_{44}
1.60	0.00	0.80	0.80	2.75	1.79	0.54	0.142	-0.0074	0.0157
K	γ								
1.0	7.15								

5.6.2 Results and discussion

Figure 5.10 shows a pair of 70 × 70 arrays representing the polarization array ***P*** and strain state ***S*** that is derived from a displacement array ***u***. These images show a typical final result after 10000 MCS starting from a random state. A noticeable result is that the lattice points with the strain state h in ***S*** exactly matches to the lattice points with polarization

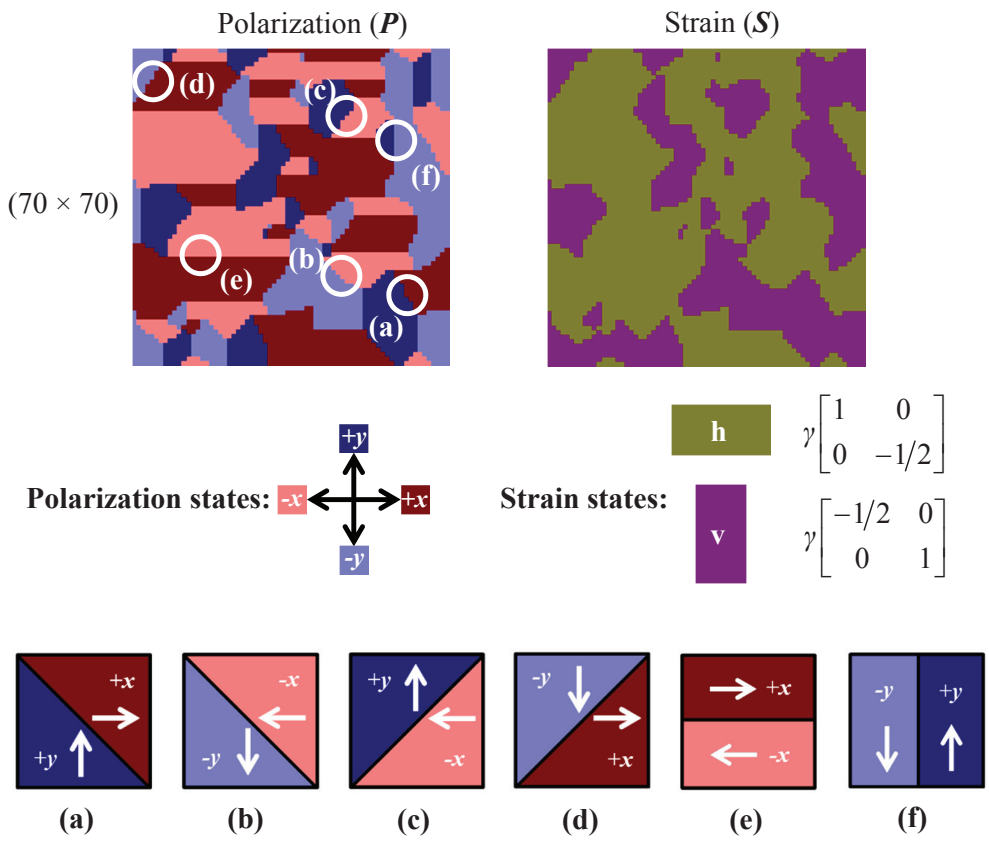

Figure 5.10: Domain patterns generated in a 70 × 70 lattice through Monte Carlo simulation from randomly oriented polarization directions and strain states. (a)–(f) show electrically compatible domain structures found from the polarization array ***P***.

vectors ±*x* in ***P***, and the lattice points with the strain state v in ***S*** matches to the lattice points with polarization vectors ±*y* in ***P***. This demonstrates that polarization and strain are strongly coupled *via* electrostrictive energy. The domain structure in ***P*** in figure 5.10 consists of four types of 90° domain wall (a)–(d) and two types of 180° domain wall (e)–(f). These configurations are generated because dipole-dipole interaction energy favours head-to-tail configuration while gradient energy favours the formation of domains. And this domain configuration is typical of the patterns of ferroelectric domain that are experimentally observed.

5.7 Domain evolution processes

For compatible and partly compatible domain patterns, domain evolution is studied in this section. Before applying electric field and mechanical stress, simulations were carried out to test how compatible and incompatible domain patterns behave without loading. Then, electric field and mechanical stress were applied to the compatible and partly compatible domain patterns.

5.7.1 Compatible and incompatible domain patterns

First of all, three distinct 50×50 $\boldsymbol{P}$ arrays (see figures 5.11(a)–(c)) were generated by assigning polarization vectors in each lattice point. The initial domain pattern in figures 5.11(a),(d) is a compatible arrangement of 90° domain lamellae, similar to the lamellae that were experimentally observed in PZT, see chapter 2, figure 2.17. The domain pattern in figures 5.11(b),(e) is compatible except for the part marked by a circle where the domain wall orientation generates tail-to-tail arrangement of polarizations. This is representative of blunt needle-like domains such as the [001] aligned domain seen in figure 2.15, chapter 2. And finally, figures 5.11(c),(f) are incompatible domain patterns with head to head polarization. The initial $\boldsymbol{u}$ arrays were set to be identical with the initial $\boldsymbol{P}$ arrays so that computation is not wasted coupling $\boldsymbol{P}$ with $\boldsymbol{u}$. In this section, all the energy terms except for f_{E} and f_{S} were included in F_{tot}. Simulations were carried out for 10000 MCS for two distinct temperature states: $k_{\mathrm{B}}T = 0.01$ and $k_{\mathrm{B}}T = 1.0 \rightarrow 0.01$.

Figures 5.11(a)–(c) show the initial states and states after 10000 MCS of three distinct domain patterns under no loading when $k_{\mathrm{B}}T = 0.01$. Comparing the initial states to the final states, almost no change can be observed from the incompatible domain

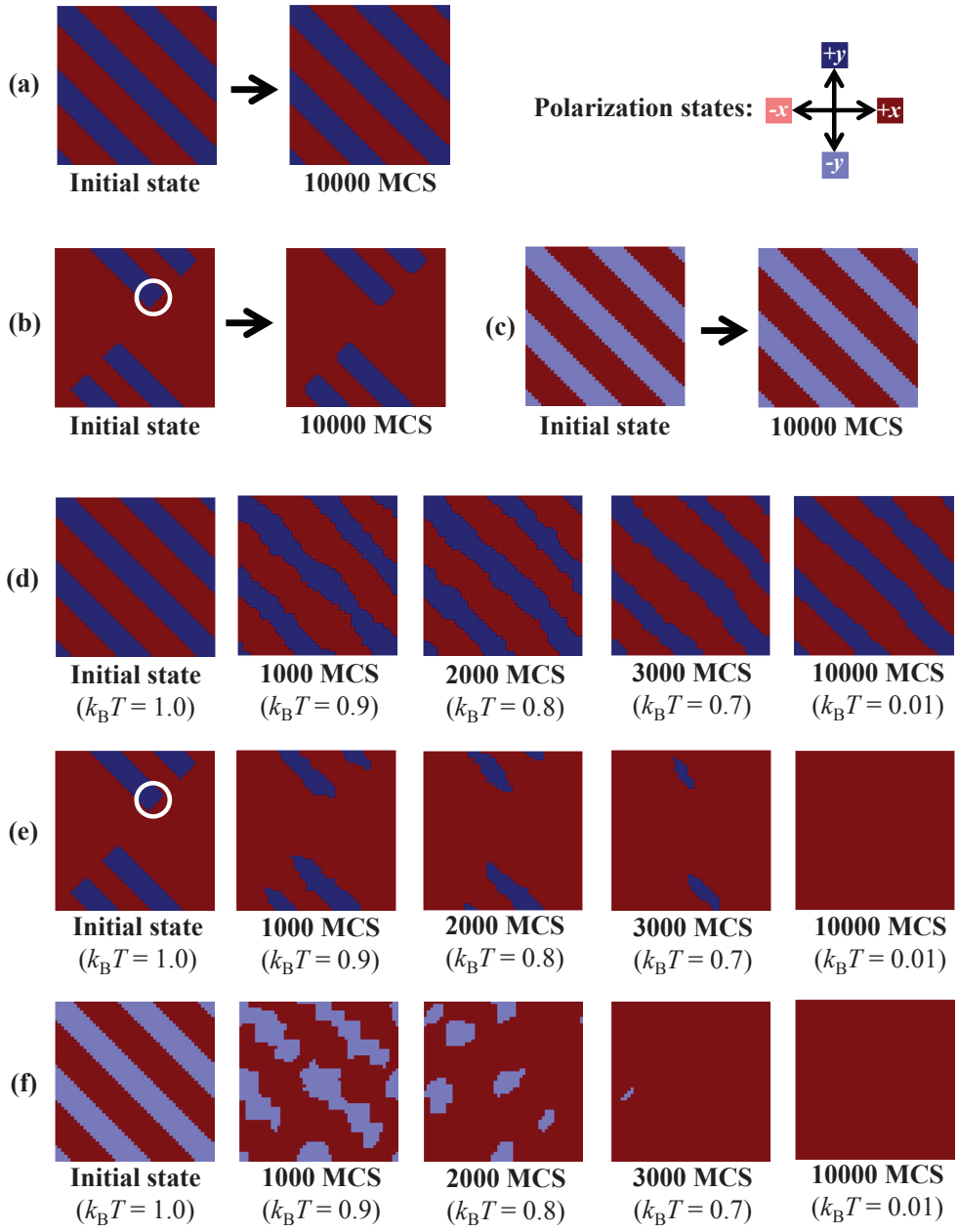

Figure 5.11: The effect of temperature on domain patterns. (a)–(c) Almost no evolution has occurred when $k_BT = 0.01$. (d)–(f) Domain evolutions have occurred when k_BT gradually decreased from 1.0 to 0.01 during 10000 MCS. The domain structures at initial state in (a),(d) are compatible patterns while those in (c),(f) are incompatible patterns. The domain structures in (b),(e) are partially compatible due to the incompatible domain walls marked by circles.

pattern in figure 5.11(c) as well as the compatible domain patterns in figures 5.11(a)–(b). Next, the simulations were carried out while gradually decreasing the temperature. Initially $k_{\mathrm{B}}T = 1.0$, and $k_{\mathrm{B}}T$ reached 0.01 after 10000 MCS. The results are shown in figures 5.11(d)–(f). In the compatible domain pattern figure 5.11(d), curvy domain walls can be seen when MCS = 1000. The level of fluctuation in domain wall gradually decreased as the temperature decreases. When MCS = 10000, the fluctuation in domain walls was significantly reduced. Meanwhile, in figure 5.11(e), the $+y$ domain gradually disappeared, and the domain pattern evolved into a mono-domain at the final MCS. In this domain pattern, most domain walls are electrically uncharged except for the part marked by circle. Since this small region is not favourable by dipole-dipole interaction energy, the edge turned into a sharp structure during evolution process. In figure 5.11(f), the incompatible domain pattern also dissolved into a mono-domain state. The only difference between figure 5.11(c) and figure 5.11(f) was $k_{\mathrm{B}}T$ values and hence it can be concluded that an incompatible domain pattern cannot persist with high f_{dip} at a high temperature. From figure 5.11, the effect of temperature on compatible and incompatible domain patterns can be observed.

5.7.2 Domain evolution under electrical loading

For the compatible and partly compatible domain patterns in figures 5.11(a)–(b), domain evolution under electrical loading was studied. Simulation was conducted at $k_{\mathrm{B}}T = 0.01$ for 2000 MCS. An electric field $E = 1.0$ was applied to three distinct directions $+x$, $+y$ and $-y$. The scaling factor $\alpha = 3.21$ in equation (5.16) was applied to capture a gradual domain wall motion. Firstly, for the domain pattern that was most stable under no loading, the evolution process by an electric field is shown in figure 5.12. The images in

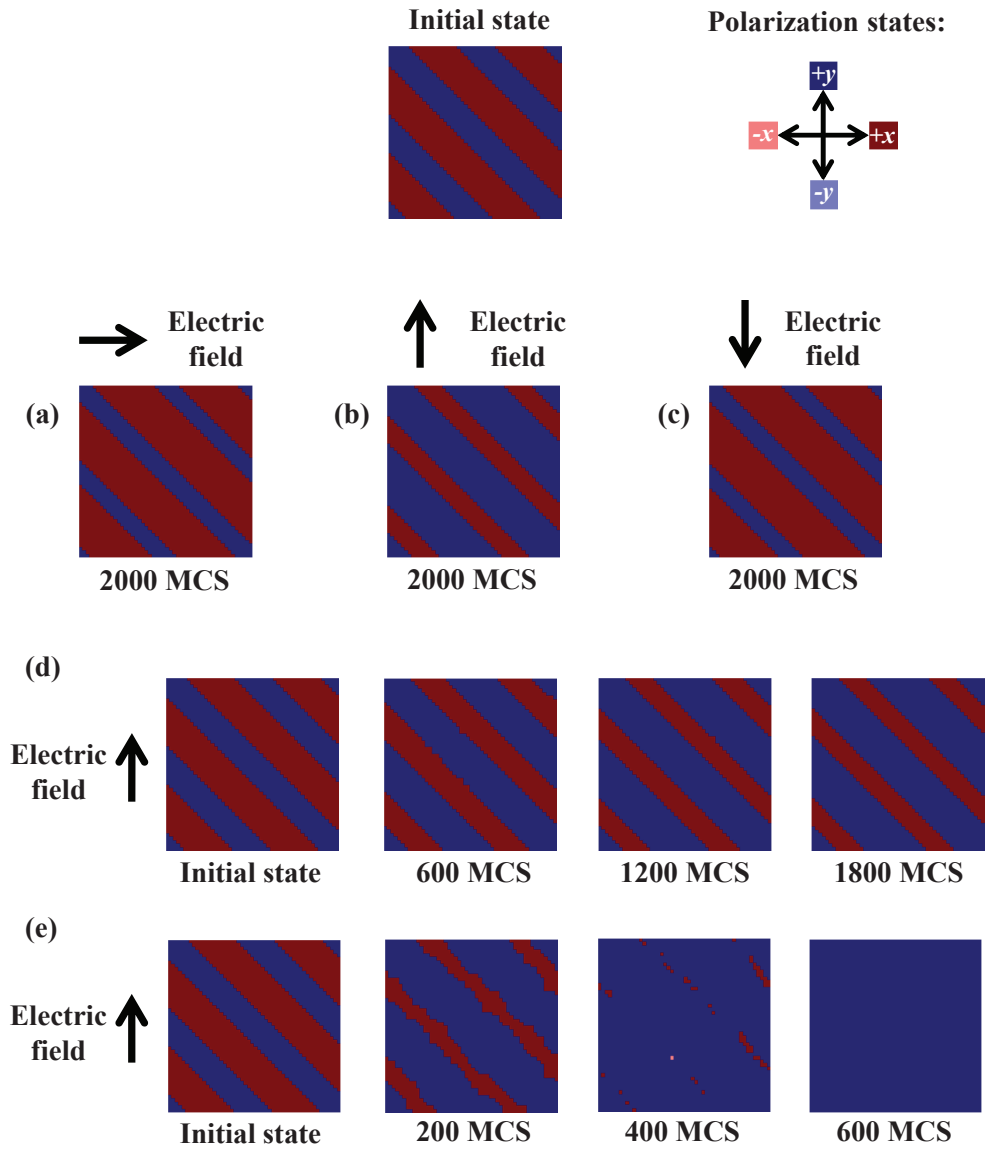

Figure 5.12: Domain evolution processes of the compatible domain pattern by three distinct electric field directions. (a)–(c) Domain structures evolved for 2000 MCS by applied electric fields in $+x$, $+y$, and $-y$ directions, respectively, with the scaling factor $\alpha = 3.21$. (d) The domain evolution process after 600 MCS intervals when the scaling factor $\alpha = 3.21$. (e) The domain evolution process after 200 MCS intervals when the scaling factor $\alpha = 3.6$.

figures 5.12(a) and (b) show the resulting domain structures after 2000 MCS when an electric field was applied to $+x$ and $+y$ directions, respectively. The domains aligned with the applied electric field direction broaden gradually while maintaining flat domain walls. In figure 5.12(c), an electric field was applied to $-y$ direction, and the $+x$ domain that is

more closely aligned with $-y$ than the $+y$ domain has grown. Figure 5.12(d) shows the domain evolution process after 600 MCS intervals when an electric field was applied to $+y$ direction. Since 1200 MCS, no significant evolution process can be seen from the lamellar pattern. This reason was attributed to a weak electric field strength, so the same simulation was conducted with $\alpha = 3.6$, see figure 5.12(e). This domain evolution process shows that $+x$ domain has disappeared at 600 MCS. Also, at high field strength the domain walls do not remain flat.

Two interesting points can be seen from figure 5.12. First of all, polarization switching took place *via* a domain broadening process. To nucleate a domain in the interior of another domain, a high energy is required to overcome the local gradient energy. Therefore, polarization switching *via* domain wall motion is energetically more favourable than domain nucleation. This broadening process in the lamellar pattern is in agreement with the observed evolution process through PFM images, see chapter 2, figure 2.17. Secondly, polarization switching was significantly constrained by the pre-existing domain pattern. When electric field was applied to $-y$ direction, polarization switching was carried out by evolving the pre-existing domain wall between $+x$ and $+y$ domains instead of nucleating $-y$ domains.

Figure 5.13 shows the domain evolution processes of the partly compatible needle-like domain pattern by an electric field for 2000 MCS. Figures 5.13(a)–(c) show the final state after 2000 MCS, and the gradual evolution processes can be seen from figures 5.13(d)–(f). First of all, the simulation results show that the domain that is closely aligned with the electric field direction grows. And also, the incompatible domain walls marked by a circle in figures 5.13(d)–(f) were transformed into sharp structures regardless of electric field direction. This illustrates that domain structures evolved maintaining a low-energy domain configuration. Figures 5.13(d) and (f) show a similar

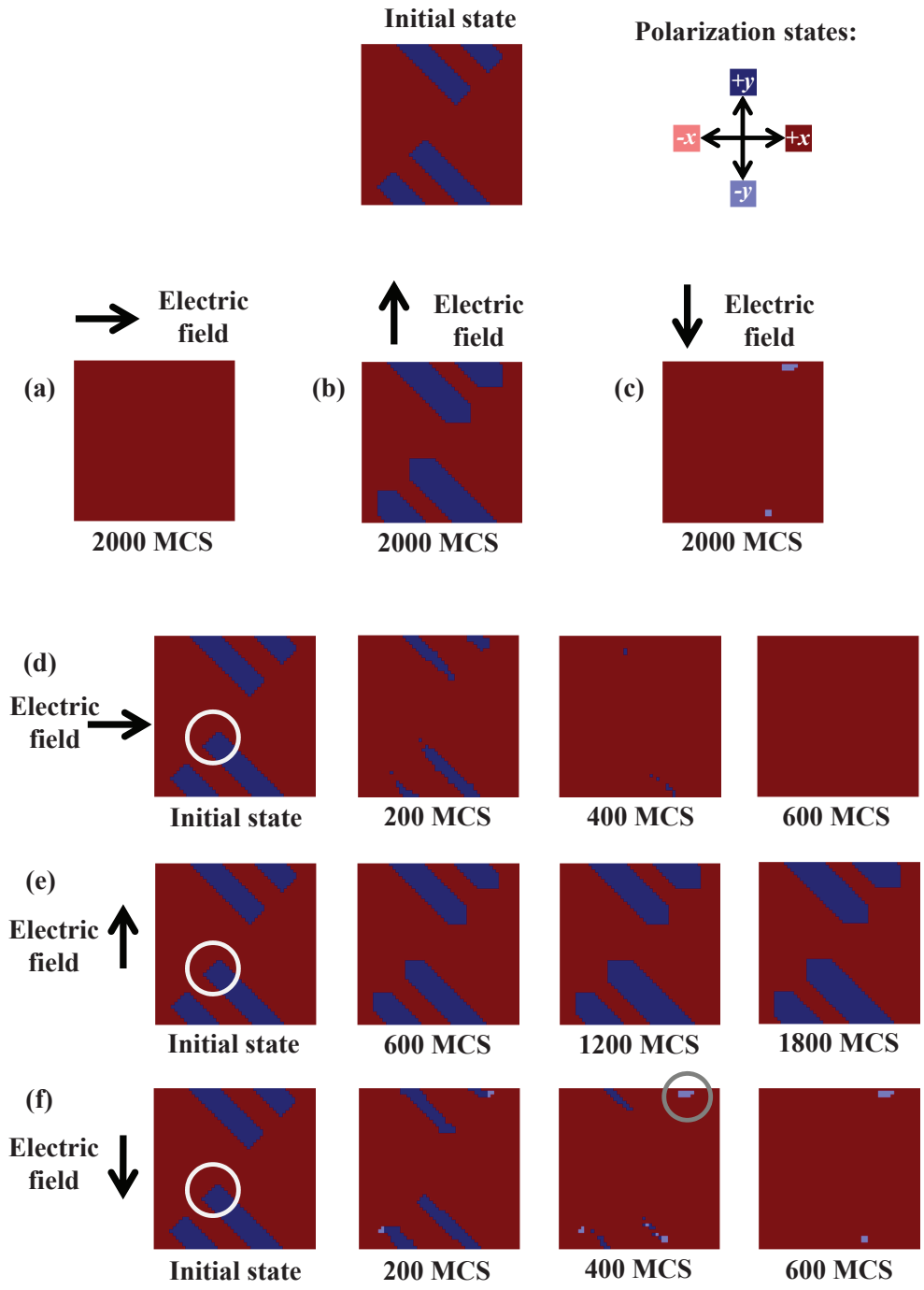

Figure 5.13: Domain evolution processes of the partly incompatible domain pattern by three distinct electric field directions. (a)–(c) Domain structures evolved for 2000 MCS by applied electric fields in $+x$, $+y$, and $-y$ directions, respectively. (d)–(f) Domain evolution processes after 200 or 600 MCS intervals are shown for applied electric fields in $+x$, $+y$, and $-y$ directions, respectively. Note that the domain walls marked by circles in the initial domain state indicate incompatible domain arrangements while the region marked by a circle at 400 MCS in (f) indicates a domain switched by 180°.

evolution process to each other in that +*y* domain gradually retreats. The main difference between these two evolution processes is that in figure 5.13(f), the evolution process involves some 180° domain switching, see the region marked by circle in the 400 MCS image. Note that the evolution process of a needle-like domain structure, observed from PFM, was that lengthening is energetically more favorable than broadening as always either lengthening happened alone, or a combination of lengthening and broadening happened. However, in this simulation no lengthening process was observed from figure 5.13(e). This difference will be discussed in section 5.7.4.

5.7.3 Domain evolution under mechanical loading

Under the same simulation conditions with section 5.7.2, f_{E} was replaced by f_{S} in F_{tot} to study domain evolution by a mechanical stress. Since only three energy terms f_{e}, f_{es}, and f_{S} include strains in their equations, flipping a displacement vector in ***u*** array will be determined by these three energy terms. In this model, f_{e} is always constant regardless of the displacement vector when only two strain states in the tetragonal phase are present. Thus, if $\Delta f_{\mathrm{S}} + \Delta f_{\mathrm{es}} < 0$ by flipping a displacement vector, this flipping is likely to be accepted. In the present simulation, the scaling factor $\beta = 10.0$ in equation (5.17) was set so that $\Delta f_{\mathrm{S}} + \Delta f_{\mathrm{es}} < 0$ can be satisfied. Thus, all the strain states were transformed into one state between h and v in figure 5.10 depending on the loading direction. And then, flipping a polarization direction followed to minimize f_{es}.

The evolution processes of the compatible domain pattern under compressive loading show that the domain orthogonal to the loading direction grows through domain wall motion, see figure 5.14. This evolution process *via* domain broadening is in

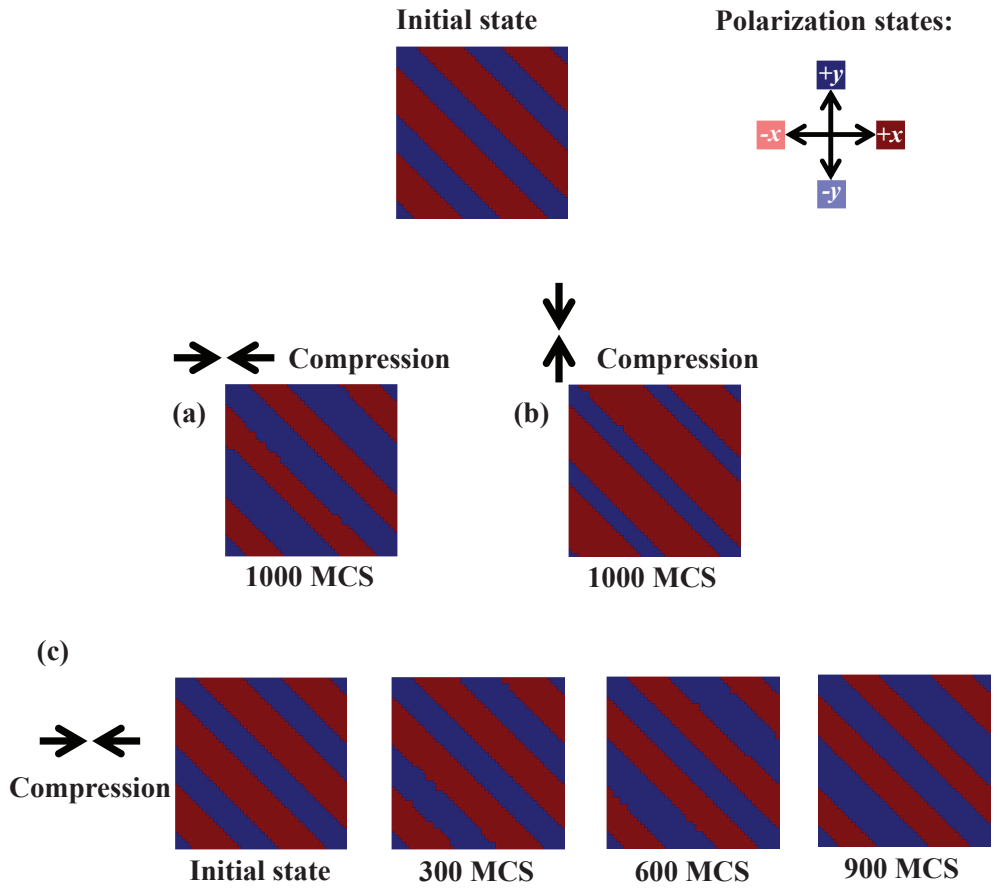

Figure 5.14: Domain evolution processes of the compatible domain pattern under compressive loading. (a)–(b) The domain structures evolved for 1000 MCS by compressive stress in $\pm x$ and $\pm y$ directions, respectively. (c) The domain evolution process after 300 MCS intervals by compressive stress in $\pm x$ direction.

agreement with the experimentally observed domain evolution process in figure 3.6, chapter 3.

Figure 5.15 shows the domain evolution processes of the partly compatible domain pattern under compressive loading. When the compressive loading direction was $\pm x$, the $+y$ domain broadened, see figure 5.15(c). And when the compressive loading direction was $\pm y$, $+y$ domain retreated as can be seen from figure 5.15(d). Regardless of the loading directions, the incompatible domain wall marked by a circle was always transformed into a sharp structure.

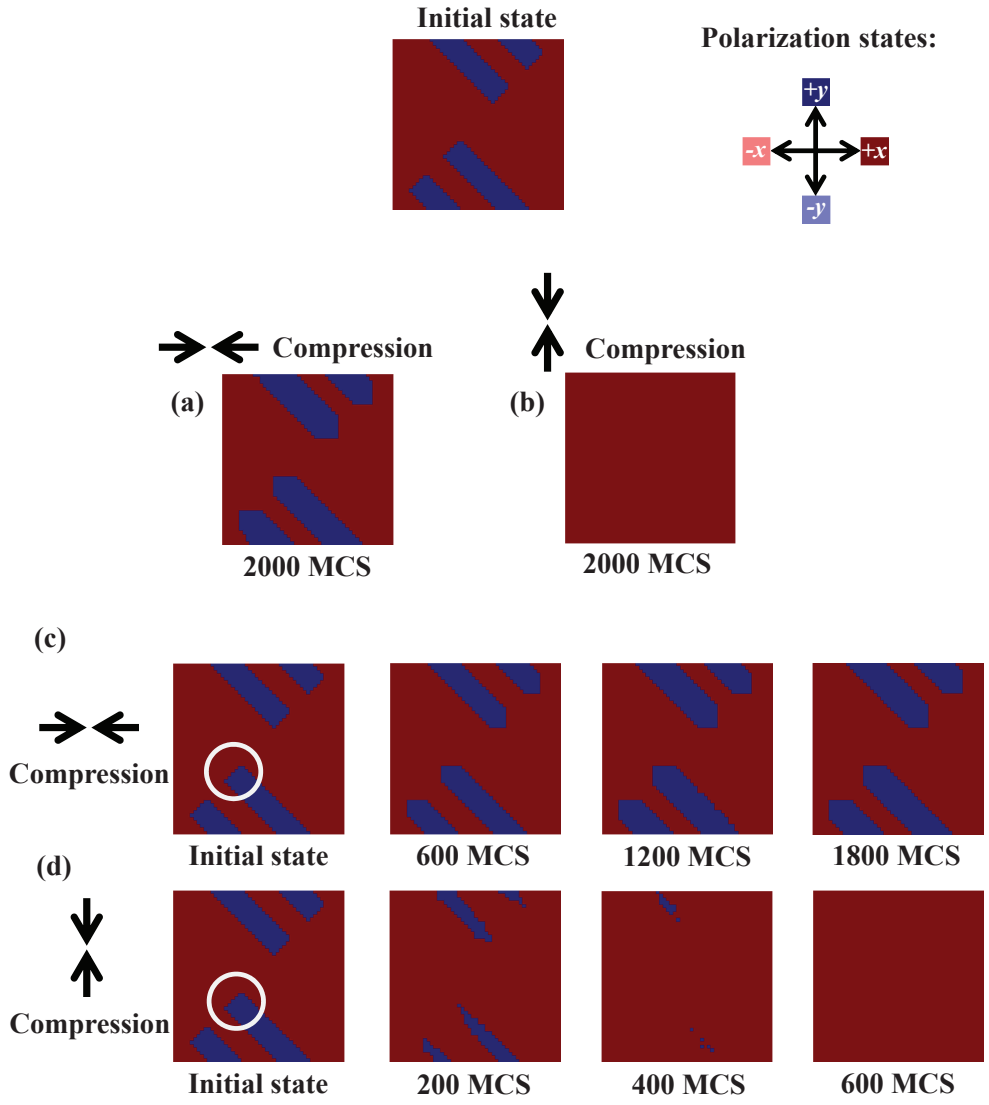

Figure 5.15: Domain evolution processes of the partly compatible domain pattern under compressive loading. (a)–(b) The domain structures evolved for 2000 MCS by compressive stress in $\pm x$ and $\pm y$ directions, respectively. (c) The domain evolution process after 600 MCS intervals by compressive stress in $\pm x$ direction. (d) The domain evolution process after 200 MCS intervals by compressive stress in $\pm y$ direction. Note that the circles in (c),(d) indicate incompatible domain walls.

5.7.4 Discussion

In section 5.7.2 and 5.7.3, domain evolution processes by electric field and mechanical stress were studied using Monte Carlo simulation. In particular, a domain broadening process, that was observed from PZT using PFM, was successfully reproduced. However, the lengthening process *via* the tip motion in the needle-like domain structures, introduced in figure 2.18, chapter 2 was not found in the simulation. Note that a similar evolution process has been also observed experimentally in $BaTiO_3$ [61]. Several possible reasons for this discrepancy could be speculated. First, the choice of model parameters may not sufficiently favour motion of the incompatible needle-tip regions. To test this, the electric field scaling factor α, temperature k_BT and lattice size m were varied.

To make a comparison with the previous simulation in figure 5.13(e), the same parameters were applied to the simulations except for one parameter. First of all, the scaling factor α was increased from 3.21 to 3.6 to study the effect of an electric field strength on a domain wall motion. As figure 5.16(a) shows, domain evolution continued to occur mainly *via* domain broadening. Thus, the electric field strength was not the cause for the discrepancy. Next, k_BT was increased from 0.01 to 0.1. As figure 5.16(b) shows, almost no lengthening was observed; instead, the $+y$ domains merged together through the domain broadening process. Finally, the lattice size m was increased from 50 to 200 to examine if the domain lengthening process was constrained by the small model size. Note that in this model, the size of the needle domain tip is determined by the minimum size of pseudo grain. A domain size cannot be smaller than the size of the pseudo grain. An initial domain pattern that is similar with the initial state in figure 5.13(e) was generated in figure 5.16(c) in a 200×200 lattice size. As figure 5.16(d) shows, domain evolution again happened *via* domain broadening. No lengthening process can be seen except for the sharpened tips.

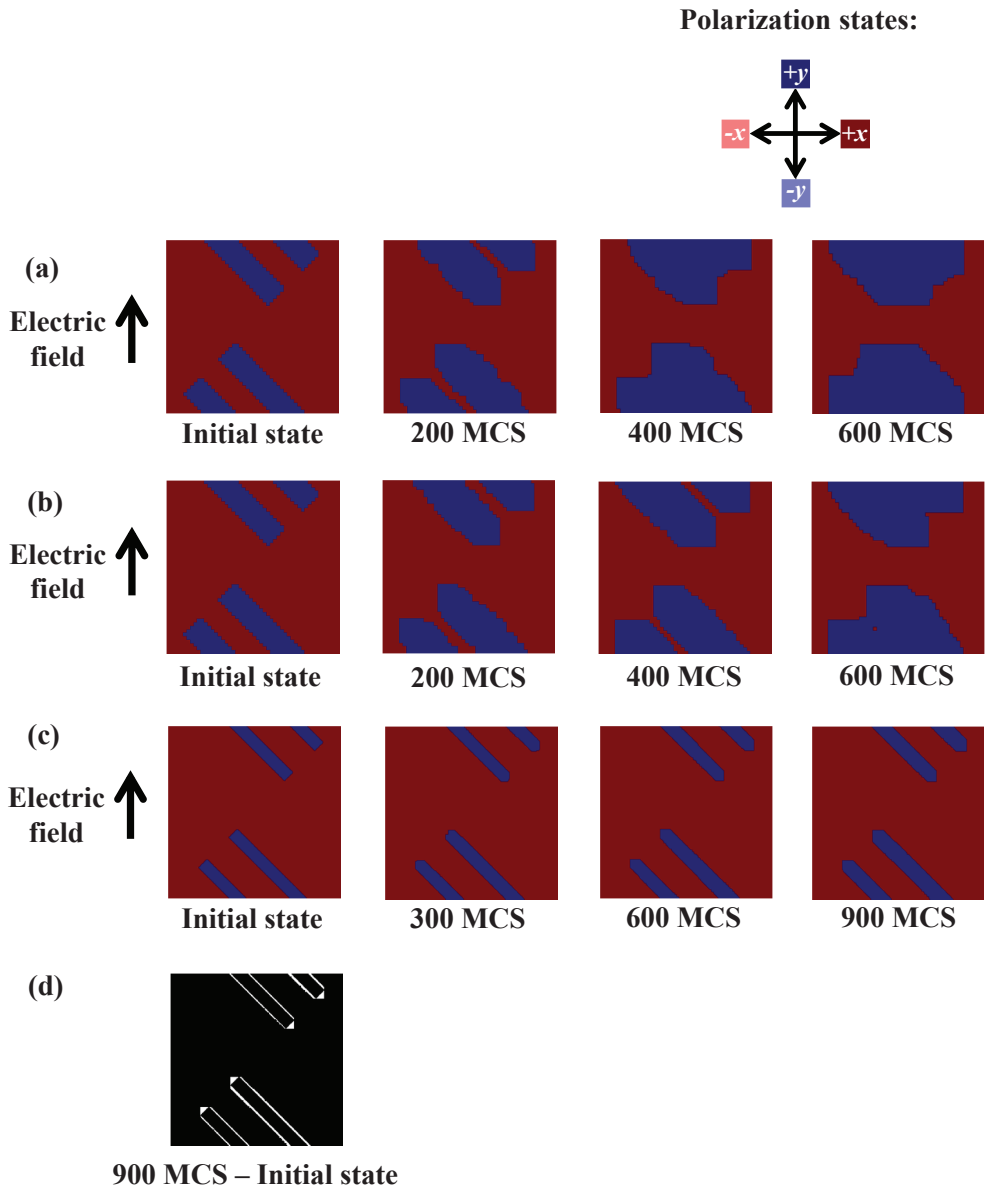

Figure 5.16: The effect of parameters on the evolution process of the blunt needle-like domain. The same parameters with figure 5.13(e) were applied to each simulation except for one parameter: (a) The scaling factor $\alpha = 3.6$, (b) $k_B T = 0.1$, (c) The lattice size $m = 200$. (d) The difference map between 900 MCS and the initial state in (c).

One difference between the needle-like domain structures observed through microscopy and the domain patterns in figure 5.16 is that the needle-tips in the simulation are blunt 90° wedge structures (see 900 MCS in figure 5.16(c)) while the observed angles of the tip in typical needle-like structures are only a few degrees. This suggests a strong

energy penalty in the real material against incompatible polarization/strain arrangements. To reproduce this in the model, we could enhance the G_{11} and G'_{12} terms in the gradient energy, equation (5.14). This would penalize divergence $P_{i,i}$ in the polarization field.

Furthermore, the assumption of uniform fields E^{ave} and σ^{ave} is likely to be most inaccurate near sharp features such as the needle-tips. This could be addressed in the model by solving the equilibrium equations $D_{i,i} = q$; $\sigma_{ij,j} + b_i = 0$ separately, and using the resulting local fields when calculating the electrical and mechanical potential energies (equations (5.16) and (5.17)).

As it stands, the model did not fully capture the way incompatible needle-tips evolve. Therefore, this model needs to be developed to fully incorporate electrical and mechanical compatibilities. Nevertheless, the current study shows that there is potential to use Monte Carlo simulation for reproducing the evolution process of ferroelectric domains.

5.8 Conclusion

In this chapter, ferroelectric domain structures were generated *via* a phenomenological approach, and domain evolution was studied using Monte Carlo methods. Two distinct arrays representing polarization vectors and displacement vectors, respectively, were created, and only four in-plane vectors were allowed in each array. The total energy consists of dipole-dipole interaction energy, local gradient energy, electrostrictive energy, and elastic strain energy. When an electric field or a mechanical stress is externally applied, additional potential energy terms were included. Compatible 90° and 180° domain patterns were generated from the initial state where polarization and strain state were randomly assigned in each lattice point. In the absence of loading, compatible

domain patterns tended to be stable regardless of temperature, but incompatible domain patterns disappeared at high temperature. By an externally applied electric field, domain evolution took place *via* domain wall motion. The domains aligned with the electric field direction grow through a domain broadening process. Regardless of electric field direction, domain evolution happened *via* the domain wall motion between the pre-existing domains rather than nucleating a new domain. Also, under compressive loading, the domains with polarization that is orthogonal to the loading direction grow through a domain broadening process.

From this chapter, it was illustrated that a simple domain evolution process can be reproduced by a Monte Carlo simulation method. However, a difference between the experimental observation and the simulation result was that domain evolution *via* a needle lengthening process was not observed from the simulations. To reproduce more realistic domain wall motions, the current model needs further development, and it is suggested that penalizing polarization divergence and relaxing the assumption of uniform fields could lead to an improved model.

Chapter 6. Conclusion and future work

6.1 Conclusions and discussions

In this thesis, domain evolution processes in ferroelectric ceramics under electrical and mechanical loading were studied using PFM. For a systematic analysis of PFM data, AR-PFM was studied and applied to identify the phase and domain structures. A selection of the observed evolution processes were reproduced using Monte Carlo simulation.

Domain evolution in near-morphotropic PZT by an electric field was studied through two experimental methods. Firstly, histograms of pixel intensity in PFM images were obtained from the surface of the PZT. Dome-shaped and M-shaped histograms were generated from unpoled and poled regions, respectively. Correlating these features in the histograms with their PFM images showed that the presence of fine non-180° domain structures is responsible for the intermediate contrast resulting in the dome shaped distributions. Meanwhile, coarser 180° domains contribute to the bi-modal M-shaped distributions. Such a difference in the histograms may be caused by domain evolution of non-180° domain patterns, but this method provided only statistical evidence for the domain evolution. Thus, for direct evidence of domain evolution, step-wise poling was carried out on the PZT, interrupted by VPFM scanning after each poling step. Domain evolution was studied for typical low-energy domain configurations such as herringbone and checkerboard. In general, domain evolution occurred according to the primary principle that switching occurs so as to allow external loads to do positive work. However, locally domain evolution sometimes took place contrary to this primary principle to maintain compatibility conditions with the neighbouring domains. Overall,

the evolution processes showed that domain switching was carried out through the evolution of the pre-existing domain pattern.

Next, ferroelastic domain evolution by a compressive stress was studied with the PZT material using VPFM. While 180° domain walls were almost motionless, non-180° domain walls evolved, supporting the hypothesis that mechanical stress induces only non-180° polarization switching. Domain evolution took place *via* broadening of lamellae and overwriting one lamellation by a differently oriented lamellar pattern. This overwriting process involved simultaneous multiple switching processes. The primary principle, requiring positive work from external loads during switching, is followed overall, but the overwriting process involved energetically unfavourable as well as favourable transformations. It was concluded that the domain switching is again significantly constrained by the pre-existing domain patterns, and multiple types of switching can take place concurrently.

In chapter 2 and 3, the studies on domain evolution in ferroelectrics relied on VPFM. Depending on crystal orientation, multiple domains may not be exposed by typical VPFM and LPFM, and hence an AR-PFM technique based on LPFM data was applied to identify domain structures. To generate an AR-PFM map, an image registration process using control point selection method was used. And then, domain structures were mapped by using the angle of phase reversal in the LPFM signal during sample rotation. AR-PFM maps represent domains based on surface displacement orientations, and hence occasionally discriminated multiple domains that appear as a single domain in VPFM. Using the data of crystallographic orientation from EBSD, the discrepancy between the direction of lateral surface displacement and the in-plane component of the polarization direction was demonstrated. In certain conditions, the phase in near-morphotropic PZT where tetragonal and rhombohedral phases can coexist was identified by AR-PFM.

To help understand the physics underlying the observed domain evolution and to reproduce the pattern evolution, a phenomenological model was developed and simulated *via* Monte Carlo method. In every lattice point, electrical polarization and strain state were coupled *via* electrostrictive energy. Typical electrically compatible domain patterns in the tetragonal phase were reproduced from randomly oriented initial polarization states. Under no loading, the stability of incompatible domain patterns was significantly affected by the temperature. Under electrical and mechanical loading, domain switching occurred *via* the motion of domain walls between the pre-existing domains and was consistent with the primary principle. The domain evolution process *via* domain broadening was reproduced through Monte Carlo simulation, which was a typical evolution process observed from PFM.

6.2 Future work

6.2.1 Characterization techniques for identifying ferroelectric domain structures

In chapter 4, the merits of AR-PFM were discussed. Also, the issue of image distortion and its solution by image registration were introduced. Residual errors in AR-PFM maps are expected to be minimized by reducing initial distortion. Therefore, a couple of methods to minimize image distortion are introduced here. First of all, the non-linearity problem could be minimized by using closed-loop AFM instead of open-loop AFM. Intrinsic non-linearity can be reduced or compensated by calibrating the instrument using standard calibration grids, but the level of non-linearity varies depending on scan speed and scan range [69]. Therefore, the possibility of image distortion always exists in the open-loop condition. Contrary to open-loop configuration, in the closed-loop AFM, the

motion of the scanning probe that deviates from the pre-determined behaviour is amended in real time. Thus, scanner non-linearity could be reduced in closed-loop configuration.

Another major problem was creep induced by spatial offset during scanning. To solve this problem, precisely locating the tip on the sample surface is required. However, it is difficult to accurately site the tip on the sample surface because the location of the tip underneath the cantilever is in general invisible through the optical system in AFM. Some advanced tips that are visible through optical microscope are already available on the market. These tips are often used in the tasks requiring precise positioning and could contribute to alleviating image distortion induced by creep.

Finally, VPFM images are more suitable for image registration than topography images. In this thesis, the instrument available did not simultaneously generate VPFM and LPFM signals. Thus, topography images were used for image registration instead of VPFM images. However, there are normally not many sharp features in the topography image (the sample was polished flat), making an accurate image registration difficult. Besides, when there are not enough topography features for image registration, generating the AR-PFM map becomes almost impossible. Therefore, for improved application of the AR-PFM technique, performing AR-PFM using a SPM instrument that simultaneously generates VPFM and LPFM signals is crucial.

If these current issues are improved, AR-PFM is expected to be one of the most powerful analytical techniques for characterizing ferroelectric domain structures. Aside from PFM, domain evolution has been studied using TEM that enables *in situ* observations [34,61,62]. The main merit of TEM is that it does not require any direct contact between the imaging tool and the sample material. Local polarization switching process through SPM tip can be directly observed using TEM, which is one of the good examples of TEM use in studying ferroelectric domains [149,150].

However, most imaging techniques are constrained to the surface of materials. In fact, domain structures and evolutions in the interior of the sample are responsible for macroscopic properties in ferroelectrics. As discussed in chapter 3, there is a difference in the constraint of switching between the interior and the surface of the crystal. Therefore, further studies on domain evolutions taking place in the volume are required to understand the relationship between the microstructure and macroscopic properties. High resolution X-ray diffraction imaging with monochromatic light would be a suitable technique for this study since it can reveal domain structures in the interior of samples [67].

6.2.2 Further studies on domain evolution under mechanical loading

When a ferroelectric material is subjected to a constant level of stress, creep in strain takes place through domain wall motion [5]. However, while conducting *in situ* PFM observation of domain evolution under compressive loading in chapter 3, creep was not discussed since the amount of change in strain induced by creep is almost negligible compared to that induced by an incremental stress. Nevertheless, domain evolution induced by creep behaviour is still worthy of studying since an observation through a microscopy can be a direct evidence. The technique, *in situ* PFM observation of domain wall motion, has been developed in chapter 3, and hence it can be naturally extended to observing domain wall motion by creep.

Meanwhile, as discussed in chapter 1, ferroelectrics are turned into useful materials when multiple domains are poled by an electric field. However, depolarization by a mechanical stress is an important problem because it is directly related to device performance. In this thesis, micro-mechanical testing was conducted for only unpoled ferroelectric samples. Therefore, observing domain evolution during a depolarization

process by mechanical stress would be an interesting and natural extension of the research. Microscopic behaviour of ferroelectrics during depolarization process can be studied relating to the macroscopic stress, strain, and the resulting charge flow [121].

6.2.3 Novel materials and scientific challenges

Novel materials with ferroelectricity have been continuously developed. Materials such as $Pb(Mg_{1/3}Nb_{2/3})O_3 - PbTiO_3$ (PMN-PT) were developed due to their outstanding material properties including high electromechanical coupling factor [151]. And demand for lead-free ferroelectrics has been increasing due to lead toxicity, so several materials such as $K_{0.5}Na_{0.5}NbO_3$ (KNN) and $Na_{0.5}Bi_{0.5}TiO_3$ (NBT) are studied to replace lead-based ferroelectrics [152]. Scientific interest to find novel materials with ferroelectricity is also extended to biological systems including human teeth [137], seashell [139], and collagen fibrils [138]. The studies on ferroelectric behaviours in biological system include understanding domain structures as well as measuring ferroelectric material properties. $BiFeO_3$ (BFO) that shows both antiferromagnetic and ferroelectric properties has also received wide attention as a multiferroic [153], and magnetic and ferroelectric domain structures and their evolutions have been studied using magnetic force microscopy and PFM [154,155].

However, PFM studies on a novel material need some attention due to the reliability of image contrast in PFM. In general, SPM-based characterization techniques are exposed to tip-related and surface-related artefacts. In the case of PZT that was used in this thesis, typical domain patterns are already well known. However, to understand domain patterns in a novel material using PFM, a more systematic approach is required. AR-PFM is based on locally induced surface displacement that is generated only *via* converse piezoelectric effect, and hence PFM data can be discriminated from other image

artefacts. Therefore, the AR-PFM methods developed in this thesis could be reliable and powerful analytical techniques for studying novel materials.

Meanwhile, the principle of AR-PFM could also be extended to other microscopies such as ESM [140,141]. ESM was developed to study lithium-ion transport dynamics. Here, applied bias in the scanning probe causes lithium ions in the active volume to be transported to the small region below the tip. An increase in the local density of lithium ion induces a surface deformation due to the relationship between the local density of lithium ion and molar volume. Thus, the imaging principle of ESM is similar to that of PFM in that these two imaging techniques are based on locally induced surface displacement. Accordingly it would be interesting to apply the mapping method of AR-PFM to ESM, for example, to identify the orientation or anisotropy of the underlying electrode material.

6.2.4 Monte Carlo simulation of ferroelectric domain evolution

The model based on Monte Carlo method introduced in this thesis reproduced typical evolution processes of ferroelectric domains under electrical and mechanical loading. This model can be developed further as follows. First of all, in the present thesis, only two-dimensional model with four in-plane polarization directions in the tetragonal phase was developed. This could be extended to a two-and-a-half-dimensional (2.5D) model that allows out-of-plane and into-plane polarization directions as well as four in-plane polarizations while still modelling a planar region. Then, more realistic model in the tetragonal phase where six polarization directions are present can be generated. Note that this is called 2.5D since only a single layer of crystalline lattice is considered in this model. It is expected that this 2.5D model will allow generating curvy 180° domain walls consisting of out-of-plane and into-plane polarizations. A three-dimensional model would

allow more complex domain structures to be simulated, but would be 'expensive' in terms of computation.

Meanwhile, one of the main advantages of Monte Carlo method over other modelling methods is that the effect of temperature on material properties can be naturally explored. In this thesis, it was briefly demonstrated through the simulations that domain patterns and evolution processes were significantly affected by temperature; domain switching was facilitated at an elevated temperature, which is in agreement with experimental data [156–158]. And also the effect of temperature on macroscopic material properties such as remnant polarization and coercive field has been reported [156]. Thus, understanding the effect of temperature on a domain evolution process could be improved through Monte Carlo simulation.

6.2.5 Negative or zero Poisson's ratio in ferroelectrics

Though positive Poisson's ratio is typically observed from most materials, auxetic materials with negative Poisson's ratio also exist. When compressive stress is applied to auxetic materials, contraction occurs along the orthogonal direction with respect to the loading direction as well as the loading direction. Materials with negative or zero Poisson's ratio have been receiving attention due to their enhanced material properties such as indentation resistance and fracture toughness [159]. Also, these unusual material behaviours can be utilized in various devices [159,160]. Recently, it was reported that negative Poisson's ratio can be theoretically predicted in some perovskite materials such as the tetragonal phase of $PbTiO_3$ and tetragonal and rhombohedral phases of $BaTiO_3$ in certain loading directions [161]. In some devices based on ferroelectricity, this unusual material behaviour can be effectively utilized. For example, piezoceramic-polymer composites have been used in sonar sensors to solve non-ideal behaviours of dense

piezoelectric ceramics [18]. The composites consist of rods of piezoelectric ceramic surrounded by polymer, the role of the polymer being to accommodate transverse straining of the rods. Here, ferroelectrics with negative or zero Poisson's ratio would be desirable to avoid transverse expansion. This abnormal Poisson's ratio in some ferroelectrics was recently recognized, and hence it is worth studying how the microstructure and domain switching mechanism are related to this unusual behaviour.

A. Appendix

A.1 Principle of lock-in amplifier

During PFM measurements, three types of signal are used in the lock-in amplifier: the reference signal from the function generator, the output piezoresponse signal, and the lock-in reference signal generated by the lock-in amplifier itself. The reference signal (S_R) is a square wave at the frequency ω_r, which is the sync output from a function generator. If a sine wave with the frequency ω_r was used as the input signal for exciting converse piezoelectric response, the output signal (S_O) and lock-in reference signal (S_L) can be represented as $S_O = V_{sig}\sin(\omega_r t + \varphi_{sig})$ and $S_L = V_L \sin(\omega_L t + \varphi_{ref})$, respectively. Note that V_{sig} and V_L are the signal amplitudes, ω_L is the frequency of lock-in reference signal, and φ_{sig} and φ_{ref} are the phase difference between S_R and S_O, and S_R and S_L, respectively. The resulting piezoresponse sine wave S_O is multiplied by the lock-in reference signal S_L as follows:

$$S_O S_L = V_{sig}V_L \sin(\omega_r t + \varphi_{sig})\sin(\omega_L t + \varphi_{ref})$$
$$= 1/2\,V_{sig}V_L \cos[(\omega_r - \omega_L)t + \varphi_{sig} - \varphi_{ref}] - 1/2\,V_{sig}V_L \cos[(\omega_r + \omega_L)t + \varphi_{sig} + \varphi_{ref}].$$

When ω_L is equal to ω_r, $S_O S_L$ consists of a DC signal and a AC signal. The AC signal is filtered by a low pass filter, and the detected signal will be only the DC part, $X = 1/2\,V_{sig}V_L \cos(\varphi_{sig} - \varphi_{ref})$. When $\varphi_{sig} = \varphi_{ref}$, $X = 1/2\,V_{sig}V_L$, but when $\varphi_{sig} - \varphi_{ref} = 90°$, $X = 0$. To resolve the phase dependency of this signal, S_O is also multiplied by $S_L = V_L \sin(\omega_L t + \varphi_{ref} + 90°)$, generating $Y = 1/2\,V_{sig}V_L \sin(\varphi_{sig} - \varphi_{ref})$. Then, the magnitude

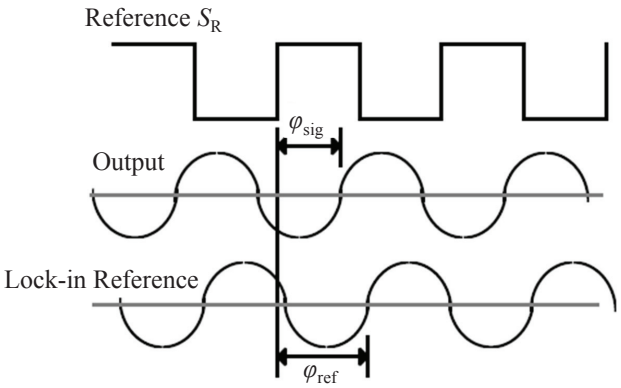

Figure A.1: Three types of signal involved in filtering the signal of interest in lock-in amplifier: reference signal, output signal, and lock-in reference signal (modified from [77]).

can be obtained by $(X^2+Y^2)^{1/2}=1/2V_{sig}V_L$, and the phase signal is $\tan^{-1}(Y/X)=\varphi_{sig}-\varphi_{ref}$.

A.2 Theoretical analysis of PFM signal

A.2.1 Transformation matrix for stress

A transformation of the stress tensor is

$$\sigma_{ij} = a_{ik} a_{jl} \sigma'_{kl}, \tag{A.1}$$

where σ_{ij} and σ'_{kl} are the stress tensor in the instrument and crystal coordinate system, respectively, and a_{ik} and a_{jl} are the direction cosines [111]. Likewise, the transformation matrix for stress written in matrix form can be represented as

$$\begin{pmatrix} \sigma_{11} \\ \sigma_{22} \\ \sigma_{33} \\ \sigma_{23} \\ \sigma_{31} \\ \sigma_{12} \end{pmatrix} = \begin{pmatrix} b_{11} & b_{12} & b_{13} & b_{14} & b_{15} & b_{16} \\ b_{21} & b_{22} & b_{23} & b_{24} & b_{25} & b_{26} \\ b_{31} & b_{32} & b_{33} & b_{34} & b_{35} & b_{36} \\ b_{41} & b_{42} & b_{43} & b_{44} & b_{45} & b_{46} \\ b_{51} & b_{52} & b_{53} & b_{54} & b_{55} & b_{56} \\ b_{61} & b_{62} & b_{63} & b_{64} & b_{65} & b_{66} \end{pmatrix} \begin{pmatrix} \sigma'_{11} \\ \sigma'_{22} \\ \sigma'_{33} \\ \sigma'_{23} \\ \sigma'_{31} \\ \sigma'_{12} \end{pmatrix}. \tag{A.2}$$

Elements of the transformation matrix $B_{m,n}$ can be identified by comparing them with the corresponding elements in the stress tensor. For example,

$$\sigma_{11} = b_{11}\sigma'_{11} + b_{12}\sigma'_{22} + b_{13}\sigma'_{33} + b_{14}\sigma'_{23} + b_{15}\sigma'_{31} + b_{16}\sigma'_{12}, \tag{A.3}$$

$$\begin{aligned} \sigma_{11} = {} & a_{11}a_{11}\sigma'_{11} + a_{11}a_{12}\sigma'_{12} + a_{11}a_{13}\sigma'_{13} + a_{12}a_{11}\sigma'_{21} + a_{12}a_{12}\sigma'_{22} + a_{12}a_{13}\sigma'_{23} \\ & + a_{13}a_{11}\sigma'_{31} + a_{13}a_{12}\sigma'_{32} + a_{13}a_{13}\sigma'_{33}. \end{aligned} \tag{A.4}$$

Thus, the transformation matrix for stress written in matrix form can be represented as

$$\boldsymbol{B} = \begin{pmatrix} a_{11}^2 & a_{12}^2 & a_{13}^2 & 2a_{12}a_{13} & 2a_{13}a_{11} & 2a_{11}a_{12} \\ a_{21}^2 & a_{22}^2 & a_{23}^2 & 2a_{22}a_{23} & 2a_{23}a_{21} & 2a_{21}a_{22} \\ a_{31}^2 & a_{32}^2 & a_{33}^2 & 2a_{32}a_{33} & 2a_{33}a_{31} & 2a_{31}a_{32} \\ a_{21}a_{31} & a_{22}a_{32} & a_{23}a_{33} & a_{22}a_{33} + a_{23}a_{32} & a_{21}a_{33} + a_{23}a_{31} & a_{22}a_{31} + a_{21}a_{32} \\ a_{31}a_{11} & a_{32}a_{12} & a_{33}a_{13} & a_{12}a_{33} + a_{13}a_{32} & a_{13}a_{31} + a_{11}a_{33} & a_{11}a_{32} + a_{12}a_{31} \\ a_{11}a_{21} & a_{12}a_{22} & a_{13}a_{23} & a_{12}a_{23} + a_{13}a_{22} & a_{13}a_{21} + a_{11}a_{23} & a_{11}a_{22} + a_{12}a_{21} \end{pmatrix}. \tag{A.5}$$

A.2.2 Transformation of piezoelectric coefficient matrix

From equation (A.2), $\boldsymbol{\sigma} = \boldsymbol{B}\boldsymbol{\sigma}'$, $\boldsymbol{\sigma}' = \boldsymbol{B}^{-1}\boldsymbol{\sigma}$, where $\boldsymbol{\sigma}$ and $\boldsymbol{\sigma}'$ are the stress matrix in the instrument and crystal coordinate system, respectively. Also $\mathbf{P}' = \boldsymbol{d}'\boldsymbol{\sigma}'$, where $\mathbf{P}'$ is the polarization, and $\boldsymbol{d}'$ is the piezoelectric coefficient matrix. If $\boldsymbol{R}$ is the rotation matrix, $\mathbf{P} = \boldsymbol{R}\mathbf{P}' = \boldsymbol{R}\boldsymbol{d}'\boldsymbol{\sigma}' = \boldsymbol{R}\boldsymbol{d}'\boldsymbol{B}^{-1}\boldsymbol{\sigma}$, and $\mathbf{P} = \boldsymbol{d}\boldsymbol{\sigma}$ [111]. Therefore,

$$\boldsymbol{d} = \boldsymbol{R}\boldsymbol{d}'\boldsymbol{B}^{-1}. \tag{A.6}$$

The rotation matrix $\boldsymbol{R}$ can be represented using the three Euler angles $(\varphi_1, \Phi, \varphi_2)$ as

$$\boldsymbol{R} = \begin{bmatrix} \cos\varphi_1 cos\varphi_2 - \cos\Phi sin\varphi_1 sin\varphi_2 & \cos\varphi_2 sin\varphi_1 + cos\varphi_1 \cos\Phi sin\varphi_2 & \sin\varphi_2 \sin\Phi \\ -\cos\varphi_1 sin\varphi_2 - cos\varphi_2 \cos\Phi sin\varphi_1 & \cos\varphi_1 cos\varphi_2 \cos\Phi - sin\varphi_1 sin\varphi_2 & \cos\varphi_2 \sin\Phi \\ \sin\varphi_1 \sin\Phi & -\cos\varphi_1 \sin\Phi & \cos\Phi \end{bmatrix}. \tag{A.7}$$

And, the piezoelectric coefficient matrix $\boldsymbol{d}'$ is

$$\boldsymbol{d}' = \begin{pmatrix} d'_{11} & d'_{12} & d'_{13} & d'_{14} & d'_{15} & d'_{16} \\ d'_{21} & d'_{22} & d'_{23} & d'_{24} & d'_{25} & d'_{26} \\ d'_{31} & d'_{32} & d'_{33} & d'_{34} & d'_{35} & d'_{36} \end{pmatrix}. \tag{A.8}$$

Finally, the reverse relationship between the stress tensors in the crystal and instrument coordinate system in equation (A.1) [162] is

$$\sigma'_{ij} = a_{ki} a_{lj} \sigma_{kl}. \tag{A.9}$$

Therefore,

$$\boldsymbol{B}^{-1} = \begin{pmatrix} a_{11}^2 & a_{21}^2 & a_{31}^2 & 2a_{21}a_{31} & 2a_{31}a_{11} & 2a_{11}a_{21} \\ a_{12}^2 & a_{22}^2 & a_{32}^2 & 2a_{22}a_{32} & 2a_{32}a_{12} & 2a_{12}a_{22} \\ a_{13}^2 & a_{23}^2 & a_{33}^2 & 2a_{23}a_{33} & 2a_{33}a_{13} & 2a_{13}a_{23} \\ a_{12}a_{13} & a_{22}a_{23} & a_{32}a_{33} & a_{22}a_{33} + a_{32}a_{23} & a_{12}a_{33} + a_{32}a_{13} & a_{22}a_{13} + a_{12}a_{23} \\ a_{13}a_{11} & a_{23}a_{21} & a_{33}a_{31} & a_{21}a_{33} + a_{31}a_{23} & a_{31}a_{13} + a_{11}a_{33} & a_{11}a_{23} + a_{21}a_{13} \\ a_{11}a_{12} & a_{21}a_{22} & a_{31}a_{32} & a_{21}a_{32} + a_{31}a_{22} & a_{31}a_{12} + a_{11}a_{32} & a_{11}a_{22} + a_{21}a_{12} \end{pmatrix}. \tag{A.10}$$

Accordingly, the piezoelectric coefficients $\boldsymbol{d}$ in equation (A.6) can be obtained using equations (A.7), (A.8), and (A.10).

A.2.3 Formulating vertical PFM signal using the elements of piezoelectric coefficient matrix and rotation matrix

The converse piezoelectric effect is represented as

$$\begin{pmatrix} \varepsilon_{11} \\ \varepsilon_{22} \\ \varepsilon_{33} \\ 2\varepsilon_{23} \\ 2\varepsilon_{31} \\ 2\varepsilon_{12} \end{pmatrix} = \begin{pmatrix} d_{11} & d_{21} & d_{31} \\ d_{12} & d_{22} & d_{32} \\ d_{13} & d_{23} & d_{33} \\ d_{14} & d_{24} & d_{34} \\ d_{15} & d_{25} & d_{35} \\ d_{16} & d_{26} & d_{36} \end{pmatrix} \begin{pmatrix} E_1 \\ E_2 \\ E_3 \end{pmatrix}, \tag{A.11}$$

where $\varepsilon_{11}, \varepsilon_{22}, \varepsilon_{33}, \varepsilon_{23}, \varepsilon_{31}, \varepsilon_{12}$ are the elements of strain matrix. In the present work, the electric field vector $\mathbf{E}$ was assumed to be $\mathbf{E} = \begin{bmatrix} 0 & 0 & E_3 \end{bmatrix}^{\mathrm{T}}$ as shown in figure A.2. Note that the divergence of the electric field from the tip is not considered, this model gives a good first approximation [75].

Meanwhile, the strain matrix is related to the displacement vector $\mathbf{u} = (u_1, u_2, u_3)$ as follows [75]:

$$\begin{pmatrix} \varepsilon_{11} & \varepsilon_{12} & \varepsilon_{13} \\ \varepsilon_{21} & \varepsilon_{22} & \varepsilon_{23} \\ \varepsilon_{31} & \varepsilon_{32} & \varepsilon_{33} \end{pmatrix} = \begin{pmatrix} \dfrac{\partial u_1}{\partial x_1} & \dfrac{1}{2}\left(\dfrac{\partial u_1}{\partial x_2} + \dfrac{\partial u_2}{\partial x_1}\right) & \dfrac{1}{2}\left(\dfrac{\partial u_1}{\partial x_3} + \dfrac{\partial u_3}{\partial x_1}\right) \\ \dfrac{1}{2}\left(\dfrac{\partial u_2}{\partial x_1} + \dfrac{\partial u_1}{\partial x_2}\right) & \dfrac{\partial u_2}{\partial x_2} & \dfrac{1}{2}\left(\dfrac{\partial u_2}{\partial x_3} + \dfrac{\partial u_3}{\partial x_2}\right) \\ \dfrac{1}{2}\left(\dfrac{\partial u_3}{\partial x_1} + \dfrac{\partial u_1}{\partial x_3}\right) & \dfrac{1}{2}\left(\dfrac{\partial u_3}{\partial x_2} + \dfrac{\partial u_2}{\partial x_3}\right) & \dfrac{\partial u_3}{\partial x_3} \end{pmatrix}. \tag{A.12}$$

From equations (A.11) and (A.12), the relationship between the elements of surface displacement vector and the elements of piezoelectric coefficient matrix is as follows:

$$\varepsilon_{11} = \frac{\partial u_1}{\partial x_1} = d_{31} E_3,$$

$$\varepsilon_{22} = \frac{\partial u_2}{\partial x_2} = d_{32} E_3,$$

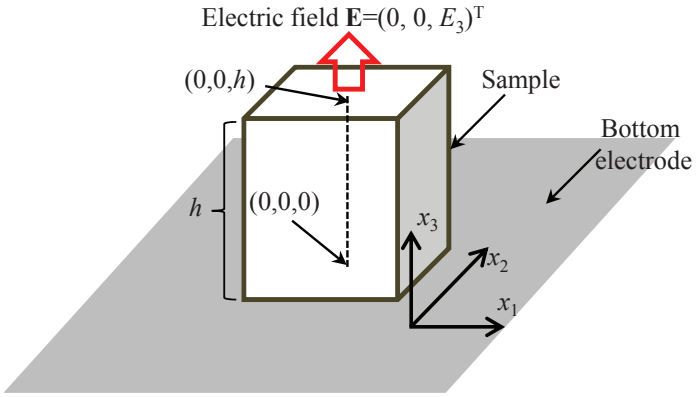

Figure A.2: Schematic showing the electric field vector **E**, the instrument coordinate system and the sample.

$$\varepsilon_{33} = \frac{\partial u_3}{\partial x_3} = d_{33}E_3,$$

$$\varepsilon_{23} = \frac{1}{2}\left(\frac{\partial u_2}{\partial x_3} + \frac{\partial u_3}{\partial x_2}\right) = \frac{1}{2}d_{34}E_3.$$

$$\varepsilon_{31} = \frac{1}{2}\left(\frac{\partial u_3}{\partial x_1} + \frac{\partial u_1}{\partial x_3}\right) = \frac{1}{2}d_{35}E_3,$$

$$\varepsilon_{12} = \frac{1}{2}\left(\frac{\partial u_1}{\partial x_2} + \frac{\partial u_2}{\partial x_1}\right) = \frac{1}{2}d_{36}E_3. \qquad \text{(A.13)}$$

Using the boundary conditions $u_1(0,0,0) = 0$, $u_2(0,0,0) = 0$ and $u_3(x_1, x_2, 0) = 0$, the equation (A.13) can be solved [75], giving

$$u_3 = d_{33}E_3h = d_{33}V. \qquad \text{(A.14)}$$

Therefore, vertical PFM signal u_3V^{-1} equals to d_{33}. In the crystal coordinate system, the piezoelectric coefficient matrix $\boldsymbol{d'}$ in tetragonal is

$$\boldsymbol{d'} = \begin{pmatrix} 0 & 0 & 0 & 0 & d'_{15} & 0 \\ 0 & 0 & 0 & d'_{15} & 0 & 0 \\ d'_{31} & d'_{31} & d'_{33} & 0 & 0 & 0 \end{pmatrix}. \qquad \text{(A.15)}$$

Therefore,

$$d_{33} = d'_{33}\cos^3(\Phi) + (d'_{31} + d'_{15})\cos(\Phi)\sin^2(\Phi). \qquad \text{(A.16)}$$

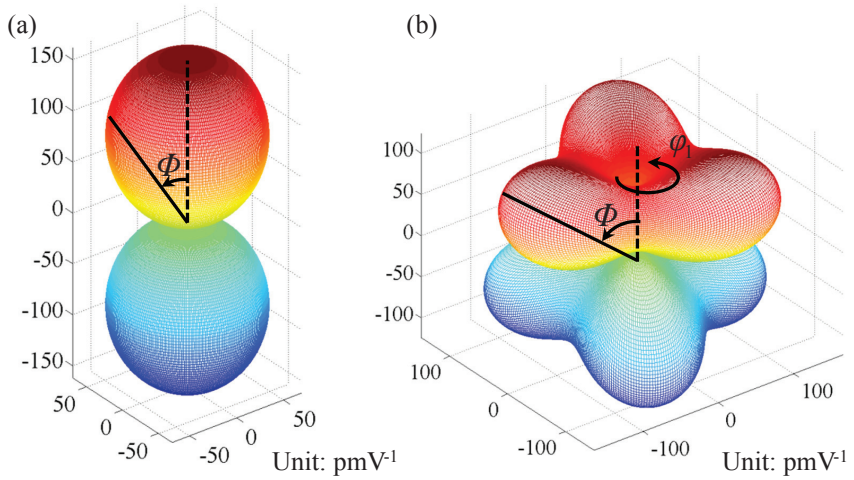

Figure A.3: The d_{33} coefficient in (a) tetragonal and (b) rhombohedral PZT depending on crystal orientation. The piezoelectric coefficients are from the previous work [78].

Meanwhile, in rhombohedral the piezoelectric coefficient matrix is

$$\boldsymbol{d}' = \begin{pmatrix} 0 & 0 & 0 & 0 & d'_{15} & -2d'_{22} \\ -d'_{22} & d'_{22} & 0 & d'_{15} & 0 & 0 \\ d'_{31} & d'_{31} & d'_{33} & 0 & 0 & 0 \end{pmatrix}. \tag{A.17}$$

Therefore,

$$\begin{aligned} d_{33} = {} & d'_{33}\cos^3(\Phi) + (d'_{31} + d'_{15})\cos(\Phi)\sin^2(\Phi) + \\ & d'_{22}\cos(\varphi_1)\sin^3(\Phi)(3\sin^2(\varphi_1) - \cos^2(\varphi_1)). \end{aligned} \tag{A.18}$$

Figure A.3 shows the three-dimensional graph of d_{33} in tetragonal and rhombohedral PZT, respectively from equations (A.16) and (A.18). In tetragonal, the d_{33} values have axisymmetric shape, and are only affected by the rotation angle Φ. The maximum d_{33} value occurs when $\Phi = 0$. Meanwhile, in rhombohedral the shape of the graph is not axisymmetric, and affected by the rotation angle φ_1 as well as Φ. Unlike in tetragonal, the maximum d_{33} can be found at the certain rotation angle φ_1 and $\Phi \neq 0$, as previously reported [107]. See the literatures [75,78,107,108] for the further details. In this thesis, the effective piezoelectric coefficient d_{zz} represents d_{33} in equations (A.16) and (A.18).

A.3 Matrices in cubic phase

The elastic constant matrix in cubic phase is

$$\begin{pmatrix} C_{11} & C_{12} & C_{12} & 0 & 0 & 0 \\ C_{12} & C_{11} & C_{12} & 0 & 0 & 0 \\ C_{12} & C_{12} & C_{11} & 0 & 0 & 0 \\ 0 & 0 & 0 & C_{44} & 0 & 0 \\ 0 & 0 & 0 & 0 & C_{44} & 0 \\ 0 & 0 & 0 & 0 & 0 & C_{44} \end{pmatrix}. \tag{A.19}$$

The electrostriction matrix in cubic phase is

$$\begin{pmatrix} q_{11} & q_{12} & q_{12} & 0 & 0 & 0 \\ q_{12} & q_{11} & q_{12} & 0 & 0 & 0 \\ q_{12} & q_{12} & q_{11} & 0 & 0 & 0 \\ 0 & 0 & 0 & q_{44} & 0 & 0 \\ 0 & 0 & 0 & 0 & q_{44} & 0 \\ 0 & 0 & 0 & 0 & 0 & q_{44} \end{pmatrix}. \tag{A.20}$$

The local gradient matrix in cubic phase is

$$\begin{pmatrix} G_{11} & G_{12} & G_{12} & 0 & 0 & 0 \\ G_{12} & G_{11} & G_{12} & 0 & 0 & 0 \\ G_{12} & G_{12} & G_{11} & 0 & 0 & 0 \\ 0 & 0 & 0 & G_{44} & 0 & 0 \\ 0 & 0 & 0 & 0 & G_{44} & 0 \\ 0 & 0 & 0 & 0 & 0 & G_{44} \end{pmatrix}. \tag{A.21}$$

A.4 Publications and presentations

List of publications, conference proceedings:

- Kim KL, Huber JE. Observation of the poling process in ferroelectric ceramics using piezoresponse force microscopy. ASME 2012 Conf. Smart Mater. Adapt. Struct. Intell. Syst., Stone Mountain, Georgia, USA: 2012, p. 155–60.
- Kim KL, Tsou NT, Huber JE. Domain evolution processes during poling of a near-morphotropic Pb(Zr, Ti)O_3 ceramic. J Appl Phys 2013;113:194104–1–11.
- Kim KL, Huber JE. Identifying ferroelectric phase and domain structure using angle-resolved piezoresponse force microscopy. Appl Phys Lett 2014;104:122901–1–4.
- Kim KL, Huber JE. Mapping of ferroelectric domain structure using angle-resolved piezoresponse force microscopy. Rev Sci Instrum 2015;86:013705–1–11.
- Kim KL, Huber JE. *In situ* observation of ferroelastic domain evolution in a near-morphotropic Pb(Zr,Ti)O_3 ceramic by piezoresponse force microscopy. J Eur Ceram Soc 2015;35:1459–68.

Conference presentations/seminars:

- Observation of the poling process in ferroelectric ceramics using piezoresponse force microscopy, ASME, Stone Mountain, USA, September 2012.
- Observation of domain evolution in a ferroelectric material using piezoresponse force microscopy, Laboratory for *In situ* Microscopy & Analysis Users Club Meeting, Oxford, UK, March 2013.
- Phase identification of ferroelectric domain structure using angle-resolved piezoresponse force microscopy, Laboratory for *In situ* Microscopy & Analysis Users Club Meeting, Oxford, UK, March 2014.

References

[1] Nguyen TD, Deshmukh N, Nagarah JM, Kramer T, Purohit PK, Berry MJ, et al. Piezoelectric nanoribbons for monitoring cellular deformations. Nat Nanotechnol 2012;7:587–93.

[2] Qi Y, Kim J, Nguyen TD, Lisko B, Purohit PK, McAlpine MC. Enhanced piezoelectricity and stretchability in energy harvesting devices fabricated from buckled PZT ribbons. Nano Lett 2011;11:1331–6.

[3] Chen X, Xu S, Yao N, Shi Y. 1.6 V nanogenerator for mechanical energy harvesting using PZT nanofibers. Nano Lett 2010;10:2133–7.

[4] Hajati A, Latev D, Gardner D, Hajati A, Imai D, Torrey M, et al. Three-dimensional micro electromechanical system piezoelectric ultrasound transducer. Appl Phys Lett 2012;101:253101–1–5.

[5] Forrester JS, Kisi EH. Ferroelastic switching in a soft lead zirconate titanate. J Eur Ceram Soc 2004;24:595–602.

[6] Hwang SC, Lynch CS, McMeeking RM. Ferroelectric/ferroelastic interactions and a polarization switching model. Acta Met Mater 1995;43:2073–84.

[7] Cao H, Evans AG. Nonlinear deformation of ferroelectric ceramics. J Am Ceram Soc 1993;76:890–6.

[8] Lynch CS. The effect of uniaxial stress on the electro-mechanical response of 8/65/35 PLZT. Acta Mater 1996;44:4137–48.

[9] Arlt G. The influence of microstructure on the properties of ferroelectric ceramics. Ferroelectrics 1990;104:217–27.

[10] Nagarajan V, Roytburd A, Stanishevsky A, Prasertchoung S, Zhao T, Chen L, et al. Dynamics of ferroelastic domains in ferroelectric thin films. Nat Mater 2003;2:43–7.

[11] Haertling GH. Ferroelectric ceramics : history and technology. J Am Ceram Soc 1999;82:797–818.

[12] Valasek J. Piezo-electric and allied phenomena in Rochelle salt. Phys Rev 1921;17:475–81.

[13] Jaffe B, Roth RS, Marzullo S. Piezoelectric properties of lead zirconate-lead titanate solid-solution ceramics. J Appl Phys 1954;25:809–10.

[14] Jaffe B, Cook WR, Jaffe H. Piezoelectric ceramics. London; New York: Academic Press; 1971.

[15] Gupta SM, Viehland D. Tetragonal to rhombohedral transformation in the lead zirconium titanate lead magnesium niobate-lead titanate crystalline solution. J Appl Phys 1998;83:407–14.

[16] Kugel VD, Cross LE. Behavior of soft piezoelectric ceramics under high sinusoidal electric fields. J Appl Phys 1998;84:2815–30.

[17] Liu M, Hsia KJ, Sardela MR. In situ X-Ray diffraction study of electric-field-induced domain switching and phase transition in PZT-5H. J Am Ceram Soc 2005;88:210–5.

[18] Moulson AJ, Herbert JM. Electroceramics: materials, properties , applications. Second Ed. Chichester: John Wiley & Sons Ltd; 2003.

[19] Tsou NT, Huber JE. Compatible domain structures and the poling of single crystal ferroelectrics. Mech Mater 2010;42:740–53.

[20] Shu YC, Bhattacharya K. Domain patterns and macroscopic behaviour of ferroelectric materials. Philos Mag Part B 2001;81:2021–54.

[21] Tsou NT, Potnis PR, Huber JE. Classification of laminate domain patterns in ferroelectrics. Phys Rev B 2011;83:184120–1–6.

[22] DeVries RC, Burke JE. Microstructure of barium titanate ceramics. J Am Ceram Soc 1957;40:200–6.

[23] Arlt G, Sasko P. Domain configuration and equilibrium size of domains in $BaTiO_3$ ceramics. J Appl Phys 1980;51:4956–60.

[24] Goldsztein GH. The effective energy and laminated microstructures in martensitic phase transformations. J Mech Phys Solids 2001;49:899–925.

[25] IEEE. IEEE standard on piezoelectricity. ANSI/IEEE Std 176-1987 1988;1:1–66.

[26] Scott JF, Paz De Araujo CA. Ferroelectric memories. Science 1989;246:1400–5.

[27] Ren SB, Lu CJ, Shen HM, Wang YN. In situ study of the evolution of domain structure in free-standing polycrystalline $PbTiO_3$ thin films under external stress. Phys Rev B 1997;55:3485–9.

[28] Wang J, Shi SQ, Chen LQ, Li Y, Zhang TY. Phase field simulations of ferroelectric/ferroelastic polarization switching. Acta Mater 2004;52:749–64.

[29] Chan CJ, Lange FF, Ruhle M, Jue JF, Virkar A V. Ferroelastic domain switching in tetragonal zirconia single crystals - microstructural aspects. J Am Ceram Soc 1991;74:807–13.

[30] Merz WJ. Domain formation and domain wall motions in ferroelectric $BaTiO_3$ single crystals. Phys Rev 1954;95:690–8.

[31] Miller RC, Savage A. Velocity of sidewise 180° domain-wall motion in $BaTiO_3$ as a function of the applied electric field. Phys Rev 1958;112:755–62.

[32] Little EA. Dynamic behavior of domain walls in barium titanate. Phys Rev 1955;98:978–84.

[33] Muñoz-Saldaña J, Schneider GA, Eng LM. Stress induced movement of ferroelastic domain walls in $BaTiO_3$ single crystals evaluated by scanning force microscopy. Surf Sci 2001;480:L402–L410.

[34] Zhang ZH, Qi XY, Duan XF. Direct determination of the polarization direction of domains in $BaTiO_3$ single crystal. Appl Phys Lett 2006;89:242905–1–3.

[35] Li Z, Foster CM, Dai XH, Xu XZ, Chan SK, Lam DJ. Piezoelectrically-induced switching of 90° domains in tetragonal $BaTiO_3$ and $PbTiO_3$ investigated by micro-Raman spectroscopy. J Appl Phys 1992;71:4481–6.

[36] Potnis PR, Tsou NT, Huber JE. A review of domain modelling and domain imaging techniques in ferroelectric crystals. Materials 2011;4:417–47.

[37] Soergel E. Visualization of ferroelectric domains in bulk single crystals. Appl Phys B 2005;81:729–52.

[38] Pearson GL, Feldmann WL. Powder-pattern techniques for delineating ferroelectric domain structures. J Phys Chem Solids 1958;9:28–30.

[39] Furuhata Y, Toriyama K. New liquid-crystal method for revealing ferroelectric domains. Appl Phys Lett 1973;23:361–2.

[40] Bluhm H, Wadas A, Wiesendanger R, Roshko A, Aust JA, Nam D. Imaging of domain-inverted gratings in $LiNbO_3$ by electrostatic force microscopy. Appl Phys Lett 1997;71:146–8.

[41] Hooton JA, Merz WJ. Etch patterns and ferroelectric domains in $BaTiO_3$ single crystals. Phys Rev 1955;98:409–13.

[42] Soergel E. Piezoresponse force microscopy (PFM). J Phys D Appl Phys 2011;44:464003–1–17.

[43] Ivry Y, Chu DP, Scott JF, Durkan C. Flux closure vortexlike domain structures in ferroelectric thin films. Phys Rev Lett 2010;104:207602–1–4.

[44] Zhang BY, Jiang FM, Yang Y, Yin QR, Kojima S. Electron acoustic imaging of $BaTiO_3$ single crystals. J Appl Phys 1996;80:1916–8.

[45] Liu XX, Heiderhoff R, Abicht HP, Balk LJ. Scanning near-field acoustic study of ferroelectric $BaTiO_3$ ceramics. Inst Phys Publ 2002;35:74–87.

[46] Merz WJ. Domain properties in $BaTiO_3$. Phys Rev 1952;88:421–2.

[47] Pan K, Liu YM, Liu YY, Li JY. Resolving ferroelectric nanostructures via piezoresponse force microscopy—A numerical investigation. J Appl Phys 2013;113:187223–1–5.

[48] Yoo H, Bae C, Kim M, Hong S, No K, Kim Y, et al. Visualization of three dimensional domain structures in ferroelectric $PbTiO_3$ nanotubes. Appl Phys Lett 2013;103:022902–1–4.

[49] Ivry Y, Chu DP, Durkan C. Nanometer resolution piezoresponse force microscopy to study deep submicron ferroelectric and ferroelastic domains. Appl Phys Lett 2009;94:162903–1–3.

[50] Ivry Y, Wang N, Chu DP, Durkan C. 90° domain dynamics and relaxation in thin ferroelectric/ferroelastic films. Phys Rev B 2010;81:174118–1–8.

[51] Polomoff NA, Premnath RN, Bosse JL, Huey BD. Ferroelectric domain switching dynamics with combined 20 nm and 10 ns resolution. J Mater Sci 2009;44:5189–96.

[52] Nath R, Chu YH, Polomoff NA, Ramesh R, Huey BD. High speed piezoresponse force microscopy: <1 frame per second nanoscale imaging. Appl Phys Lett 2008;93:072905–1–3.

[53] Huey BD, Premnath RN, Lee S, Polomoff NA. High speed SPM applied for direct nanoscale mapping of the influence of defects on ferroelectric switching dynamics. J Am Ceram Soc 2012;95:1147–62.

[54] Potnis P, Huber J. In-situ observation of needle domain evolution in barium titanate single crystals. J Eur Ceram Soc 2013;33:327–33.

[55] Jiang B, Bai Y, Chu W, Su Y, Qiao L. Direct observation of two 90° steps of 180° domain switching in $BaTiO_3$ single crystal under an antiparallel electric field. Appl Phys Lett 2008;93:152905–1–3.

[56] Hu YH, Chan HM, Wen ZX, Harmer MP. Scanning electron microscopy and transmission electron microscopy study of ferroelectric domains in doped $BaTiO_3$. J Am Ceram Soc 1986;69:594–602.

[57] Burnett TL, Weaver PM, Blackburn JF, Stewart M, Cain MG. Correlation of electron backscatter diffraction and piezoresponse force microscopy for the nanoscale characterization of ferroelectric domains in polycrystalline lead zirconate titanate. J Appl Phys 2010;108:042001–1–7.

[58] Okayasu M, Sato K, Kusaba Y. Domain switching characteristics of lead zirconate titanate piezoelectric ceramics during mechanical compressive loading. J Eur Ceram Soc 2011;31:129–40.

[59] Jia CL, Mi SB, Urban K, Vrejoiu I, Alexe M, Hesse D. Atomic-scale study of electric dipoles near charged and uncharged domain walls in ferroelectric films. Nat Mater 2008;7:57–61.

[60] Tan X, Shang JK. Intersection of a domains in the c-domain matrix driven by electric field in tetragonal ferroelectric crystal. J Appl Phys 2004;96:2805–10.

[61] Qi XY, Liu HH, Duan XF. In situ transmission electron microscopy study of electric-field-induced 90° domain switching in $BaTiO_3$ single crystals. Appl Phys Lett 2006;89:092908–1–3.

[62] Zhang ZH, Qi XY, Duan XF. Two-step evolution mechanism of multi-domains in $BaTiO_3$ single crystal investigated by in situ transmission electron microscopy. Scr Mater 2008;58:441–4.

[63] Jones JL. The use of diffraction in the characterization of piezoelectric materials. J Electroceramics 2007;19:67–79.

[64] Hall DA, Steuwer A, Cherdhirunkorn B, Withers PJ, Mori T. Micromechanics of domain switching in rhombohedral PZT ceramics. Ceram Int 2008;34:679–83.

[65] Jones JL, Slamovich EB, Bowman KJ. Domain texture distributions in tetragonal lead zirconate titanate by X-ray and neutron diffraction. J Appl Phys 2005;97:034113–1–6.

[66] Niizeki N, Hasegawa M. Direct observation of antiparallel 180° domains in $BaTiO_3$ by X-ray anomalous dispersion method. J Phys Soceity Japan 1964;19:550–4.

[67] Fogarty G, Steiner B, Cronin-Golomb M, Laor U, Garrett MH, Martin J, et al. Antiparallel ferroelectric domains in photorefractive barium titanate and strontium barium niobate observed by high-resolution X-ray diffraction imaging. J Opt Soc Am B 1996;13:2636–43.

[68] Binnig G, Quate CF. Atomic force microscope. Phys Rev Lett 1986;56:930–3.

[69] Eaton P, West P. Atomic force microscopy. Oxford: Oxford University Press; 2010.

[70] Oliver RA. Advances in AFM for the electrical characterization of semiconductors. Reports Prog Phys 2008;71:1–37.

[71] Sumner J, Bakshi SD, Oliver RA, Kappers MJ, Humphreys CJ. Unintentional doping in GaN assessed by scanning capacitance microscopy. Phys Status Solidi 2008;245:896–8.

[72] Erts D, Polyakov B, Daly B, Morris MA, Ellingboe S, Boland J, et al. High density germanium nanowire assemblies : contact challenges and electrical characterization. J Phys Chem B 2006;110:820–6.

[73] Kuramochi H, Uzumaki T, Yasutake M, Tanaka A, Akinaga H, Yokoyama H. A magnetic force microscope using CoFe-coated carbon nanotube probes. Nanotechnology 2005;16:24–7.

[74] Nozaki Y, Ohta M, Taharazako S, Tateishi K, Yoshimura S, Matsuyama K. Magnetic force microscopy study of microwave-assisted magnetization reversal in submicron-scale ferromagnetic particles. Appl Phys Lett 2007;91:082510–1–3.

[75] Kalinin S V, Rodriguez BJ, Jesse S, Shin J, Baddorf AP, Gupta P, et al. Vector piezoresponse force microscopy. Microsc Microanal 2006;12:206–20.

[76] Rodriguez BJ, Jesse S, Morozovska AN, Svechnikov S V, Kiselev DA, Kholkin AL, et al. Real space mapping of polarization dynamics and hysteresis loop formation in relaxor-ferroelectric $PbMg_{1/3}Nb_{2/3}O_3$-$PbTiO_3$ solid solutions. J Appl Phys 2010;108:042006–1–11.

[77] Model SR830 DSP lock-in amplifier user's manual 2011;5.

[78] Du XH, Belegundu U, Uchino K. Crystal orientation dependence of piezoelectric properties in lead zirconate titanate: theoretical expectation for thin films. Jpn J Appl Phys 1997;36:5580–7.

[79] Rodriguez BJ, Gruverman A, Kingon AI, Namanich RJ, Cross JS. Three-dimensional high-resolution reconstruction of polarization in ferroelectric capacitors by piezoresponse force microscopy. J Appl Phys 2004;95:1958–62.

[80] Eng LM, Güntherodt HJ, Schneider GA, Köpke U, Muñoz Saldaña J. Nanoscale reconstruction of surface crystallography from three-dimensional polarization distribution in ferroelectric barium–titanate ceramics. Appl Phys Lett 1999;74:233–5.

[81] Huber JE. Micromechanical modelling of ferroelectrics. Curr Opin Solid State Mater Sci 2005;9:100–6.

[82] Huber JE, Fleck NA. Multi-axial electrical switching of a ferroelectric: theory versus experiment. J Mech Phys Solids 2001;49:785–811.

[83] Landis CM. Fully coupled , multi-axial , symmetric constitutive laws for polycrystalline ferroelectric ceramics. J Mech Phys Solids 2002;50:127–52.

[84] Huber JE, Fleck NA, Landis CM, McMeeking RM. A constitutive model for ferroelectric polycrystals. J Mech Phys Solids 1999;47:1663–97.

[85] Yen JH, Shu YC, Shieh J, Yeh JH. A study of electromechanical switching in ferroelectric single crystals. J Mech Phys Solids 2008;56:2117–35.

[86] Weng GJ, Wong DT. Thermodynamic driving force in ferroelectric crystals with a rank-2 laminated domain pattern, and a study of enhanced electrostriction. J Mech Phys Solids 2009;57:571–97.

[87] Tsou NT, Huber JE, Cocks ACF. Evolution of compatible laminate domain structures in ferroelectric single crystals. Acta Mater 2013;61:670–82.

[88] Hu HL, Chen LQ. Computer simulation of 90° ferroelectric domain formation in two-dimensions. Mater Sci Eng 1997;A238:182–91.

[89] Yang W, Chen LQ. Computer simulation of the dynamics of 180° ferroelectric domains. J Am Ceram Soc 1995;78:2554–6.

[90] Choudhury S, Chen LQ, Li YL. Correlation between number of ferroelectric variants and coercive field of lead ziconate titanate single crystals. Appl Phys Lett 2007;91:032902–1–3.

[91] Chen LQ. Phase-field models for microstructure evolution. Annu Rev Mater Res 2002;32:113–40.

[92] Hu HL, Chen LQ. Three-dimensional computer simulation of ferroelectric domain formation. J Am Ceram Soc 1998;81:492–500.

[93] Landau DP, Binder K. A guide to monte carlo simulations in statistical physics. Cambridge: Cambridge University Press; 2000.

[94] Metropolis N, Rosenbluth AW, Rosenbluth MN, Teller AH, Teller E. Equation of state calculations by fast computing machines. J Chem Phys 1953;21:1087–92.

[95] Yao J, Yang Y, Ge W, Li J, Viehland D. Domain evolution in $PbMg_{1/3}Nb_{2/3}O_3$-60at%$PbTiO_3$ with temperature and electric field. J Am Ceram Soc 2011;94:2479–82.

[96] Tan X, Shang JK. Field-induced domain interpenetration in tetragonal ferroelectric crystal. J Appl Phys 2004;95:635–9.

[97] Potnis PR. Single crystal ferroelectrics: Macroscopic and microscopic studies. University of Oxford, 2011.

[98] Gruverman A, Auciello O, Tokumoto H. Imaging and control of domain structures in ferroelectric thin films via scanning force microscopy. Annu Rev Mater Sci 1998;28:101–23.

[99] Kalinin S V, Morozovska AN, Chen LQ, Rodriguez BJ. Local polarization dynamics in ferroelectric materials. Reports Prog Phys 2010;73:056502–1–67.

[100] Panwar N, Coondoo I, Tomar A, Kholkin AL, Puli VS, Katiyar RS. Nanoscale piezoresponse and magnetic studies of multiferroic Co and Pr co-substituted BFO thin films. Mater Res Bull 2012;47:4240–5.

[101] Wu A, Vilarinho PM, Shvartsman V V, Suchaneck G, Kholkin AL. Domain populations in lead zirconate titanate thin films of different compositions via piezoresponse force microscopy. Nanotechnology 2005;16:2587–95.

[102] Gruverman A. Scaling effect on statistical behavior of switching parameters of ferroelectric capacitors. Appl Phys Lett 1999;75:1452–4.

[103] Lines ME, Glass AM. Principles and applications of ferroelectrics and related materials. Oxford: Clarendon Press; 1977.

[104] Sawyer CB, Tower CH. Rochelle salt as a dielectric. Phys Rev 1930;35:269–73.

[105] Jesse S, Baddorf AP, Kalinin S V. Dynamic behaviour in piezoresponse force microscopy. Nanotechnology 2006;17:1615–28.

[106] Jungk T, Hoffmann Á, Soergel E. Impact of the tip radius on the lateral resolution in piezoresponse force microscopy. New J Phys 2008;10:013019–1–9.

[107] Du XH, Zheng J, Belegundu U, Uchino K. Crystal orientation dependence of piezoelectric properties of lead zirconate titanate near the morphotropic phase boundary. Appl Phys Lett 1998;72:2421–3.

[108] Harnagea C, Pignolet A, Alexe M, Hesse D. Piezoresponse scanning force microscopy: what quantitative information can we really get out of piezoresponse measurements on ferroelectric thin films. Integr Ferroelectr 2002;44:113–24.

[109] Rodriguez BJ, Callahan C, Kalinin S V, Proksch R. Dual-frequency resonance-tracking atomic force microscopy. Nanotechnology 2007;18:475504–1–6.

[110] Jesse S, Kalinin S V, Proksch R, Baddorf AP, Rodriguez BJ. The band excitation method in scanning probe microscopy for rapid mapping of energy dissipation on the nanoscale. Nanotechnology 2007;18:435503–1–8.

[111] Newnham RE. Properties of materials: anisotropy, symmetry, structure. Oxford: Oxford University Press Inc.; 2005.

[112] Ganpule CS, Nagarajan V, Hill BK, Roytburd AL, Williams ED, Ramesh R, et al. Imaging three-dimensional polarization in epitaxial polydomain ferroelectric thin films. J Appl Phys 2002;91:1477–81.

[113] Ganpule CS, Nagarajan V, Li H, Ogale AS, Steinhauer DE, Aggarwal S, et al. Role of 90° domains in lead zirconate titanate thin films. Appl Phys Lett 2000;77:292–4.

[114] Eliseev EA, Kalinin S V, Jesse S, Bravina SL, Morozovska AN. Electromechanical detection in scanning probe microscopy: Tip models and materials contrast. J Appl Phys 2007;102:014109–1–12.

[115] Snoeck E, Normand L, Thorel A, Roucau C. Electron microscopy study of ferroelastic and ferroelectric domain wall motions induced by the in situ

application of an electric field in $BaTiO_3$. Phase Transitions A Multinatl J 1994;46:77–88.

[116] Roelofs A, Pertsev NA, Waser R, Schlaphof F, Eng LM, Ganpule C, et al. Depolarizing-field-mediated 180° switching in ferroelectric thin films with 90° domains. Appl Phys Lett 2002;80:1424–6.

[117] Kamlah M, Tsakmakis C. Phenomenological modeling of the non-linear electro-mechanical coupling in ferroelectrics. Int J Solids Struct 1999;36:669–95.

[118] Shvartsman V V, Kholkin AL. Polar structures of PbMg1/3Nb2/3O3-PbTiO3 relaxors: Piezoresponse force microscopy approach. J Adv Dielectr 2012;02:1241003–1–11.

[119] McGilly LJ, Schilling A, Gregg JM. Domain bundle boundaries in single crystal $BaTiO_3$ lamellae: searching for naturally forming dipole flux-closure/quadrupole chains. Nano Lett 2010;10:4200–5.

[120] Balke N, Bdikin I, Kalinin S V, Kholkin AL. Electromechanical imaging and spectroscopy of ferroelectric and piezoelectric materials: state of the art and prospects for the future. J Am Ceram Soc 2009;92:1629–47.

[121] Liu QD, Huber JE. State dependent linear moduli in ferroelectrics. Int J Solids Struct 2007;44:5635–50.

[122] Morozovska AN, Svechnikov S V, Eliseev EA, Jesse S, Rodriguez BJ, Kalinin S V. Piezoresponse force spectroscopy of ferroelectric-semiconductor materials. J Appl Phys 2007;102:114108–1–14.

[123] Hidaka T, Maruyama T, Saitoh M, Mikoshiba N, Shimizu M, Shiosaki T, et al. Formation and observation of 50 nm polarized domains in $PbZr_{1-x}Ti_xO_3$ thin film using scanning probe microscope. Appl Phys Lett 1996;68:2358–9.

[124] Rivard M, Laliberté M, Bertrand-Grenier A, Harnagea C, Pfeffer CP, Vallières M, et al. The structural origin of second harmonic generation in fascia. Biomed Opt Express 2011;2:26–36.

[125] Jungk T, Hoffmann Á, Soergel E. Contrast mechanisms for the detection of ferroelectric domains with scanning force microscopy. New J Phys 2009;11:033029–1–14.

[126] You L, Chen Z, Zou X, Ding H, Chen W, Chen L, et al. Characterization and manipulation of mixed phase nanodomains in highly strained $BiFeO_3$ thin films. ACS Nano 2012;6:5388–94.

[127] Park M, Hong S, Kim J, Hong J, No K. Nanoscale ferroelectric switching behavior at charged domain boundaries studied by angle-resolved piezoresponse force microscopy. Appl Phys Lett 2011;99:142909–1–3.

[128] Park M, Hong S, Klug JA, Bedzyk MJ, Auciello O, No K, et al. Three-dimensional ferroelectric domain imaging of epitaxial $BiFeO_3$ thin films using angle-resolved piezoresponse force microscopy. Appl Phys Lett 2010;97:112907–1–3.

[129] Park M, No K, Hong S. Visualization and manipulation of meta-stable polarization variants in multiferroic materials. AIP Adv 2013;3:042114–1–6.

[130] Kim KE, Jang BK, Heo Y, Lee JH, Jeong M, Lee JY, et al. Electric control of straight stripe conductive mixed-phase nanostructures in La-doped $BiFeO_3$. NPG Asia Mater 2014;6:e81–1–9.

[131] Humphreys FJ. Grain and subgrain characterisation by electron backscatter diffraction. J Mater Sci 2001;36:3833–54.

[132] Braga PC, Ricci D. Atomic force microscopy: biomedical methods and applications. Totowa, New Jersey: Humana Press Inc; 2004.

[133] Follin ND, Taylor KD, Musalo CJ, Trawick ML. Three-axis correction of distortion due to positional drift in scanning probe microscopy. Rev Sci Instrum 2012;83:083711–1–7.

[134] Jungk T, Hoffmann A, Soergel E. Quantitative analysis of ferroelectric domain imaging with piezoresponse force microscopy. Appl Phys Lett 2006;89:163507–1–3.

[135] Lei S, Eliseev EA, Morozovska AN, Haislmaier RC, Lummen TTA, Cao W, et al. Origin of piezoelectric response under a biased scanning probe microscopy tip across a 180° ferroelectric domain wall. Phys Rev B 2012;86:134115–1–12.

[136] Liu Y, Zhang Y, Chow MJ, Chen QN, Li J. Biological ferroelectricity uncovered in aortic walls by piezoresponse force microscopy. Phys Rev Lett 2012;108:078103–1–5.

[137] Gruverman A, Wu D, Rodriguez BJ, Kalinin S V, Habelitz S. High-resolution imaging of proteins in human teeth by scanning probe microscopy. Biochem Biophys Res Commun 2007;352:142–6.

[138] Minary-Jolandan M, Yu MF. Nanoscale characterization of isolated individual type I collagen fibrils: polarization and piezoelectricity. Nanotechnology 2009;20:085706–1–6.

[139] Li T, Zeng K. Nanoscale piezoelectric and ferroelectric behaviors of seashell by piezoresponse force microscopy. J Appl Phys 2013;113:187202–1–10.

[140] Balke N, Jesse S, Morozovska AN, Eliseev E, Chung DW, Kim Y, et al. Nanoscale mapping of ion diffusion in a lithium-ion battery cathode. Nat Nanotechnol 2010;5:749–54.

[141] Balke N, Eliseev EA, Jesse S, Kalnaus S, Daniel C, Dudney NJ, et al. Three-dimensional vector electrochemical strain microscopy. J Appl Phys 2012;112:052020–1–7.

[142] Liu JM, Liu ZG. A Monte-Carlo approach of domain switching in ferroelectric Potts lattice under external electric field. Mater Lett 1998;36:17–23.

[143] Duiker HM, Beale PD. Grain-size effects in ferroelectric switching. Phys Rev B 1990;41:490–5.

[144] Wu FY. The Potts model. Rev Mod Phys 1982;54:235–68.

[145] Potter BG, Tikare V, Tuttle BA. Monte Carlo simulation of ferroelectric domain structure and applied field response in two dimensions. J Appl Phys 2000;87:4415–24.

[146] Xue F, Gao XS, Liu JM. Monte Carlo simulation on the size effect in ferroelectric nanostructures. J Appl Phys 2009;106:114103–1–6.

[147] Tikare V, Holm EA, Fan D, Chen LQ. Comparison of phase-field and Potts models for coarsening processes. Acta Mater 1999;47:363–71.

[148] Hlinka J, Márton P. Phenomenological model of a 90° domain wall in $BaTiO_3$-type ferroelectrics. Phys Rev B 2006;74:104104–1–12.

[149] Gao P, Britson J, Nelson CT, Jokisaari JR, Duan C, Trassin M, et al. Ferroelastic domain switching dynamics under electrical and mechanical excitations. Nat Commun 2014;5:3801–1–8.

[150] Nelson CT, Gao P, Jokisaari JR, Heikes C, Adamo C, Melville A, et al. Domain dynamics during ferroelectric switching. Science 2011;334:968–71.

[151] Park SE, Shrout TR. Ultrahigh strain and piezoelectric behavior in relaxor based ferroelectric single crystals. J Appl Phys 1997;82:1804–11.

[152] Shrout TR, Zhang SJ. Lead-free piezoelectric ceramics: Alternatives for PZT? J Electroceramics 2007;19:111–24.

[153] Ramesh R, Spaldin NA. Multiferroics : progress and prospects in thin films. Nat Mater 2007;6:21–9.

[154] Zavaliche F, Zhao T, Zheng H, Straub F, Cruz MP, Yang PL, et al. Electrically assisted magnetic recording in multiferroic nanostructures. Nano Lett 2007;7:1586–90.

[155] Zavaliche F, Yang SY, Zhao T, Chu YH, Cruz MP, Eom CB, et al. Multiferroic $BiFeO_3$ films: domain structure and polarization dynamics. Phase Transitions 2006;79:991–1017.

[156] Lee N, Kim SJ. Effects of loading rate and temperature on domain switching and evolutions of reference remnant state variables during polarization reversal in a PZT wafer. Ceram Int 2012;38:1115–26.

[157] Ji DW, Kim SJ. Temperature-dependent ferroelastic switching of ferroelectric ceramics and evolution of linear material properties. Acta Mater 2013;61:1–11.

[158] Webber KG, Aulbach E, Key T, Marsilius M, Granzow T, Rödel J. Temperature-dependent ferroelastic switching of soft lead zirconate titanate. Acta Mater 2009;57:4614–23.

[159] Wang Z, Hu H. Auxetic materials and their potential applications in textiles. Text Res J 2014;84:1600–11.

[160] Prawoto Y. Seeing auxetic materials from the mechanics point of view: A structural review on the negative Poisson's ratio. Comput Mater Sci 2012;58:140–53.

[161] Huang CW, Ren W, Nguyen VC, Chen Z, Wang J, Sritharan T, et al. Abnormal Poisson's ratio and linear compressibility in perovskite materials. Adv Mater 2012;24:4170–4.

[162] Nye JF. Physical properties of crystals. Oxford: Clarendon Press; 1985.